# Interactions of Peripheral Nerve Cells with Soft Micropillar Interfaces

### THÈSE Nº 6705 (2015)

PRÉSENTÉE LE 23 OCTOBRE 2015

À LA FACULTÉ DES SCIENCES ET TECHNIQUES DE L'INGÉNIEUR CHAIRE FONDATION BERTARELLI DE TECHNOLOGIE NEUROPROSTHÉTIQUE PROGRAMME DOCTORAL EN BIOTECHNOLOGIE ET GÉNIE BIOLOGIQUE

### ÉCOLE POLYTECHNIQUE FÉDÉRALE DE LAUSANNE

POUR L'OBTENTION DU GRADE DE DOCTEUR ÈS SCIENCES

#### PAR

### Cédric Xavier PAULOU

acceptée sur proposition du jury:

Prof. S. Roke, présidente du jury Prof. S. Lacour, directrice de thèse Prof. C. Villard, rapporteuse Prof. J. Fawcett, rapporteur Prof. Ph. Renaud, rapporteur



## ACKNOWLEDGEMENTS

First of all, I want to address my sincere gratitude to Prof. Stéphanie P. Lacour, who directed this thesis. She gave me the opportunity to work in the best conditions, kept me on track, and more importantly, gave me the confidence that I needed, along with precious guidance and advice on scientific (and sometimes baby caring) matters.

I warmly thank my thesis committee Profs. James Fawcett, Catherine Villards, Philippe Renaud and Sylvie Roke for taking the time and energy to critically review my work.

I am particularly grateful to Drs. Ivan Minev, Abla de Luca and Aaron Gerratt for their careful reading and invaluable comments during the preparation of my manuscript. The in vivo nerve regeneration part of this work was made possible by the skilful surgeries of Dr. Pietro di Summa. I thank him for that and for helpful comments on data interpretation. The LSBI is a fun place to work at, mostly thanks to its cheerful members. I thank all of them for the good atmosphere which makes it easier to spend countless hours in the lab.

I want to thank my friends for the good times spent outside of the lab. I have a special thought for my EPFL classmates Bastien, Gilles, Johannes and Julien who greatly contributed to make this period of my life quite awesome.

I would not be here without the unconditional love and support of my parents, who always encouraged me and made it possible to do whatever I wanted in life. I take this opportunity to thank them with all my heart for the past 30 years.

Last but not least, I want to express my deepest gratitude to my beloved wife Frédérique, who is my real buddy in life. She has been of infinite support and understanding, especially during the painful process of thesis ending, which we both endured. She also expended the room available for love in my heart, by giving birth to Alexandre. I thank him for helping me to relativise the gravity of a failed experiment, and making me a more complete man.

Lausanne, 30 July 2015

Cédric Paulou

Regenerative peripheral nerve interfaces are particularly invasive implant devices. They rely on the growth of axons from transected nerve stumps through electrode-bearing structures in order to establish highly efficient communication channels with the nervous system. The functioning and lifetime of these devices is challenged by the host response from the nervous tissue, which complicates their use in long-term applications. The elicited foreign body reaction is characterized by chronic inflammation and excessive deposition of collagen. The difference in mechanical properties between implant material and nervous tissue, which are among the softest in the body, is thought to be an important contributor to these adverse effects.

With the motivation of improving the bio-integration of implanted nerve interfaces, this thesis evaluate micropillar arrays as a texture to modulate the behaviour of peripheral nerve cells on polydimethylsiloxane (PDMS) silicone surfaces. Thanks to their flexibility, micropillars can reduce the effective stiffness perceived by cells, while providing topographic cues at the microscopic level. Importantly, these mechanical and topographic cues can be easily tailored by modification of their geometrical dimensions.

Micropillar arrays with varying dimensions were fabricated by soft lithography process. Their mechanical behaviour under bending was simulated by finite element method (FEM) analysis to approximate their spring constants. The softest micropillar configuration had an effective surface stiffness of 0.7 kPa, representing a reduction of 3 orders of magnitude compared to bulk PDMS.

The effect of micropillar diameter (from 1.2 to 4.2 µm), modulating the surface stiffness, and the effect of interpillar spacing (from 1.0 to 7.6 µm), modifying micropillars density, were investigated in vitro. Dissociated cell cultures from dorsal root ganglion (DRG), comprising neurons and glial cells, were probed for different parameters after 7 days of incubation. While neurons spread and established neurite networks on all configurations, fewer glial cells were found on the softest and lowest density of micropillars. Neurites explored this pseudo-3D environment and preferentially anchored to the top of pillar shafts, well above the bottom surface. The matrix of pillars provided physical cues for growing neurites, which strongly aligned with the densest arrays. The morphology of neuronal bodies was affected by the most flexible pillars, which induced smaller and rounder somas. Macrophages and adipose-derived stem cells showed significantly increased attachment to

#### Acknowledgements

micropillar topographies compared to flat surface.

The effect of micropillars was investigated on nerve regeneration in vivo. Nerve guidance conduits patterned with micropillars on their lumen surface were sutured to the transected sciatic nerve of rats. While the axonal regeneration was slightly affected by the micropillar texture, macrophages were massively recruited to the micropillar surface in comparison to the flat control. Their phenotype was also affected, with predominantly classically activated macrophage in contact with the micropillars.

Altogether, these results demonstrate the possibility to modulate the behaviour of a variety of cell types in vitro and in vivo, through the patterning of micropillars on the surface. This approach is amenable to implementation on silicone neural implants for mitigating tissue-material interactions.

#### Key words:

Micropillars, Elastomer, Polydimethylsiloxane (PDMS), Young's modulus, Topography, Dorsal root ganglion, Neurons, Peripheral nervous system (PNS), Cell biomechanics, Nerve regeneration, Implant, Foreign body reaction

Les interfaces régénératives du nerf périphérique sont des dispositifs particulièrement invasifs. Ils supportent la croissance des axones depuis un nerf sectionné à travers des structures comportant des électrodes, ceci afin d'établir une voie de communication sélective avec le système nerveux. Le fonctionnement et la durée de vie de ces dispositifs est mis à mal par la réponse des tissus nerveux, ce qui restreint leur utilisation pour des applications de longue durée. La réaction à corps étranger ainsi provoquée est caractérisée par une inflammation chronique et un dépôt de collagène excessif. La différence de propriété mécanique entre le matériau de l'implant et les tissus nerveux, qui sont parmi les plus mous du corps, est considéré comme un facteur important contribuant à ses effets délétères.

Avec la motivation d'améliorer la bio-intégration des interfaces nerveuses implantées, cette thèse évalue les champs micropiliers comme textures pour moduler le comportement des cellules de nerf sciatique sur des surfaces en silicone polydiméthylsiloxane (PDMS). Grâce à leur flexibilité, les micropiliers réduisent la rigidité perçue par les cellules, tout en fournissant des éléments topographiques à l'échelle microscopique. Ces éléments mécaniques et topographiques sont facilement modulables en modifiant leurs dimensions géométriques.

Des matrices de micropiliers de diverses dimensions ont été fabriquées par un procédé de lithographie molle. Leur comportement mécanique en flexion a été simulé avec la méthode des éléments finis afin d'approximer leur constantes de raideur. La configuration de micropiliers la plus molle a une rigidité de surface de  $0.7\,\mathrm{kPa}$ , ce qui représente une réduction de 3 ordres de grandeur en comparaison du module d'élasticité du PDMS. L'effet du diamètre des micropiliers (de 1.2 à  $4.2\,\mathrm{\mu m}$ ), qui module la rigidité de surface, et l'effet de l'espacement inter-piliers (de 1.0 à  $7.6\,\mathrm{\mu m}$ ), qui modifie la densité de micropiliers, ont été investigués in vitro.

Des cellules dissociées de ganglions spinaux, comprenant des neurones et des cellules gliales, ont été examinées sous différents paramètres après 7 jours d'incubation. Alors que les neurones se sont propagés et ont établis des réseaux de neurites sur toutes les configurations, les cellules gliales étaient moins nombreuses sur les micropiliers les plus mous et les moins denses. Les neurites ont exploré cet environnement pseudo-tridimensionnel et se sont établis

#### Acknowledgements

préférentiellement sur le haut des micropiliers, bien au-dessus de la surface du sol. Les micropiliers ont fourni des éléments physiques aux neurites, qui se sont alignés sur les matrices les plus denses. La morphologie des corps cellulaires des neurones a été affectée par les micropiliers les plus flexibles, qui ont induit des somas plus petits et plus ronds. Les macrophages et les cellules souches dérivées de tissus adipeux ont montré un attachement significativement plus important sur des surfaces comprenant des micropiliers que sur des surfaces planes.

L'effet des micropiliers a été étudié in vivo sur la régénération nerveuse. Des conduits présentant des micropiliers sur leur surface luminale ont été suturés sur des nerfs sciatiques sectionnés de rats. Alors que la régénération des axones a été peu affectée par la texture des micropiliers, les macrophages ont été massivement recrutés sur les surfaces de micropiliers, en comparaison des surfaces contrôles planes. Leur phénotype a aussi été affecté, avec une prédominance des macrophages classiquement activés en contact avec les micropiliers.

En résumé, ces résultats démontrent la possibilité de moduler le comportement d'une variété de types de cellule in vitro et in vivo, au moyen de micropiliers présents sur la surface. Cette approche pourrait être intégrée à un implant neuronal afin de contrôler les interactions entre le tissue et le matériau.

Mots clefs: Micropilliers, Elastomère, Polydiméthylsiloxane (PDMS), Module de Young, Topographie, Ganglion spinal, Neurone, Système nerveux périphérique, Biomécanique cellulaire, Régénération nerveuse, Implant, Réaction au corps étrangers

# Table of Contents

Ackno	wieagem	ents	1
Abstra	act (Eng	lish/Français)	iii
List of	f Figures		xi
List of	f Tables		XV
Chap	ter 1:	Introduction	1
1.1	Conte	ext and Problem statement	2
	1.1.1	Neural prostheses	2
	1.1.2	Peripheral nerve interfaces	3
	1.1.3	Tissue response to neural implants	5
1.2	Objec	tives and scope of the thesis	8
1.3	Overv	view	10
Chap	ter 2:	Micropillar-textured surfaces	13
2.1	Intro	luction	14
	2.1.1	Photolithography	15
	2.1.2	Soft Lithography	16
	2.1.3	Replica molding	17
	2.1.4	PDMS	18
2.2	Fabric	cation of micropillars	20
	2.2.1	Design considerations	20
	2.2.2	Silicon master	23
	2.2.3	PDMS micropillar substrates	25
	2.2.4	Characterization	27
	2.2.5	Results	28
	2.2.6	Discussion	30
2.3	PDM	S Surface functionalization	33
	2.3.1	Tailoring the proprieties of PDMS surfaces	33
	2.3.2	Functionalization of PDMS micropillar substrates	34
	2.3.3	Coating strategy	34

	2.3.4	Absorption of Poly-lysine and Laminin on PDMS	35
2.4	Mecha	nical behaviour of micropillars	40
	2.4.1	Analytical model	40
	2.4.2	Finite Element Method (FEM) analysis $\ \ldots \ \ldots \ \ldots \ \ldots$	42
	2.4.3	Effective stiffness of micropillar surfaces	44
2.5	Multil	evel micropillar arrays	46
	2.5.1	Rationale	46
	2.5.2	"4-levels" design	47
	2.5.3	"Stripes" design	47
	2.5.4	Fabrication process	48
	2.5.5	Results	50
Chapt	ter 3:	Evaluation of micropillar textures in vitro	53
3.1	Introd	uction	54
	3.1.1	Cell sensitivity to substrate stiffness	54
	3.1.2	Neuronal mechanosensitivity	56
	3.1.3	Cell sensitivity to substrate topography	57
	3.1.4	Guidance of neurons by topography	58
	3.1.5	Micropillars as soft, topographically rich environment	59
3.2	Mater	ials and Methods	61
	3.2.1	Preparation of substrates	61
	3.2.2	Harvesting and dissociation of dorsal root ganglia	61
	3.2.3	Seeding and culture of DRG cells	62
	3.2.4	Immunofluorescence staining and imaging	63
	3.2.5	Scanning electron microscopy	64
	3.2.6	Quantification of cell densities	64
	3.2.7	Proliferation and viability assays	64
	3.2.8	Quantification of neurite and glial cell orientation	65
	3.2.9	Quantification of soma morphology	66
	3.2.10	Traction forces analysis	66
	3.2.11	Immortalized bone macrophages culture and assays	66
	3.2.12	Adipose-derived stem cells culture and assays	67
	3.2.13	Statistical analysis	68
3.3	Result	s - Primary DRG cells	69
	3.3.1	Micropillar substrates for in vitro experiments	69
	3.3.2	Culture of DRG cells on Chip 1 and Chip 9	69
	3.3.3	Integration of DRG cells on micropillars in the XZ plane	75

	3.3.4	DRG cell density	76
	3.3.5	Viability and proliferation	76
	3.3.6	Neuronal somas morphology	79
	3.3.7	Neurite orientation	81
	3.3.8	Schwann cells orientation	81
	3.3.9	Soma traction force measurements	83
3.4	Result	ts - Macrophages	86
	3.4.1	Attachment	86
	3.4.2	Morphology	88
3.5	Result	ts - Adipose-derived stem cells	90
	3.5.1	Stem cell morphology and phenotype	90
	3.5.2	Attachement and spreading	91
3.6	Discus	ssion	94
	3.6.1	Mechanical effects of micropillars	94
	3.6.2	Topographic effects of micropillars	97
	3.6.3	Integration and orientation of neurite networks in micropillars $$	97
	3.6.4	Behaviour of macrophages and stem cells on micropillars	98
	3.6.5	Behaviour of adipose-derived stem cells on micropillars	99
3.7	Concl	usion	102
Chapt	ter 4:	Evaluation of Micropillar Texture in vivo	105
4.1	Introd	luction	106
	4.1.1	Peripheral nerve injury and regeneration	107
	4.1.2	Tissue response to implanted neural devices	110
	4.1.3	Current strategies for neural implants	114
4.2	Mater	ial and Methods	116
	4.2.1	Creation of micropillar-textured nerve conduits	116
	4.2.2	In vivo implantation	119
	4.2.3	Tissue fixation and sectioning	120
	4.2.4	Determination of muscle weight	121
	4.2.5	Immunohistochemical staining and imaging	121
	4.2.6	Quantification of tissue cross-sectional area	122
	4.2.7	Quantification of axonal regeneration	122
	4.2.8	Quantification of fluorescence intensity	123
	4.2.9	Statistical analysis	123
4.3	Result	ts	124
	4.3.1	Fabrication of nerve conduits	124

### Table of Contents

	4.3.2	Implantation of conduits on transected rat sciatic nerves	. 126
	4.3.3	Nerve regeneration through simple conduits	. 126
	4.3.4	Quantification of tissue area in conduits	. 128
	4.3.5	Leg muscles weight measurements	. 129
	4.3.6	Nerve regeneration through theta conduit	. 130
	4.3.7	Axonal regeneration	. 132
	4.3.8	Short term implantation	. 135
	4.3.9	Macrophages	. 135
4.4	Discus	ssion	. 142
	4.4.1	Considerations on the design of the tube and the implantation $$ . $$	. 142
	4.4.2	Effect of micropillars on sciatic nerve regeneration	. 144
	4.4.3	Effect of micropillars on the immune response	. 145
	4.4.4	Implications for the tissue-material interface	. 147
4.5	Concl	usion	. 149
Chap	ter 5:	Conclusions	151
5.1	Summ	nary of the results	. 152
5.2	Signif	icance	. 156
5.3	Outlo	ok and Perspectives	. 158
Bibliog	graphy		161
Glossa	ry		179
Curric	ulum Vi	tae	181

# LIST OF FIGURES

1.1	Relation between invasiveness and selectivity of neural interfaces $\dots \dots$	3
1.2	Peripheral nerve interfaces with different levels of invasiveness	4
1.3	Stiffness of fabricated materials versus stiffness of biological tissues	7
2.1	Soft Lithography techniques	17
2.2	Examples of microstructures fabricated by soft lithography $\dots \dots$ .	18
2.3	Design of the different chips	22
2.4	Initial design and dimension of chips	22
2.5	Process flow of PDMS micropillar fabrication	23
2.6	Negative mold and a micropillar substrate mounted on a petri dish	26
2.7	SEM pictures of micropillars etched in a silicon wafer	28
2.8	SEM pictures of micropillars molded in PDMS by REM $\ \ldots \ \ldots \ \ldots$	29
2.9	CSI pictures	30
2.10	Comparison between PDL and LN coatings on DRG cells $\ \ldots \ \ldots \ \ldots$	35
2.11	Global vs selective coating of micropillars	36
2.12	Examples of defects of pillar tops-printed molecules	36
2.13	Absorption of Poly-L-lysine on PDMS substrates	37
2.14	Laminin coating imaged by immunofluorescence	38
2.15	Absorption of Laminin on PDMS, Glass and PS	39
2.16	Analytical model of a pillar bend by cellular force	40
2.17	Characterization of pillar mechanics with FEM simulations	43
2.18	FEM simulations of micropillar deformation	44
2.19	Schematic of the "4-level" design	47
2.20	Schematic of "Stripe" design	48
2.21	Process flow for fabrication of multilevel pillars	50
2.22	SEM images of the "4 levels" Si master	52
2.23	SEM images of the "Stripes" design Si masters	52
3.1	Cells sense and respond to biophysical parameters of their microenvironment	55
3.2	Cell-type dependant reaction to substrate stiffness	56
3.3	Effect of surface topography on neuronal and glial cells	59
3.4	Recapitulation of Chips 1 and 9 characteristics	70

3.5	Immunostaining of DRG cell cultures
3.6	Fluorescence images of DRG cells on Chips 1 and 9 after 7 DIV
3.7	SEM images of DRG cells on Chip 1
3.8	SEM images of DRG cells on Chip 9
3.9	Confocal imaging of DRG cells in the XZ plane
3.10	Distribution of neurons and glial cells on Chip 1 and 9 after 7 DIV $\dots$ 77
3.11	Proliferation and viability of cells on Chip 1 and 9
3.12	Morphology of neuronal somas on surfaces with diameter variations from
	Chip 1
3.13	Directionality of neurites on surfaces with variations of interpillar spacings . $82$
3.14	Alignment of Schwann cells and neurites on Chip 9 topographies 83
3.15	Traction force measurements of DRG soma
3.16	Attachment of macrophages after 2 DIV
3.17	Morphology of macrophages on Chip 1 and 9
3.18	Characterization of adipose-derived stem cells
3.19	Attachment of adipose-derived stem cells on Chip 9 arrays
3.20	Morphology of adipose-derived stem cells on Chip 9
3.21	Correlation between the number of somas and cells on flat PDMS 95
4.1	Anatomical structure of a peripheral nerve
4.1 4.2	Anatomical structure of a peripheral nerve
4.2	Schematic of nerve injury and regeneration mechanisms
4.2 4.3	Schematic of nerve injury and regeneration mechanisms
4.2 4.3	Schematic of nerve injury and regeneration mechanisms
4.2 4.3 4.4	Schematic of nerve injury and regeneration mechanisms
4.2 4.3 4.4 4.5	Schematic of nerve injury and regeneration mechanisms
4.2 4.3 4.4 4.5 4.6	Schematic of nerve injury and regeneration mechanisms
4.2 4.3 4.4 4.5 4.6 4.7	Schematic of nerve injury and regeneration mechanisms
4.2 4.3 4.4 4.5 4.6 4.7 4.8 4.9	Schematic of nerve injury and regeneration mechanisms
4.2 4.3 4.4 4.5 4.6 4.7 4.8 4.9 4.10	Schematic of nerve injury and regeneration mechanisms
4.2 4.3 4.4 4.5 4.6 4.7 4.8 4.9 4.10 4.11	Schematic of nerve injury and regeneration mechanisms
4.2 4.3 4.4 4.5 4.6 4.7 4.8 4.9 4.10 4.11 4.12	Schematic of nerve injury and regeneration mechanisms
4.2 4.3 4.4 4.5 4.6 4.7 4.8 4.9 4.10 4.11 4.12 4.13	Schematic of nerve injury and regeneration mechanisms
4.2 4.3 4.4 4.5 4.6 4.7 4.8 4.9 4.10 4.11 4.12 4.13 4.14	Schematic of nerve injury and regeneration mechanisms
4.2 4.3 4.4 4.5 4.6 4.7 4.8 4.9 4.10 4.11 4.12 4.13 4.14 4.15	Schematic of nerve injury and regeneration mechanisms

4.18	Attachment of cells on PDMS surfaces 2 days post-implantation 136
4.19	Attachment of cells on micropillar versus flat surfaces
4.20	Longitudinal section of theta tube showing macrophage distribution $12$ weeks
	post-implantation
4.21	Macrophages near the interface between tissue and material

# LIST OF TABLES

2.1	Definitions of the geometrical parameters of pillar arrays
2.2	Parameters for etching micropillar structures in silicon wafers
2.3	Dimensions of micropillars configurations on Chip 1 and Chip 9 $31$
2.4	Spring constants obtained analytically and with FEM simulation 43
2.5	Effective Young's modulus $E_{eff}$ for Chips 1 and 9
2.6	Dimensions of the micropillars from multilevel designs
2.7	Mechanical characteristics of "4 levels" Chip
3.1	Antibodies and stains used for in vitro experiments
4.1	Dimensions of the micropillars patterned on nerve tubes
4.2	In vivo experimental groups
4.3	List of antibodies and stains used for in vivo experiments

## Introduction

The overall motivation of this thesis is to address the challenge of the bio-integration of regenerative peripheral nerve interfaces. More specifically, the reduction of the mechanical mismatch between biological tissues and implant material constitute the main hypothesis underlying this research. Key concepts in neural interfaces, tissue response to implants and mechanobiology are presented in this chapter. Finally, the structure of the thesis is reviewed in the last section.

### Contents

1.1 Context and Problem statement	2
1.2 Objectives and scope of the thesis	8
1.3 Overview	10

## Context and Problem statement

### 1.1.1 Neural prostheses

Neuroprosthetics is a highly multidisciplinary field which seeks, through the use of neural prostheses, to restore, replace or provide human physiological functions which were impaired or absent. Taking many different forms, the common feature of neural protheses is the exchange information with the patient's nervous system, by means of recording or stimulation. Such communication channels can eventually provide motor or sensory capabilities when implemented into therapeutic systems.

Neural interfaces designate the devices establishing the communication between the nervous system and the prosthetic apparatus. To date, electric signals constitute the most straight-forward vector for exchanging information with the nervous system. For that purpose, neural interfaces generally rely on metallic electrodes to capture or inject electrical charges into electrically excitable tissues. The anatomical location of neural interfaces is a critical parameter, which has major implications on their functionality. For instance, non-invasive interfaces using surface electrodes can capture electro-encephalogram (EEG) or electromyogram (EMG) signals to assess the brain or muscle activity. However, their utility is restricted to areas near the surface of the body and recording/stimulation is only possible for large populations of neurons/muscles. On the other hand, neural interfaces which are implanted in the patient's body can address precise anatomical areas, allowing highly specialized actions. Examples of implanted neural interfaces used in clinical applications include deep brain stimulation for the treatment of Parkinson's disease [1], cochlear implants to restore audition [2] and epidural stimulation for treating pain [3]. The ability to target definite number of nerve cells, while avoiding perturbation or cross-talk with neighboring cells, augments the resolution of the communication channel. However, this comes at the expense of invasiveness, as the selectivity is largely dependant on the distance with the interface (Fig.1.1). Thus there is a trade-off between the selectivity needed for a particular application and the adverse effects due to invasiveness which can be afforded.

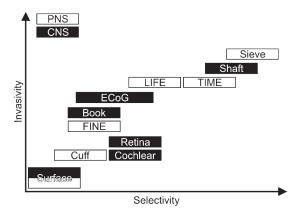


Figure 1.1 – Relation between invasiveness and selectivity of neural interfaces. Schematic plot showing the trade-off between the selectivity and the invasiveness for different neural interfaces present in the central (black rectangles) and peripheral (white rectangles) nervous system. Regenerative electrodes such as the Sieve electrode are among the most invasive devices, notably due to their applicability to severed nerve only. Adapted from Hassler et al. [4].

The most invasive implants fully penetrate the tissues to reach close contact with nerve cells, and are able to distinguish signals down to single action potentials [5].

#### 1.1.2 Peripheral nerve interfaces

Integrating a neural implant in the central or peripheral nervous system (CNS and PNS, respectively) constitute two very distinct situations. Most obviously, the tissue architectures are vastly different. Other contrasting parameters to take into consideration for a neural implant include the regeneration potential of the neurons, the tissue reaction to the implants or the mechanical behaviour of the tissues. The motivation of this thesis is focused on the situation pertaining to peripheral nerve interfaces. Thus, the discussion here concentrate on the PNS environment.

Interfacing the PNS is of particular interest for restoring motor and sensory functions when the integrity of peripheral nerves is compromised. It is also useful in case of spinal cord injury, where a lost connection between PNS and higher brain centers can be by-passed with an external system [6]. Peripheral nerve interfaces have the potential to alleviate a major health burden, as millions of amputees and paralyzed patients could benefit from a prosthetic devices connected to their nervous system. The ideal neuroprosthetic interface will implement a bi-directional communication, allowing seamless control of the prothesis by the patient's own nervous system, along with the feedback of sensory information arising from physical inputs on the prosthesis. However, important technical and biological challenges remain to be addressed in order to achieve a reliable system.

Various designs of peripheral nerve interface have been developed. They can be classified into three main categories, according to their invasiveness: Extraneural, intraneural and regenerative interfaces. Figure 1.2 provides one example of interface for each category. Cuff electrodes are extraneural devices which form a tube-like structure warping nerves in their luminal space. They are made of insulating materials such as polydimethylsiloxane (PDMS) or polyimide, and carry a certain number of electrode sites on their inner surface, facing the nerve. This minimally invasive approach has the advantage to avoid disruption of the epineurium, thus limiting the damages to the nerves, while restrict the stimulation to the encircled nerve portion [7]. Despite their use in clinical applications, cuff electrodes have significant limitations for complex neuroprosthetic applications. Most importantly, due to their external position, electrode selectivity is rather poor, and axons from outer periphery of the nerve are indiscriminately interfaced, while those at the center of the nerve remain inaccessible. Damage to the nerves can also occur during motion of the implant [8].

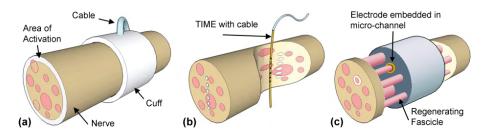


Figure 1.2 – Peripheral nerve interfaces with different levels of invasiveness. White areas depict the predicted area of activation upon electrical stimulation in each case. (a) Cuff electrodes reach only superficial fascicles. (b) Transversal intrafascicular multichannel electrodes (TIME) can excite several small populations of neurons in different fascicles across the nerve section. (c) Regenerative micro-channel electrode are traversed by small regenerating nerve fibers. Channels integrating electrodes can selectively interface the confined nerve fibers thanks to insulation from neighboring fibers (Adapted from Boretius et al. 2010 [9]).

The next level of invasiveness is reached with intraneural electrodes. Various designs exist, with different shapes and mechanisms of penetration. These include penetrating micro-electrode arrays (MEA) made out of silicon or titanium such as the Utah array, longitudinal intrafascicular electrode (LIFE) or transversal intrafascicular multichannel electrode (TIME). The latter design, which is shown on Fig.1.2(b), uses more flexible substrates like polyimide or parylene and platinum metal tracks [9]. The intraneural configuration of these devices greatly increases the signal-to-noise ratio and enables selective stimulation/recording of individual fascicles without cross-talk with neighboring fibers [4]. However, their invasive nature poses a problem on the long-term both for the stability of signal transduction and integrity of nerves [6, 10, 9].

Regenerative electrodes represent a distinct class of interface which take advantage of the potential of peripheral nerves to regenerate over short distances upon injury. The device is

placed on the proximal stump of a severed nerve, which forces the regrowing axons to invade the structures of the implant where electrodes are distributed. Sieve electrodes, one of the first regenerative interface, was formed of a planar surface comprising an array of via-holes with electrode sites, through which axons eventually pass by when regenerating [11]. Recent designs include tubular 3D scaffolds consisting of multiple longitudinal microchannels where individual fibers can grow [12, 13, 14]. Polyimide, SU-8 or silicone (PDMS) are used as bulk material, and microchannels incorporate electrode sites on their inner surface for interfacing the neurons (Fig.1.2(c)). The microchannel architecture simultaneously provides excellent selectivity, high number of interfaced fibers and good signal-to-noise ratio thanks to the insulation provided by channels. A strategy using bifurcating channels was proposed to promote the separation of ingrowing nerve fibers, in an attempt to further increase selectivity [15].

Successful interfacing with regenerative electrode designs is highly dependant on the capacity of axons to regenerate thought the microchannels. This issue can be modulated by several factors, such as the design and the material used for the implant. A critical geometrical parameter is the cross-sectional area of the microchannels. The number of ingrowing myelinated axons has been shown to decrease for channels with cross-section area smaller than  $100x100\,\mu\text{m}$  [13, 14]. Microchannels were filled with variable amount of tissue and axons across the device [13, 14]. This variability constitutes a risk for the channels incorporating electrodes to have lower or no axons, hindering their usability. One of the most advanced device incorporated 20 electrodes in almost 200 microchannels [16]. Thus, ensuring robust regeneration in electrode-bearing channels is critical for the functionality of the interface and should be addressed.

### 1.1.3 Tissue response to neural implants

While a few neural implants are currently approved for for therapeutic use, the majority of neural implants in development are hindered by adverse reaction of the tissue, which impedes their use in clinical applications. The need for highly selective interfaces drives the design of implants towards increased invasiveness, which amplifies the inflammation response of the host, both during the implantation and chronically.

Implanted electrodes generally elicit a Foreign Body Reaction (FBR), which is the mechanism of defense of our organism against macroscopic objects that cannot be phagocytozed. In the initial phase of the inflammation, proteins cover the surface of the implants, followed by cells such as macrophages and fibroblasts. If the inflammation reaction is sustained over long period of time, the layer of cells at the surface of the implant becomes thicker,

macrophages fuse into foreign body giant cells, collagen starts to be deposited and cytokines are released, amplifying the activation of cells.

Most often, the outcome of this process is the encapsulation of the foreign material in a fibrotic capsule formed by several layers of cells and collagenous fibers. The coupling between neuron and electrode, important for the transduction of electrical signals, is impaired by this change in the composition of the surrounding tissue. This can ultimately lead to device failure [6]. Thus, the FBR and its resulting fibrotic capsule can dramatically reduce the performance of chronically implanted neural electrodes, both in terms of functionality and lifetime.

The mechanisms leading to chronic inflammation around the implants are not yet fully understood. The role of the shape and size of the implant has been examined [17]. Reducing the footprint of electrodes has notably shown to ameliorate the initial reaction to the implantation procedure [18, 19]. In this sense, current microfabrication technologies allow for increasing miniaturization of neural interfaces. However, reduced dimensions alone is not sufficient to suppress the chronic inflammation response. Silicon microelectrodes with different shapes and sizes have been shown to induce similar inflammation reactions after 4 weeks of implantation [20].

The role of the mechanical compliance of the implant on the tissue response is gaining increased attention. Neural tissue are among the softest found in the body, with young modulus lower than 1 kPa. On the other hand, most penetrating electrodes are fabricated with stiff materials like silicon, glass or metals, which are in the Giga-Pascal range (Fig. 1.3). This represents a mechanical mismatch of several orders of magnitude between the neural tissues and the electrode materials. This interface between soft tissue and stiff implants is potentially a source of deleterious effects. The natural movement of nerves during locomotion may create stress at the electrode surface and induces relative displacement, causing sustained tissue inflammation or electrode deterioration, and eventually promoting the FBR.

The latest developments in neural implants are taking these parameters into consideration. Polymers with reduced stiffness compared to metallic materials are increasingly considered for neural interfaces [4]. Silicone elastomers such as PDMS demonstrate several advantages, due to their mechanical stretchability and good acceptance as foreign material in the body. However, with its elastic modulus in the MPa range, PDMS is still 2-3 order of magnitude stiffer than neural tissue.

On the microscopic level, the sensitivity of cells to the mechanical components of their

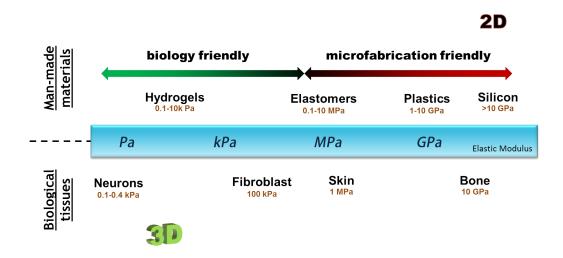


Figure 1.3 – Stiffness of fabricated materials versus stiffness of biological tissues. The elastic modulus of materials used for microfabrication is 3-6 orders of magnitude stiffer than neural tissue. A structural mismatch is also present between the three-dimensional architecture of biological tissues and the mostly planar microfabrication techniques.

environment is a well-demonstrated nowadays. Evidence has shown that cells can induce specific cellular programs in response to the mechanical properties of their surroundings [21]. For instance, neurons were shown to thrive more on soft substrates with stiffness of few hundreds of Pascals in vitro [22, 23]. This value is close to the one encountered by neurons in their natural environment in vivo [24]. Topography plays a important role as well, especially for exploratory cells such as neurons. The addition of three-dimensionality to a substrate may provide better mimicking of the in vivo situation as well.

Taken together, these considerations indicate the need for strategies to create bio-mimetic implants and electrodes surfaces, which would seamlessly integrate with neural tissue and minimize inflammation. The reduction of the mechanical mismatch between tissues and implanted materials may be a crucial point towards this goal. *In fine*, the acceptance and reliability of future implanted neural devices, which should sustain decades of use in the body, will greatly benefit from these efforts.

## Objectives and scope of the thesis

Problems associated with the integration of neural implants into the body currently lack a reliable, practical solution, which hinders the development of clinical applications for neuroprosthetic devices. The overall motivation of this thesis is to ameliorate the biointegration of such implanted nerve interfaces. Two aims in particular are targeted: the association between neurons and electrodes should be promoted, and the formation of excessive collagen due to foreign body reaction should be reduced. The main hypothesis driving the strategy developed here is that the behavior of cells can be altered by modulating the local mechanical microenvironment which is presented at the surface of an implant. More specifically, the influence of mechanical and topographical cues on the biological response to silicone surfaces is investigated.

The specific case of a regenerative peripheral nerve interface made out of PDMS and structured with microchannels serves as a motivation to study this question. This kind of device guides axonal processes through its structures, thereby creating a close contact between neurites and electrodes. As one of the most invasive designs, this microchannel regenerative interface has shown foreign body reactions with significant fibrotic tissue deposition on the surfaces of the implant, perturbing the axon-electrode association. This issue is critical for extracellular recording electrodes because signal transduction, which depends on the axon-electrode interface, is hindered by the invading fibrotic tissue. The motivation of the present research is thus to promote the growth of nervous tissue towards implant's structures while avoiding fibrotic encapsulation.

To achieve this, the strategy developed here relies on an micro-structured surface presenting topographic and mechanical cues at the cellular level, and serving as mechanical stealth interface for cells on the implant surface. The approach proposed to modulate the stiffness and topography sensed by the cells is to create fields of micron-size pillars on the surface. Micro-pillars act as springs that bend according to the geometric and elastic properties of the material when subjected to a force. Therefore, the effective compliance of the surface presented to the cells is artificially reduced and can be controlled through geometric

variables. These micropillar arrays, whose creation requires microfabrication and soft lithography technologies, constitute a versatile tool for studying cell-matrix interactions and mechanobiology. For instance, modulation of substrate rigidity with micropillars was shown to influence human mesenchymal stem cells differentiation [25].

In the initial part of the project, extensive characterization of peripheral nerve cells response to micropillar substrates with varying configurations is performed in vitro. Other types of cells relevant to the context of FBR and regenerative strategies are be probed, including macrophage and stem cells. The information gained in the in vitro phase then served to determine the favorable characteristics of the micropillar configuration to be implanted in vivo. The micropillar texture is then implemented on the inner surfaces of nerve conduit implants and its effect on nerve regeneration evaluated on a transected rat sciatic nerve model.

## Overview

After this introductory chapter, the structure of the thesis is divided into 3 main chapters presenting the background, methods, results and discussions on the different steps of the experimental work. The last chapter concludes the thesis with a general discussion and outlook on the results.

Chapter 2 describes in details the fabrication of the micropillar structures in PDMS, and the aspects linked with the preparation and characterization of the interfaces for in vitro and in vivo experiments. First, a library of micropillar configurations was designed to fit on a single silicon wafer, allowing rapid replication by replica molding. Geometrical parameters such as micropillar diameter, inter-pillar spacing and lattice arrangement were varied. Small test surfaces with different configurations were grouped into chips designed for the in vitro assessment of cellular behaviour. The absorption of molecules to promote cell adhesion on the PDMS surfaces was inspected and a protocol to prepare the micropillar interface for cell culture was established. Characterization of the mechanical behaviour of the micropillars was investigated with analytic model and finite element methods. Finally, surfaces with patterns of micropillar with different heights are described.

All experiments related to the in vitro assays are discussed in the **Chapter 3**. Cultures of dissociated cells derived from dorsal root ganglions (DRG) were established on 2 kinds of micropillar chips: The first chip presents 4 different diameters of pillars, which can be translated into 4 distinct effective surface stiffness. The second chip offers 3 different interpillar spacings, modifying the topography and surface area available for cell attachment. The influence of these parameters on DRG neurons were quantified in terms of cell density, soma morphology and neurite orientation. Co-cultured glial cells were inspected as well. Acting as force sensors, micropillars were used to measure the traction forces applied by DRG neurons on their substrate. This chapter is concluded with pilot experiments on other cell types, including an immortalized macrophage cell line and undifferentiated mesenchymal stem cells from adipose tissues.

Chapter 4 details the fabrication of nerve guidance conduits with micropillar textures and

the in vivo experimentation performed during this thesis. The regeneration of transected rat sciatic nerve through textured conduits served as model. Two type of conduits were created: First a simple tube with inner surface covered with micropillar, and secondly a tube comporting a central membrane which divides the lumen into 2 longitudinal chambers. One half is covered with micropillars and the other is left with flat surfaces. This design allowed the simultaneous inspection of nerve regeneration in the test and control conditions. Regeneration is assessed in terms of total tissue area, axonal area and macrophage presence and phenotype in the tissues.

To conclude, **Chapter 5** puts in perspective the results obtained with micropillars, comparing the in vitro and in vivo contexts. The implications of the results for strategies aiming at reducing foreign body reaction with micro-textured surfaces are discussed, as well as their applicability to neural interfaces. Elements of future investigations are finally given as final thoughts.

# MICROPILLAR-TEXTURED SURFACES

This chapter focuses on the technical aspects of the creation of PDMS micropillar arrays. The fabrication process of chips for in vitro assays with multiples configuration of micropillars is described, along with their mechanical characterization with an analytical model and with FEM simulations.

### Contents

2.1 Introduction	14
2.2 Fabrication of micropillars	20
2.3 PDMS Surface functionalization	33
2.4 Mechanical behaviour of micropillars	40
2.5 Multilevel micropillar arrays	46

## Introduction

The first phase of this thesis concentrated on the development of a library of microtopographies in the form of micron-size pillars, having their base fixed to the bottom surface and their other extremity freely moving. This kind of topography, referred to as micropillars or microposts, combines characteristics such as increased total surface area, ordered arrangement and flexible geometry. Micropillars have found utility in diverse applications such as super hydrophobic surfaces, reversible bonding to surfaces, and reduction of electrode impedance [26, 27, 28]. For the past ten years, one of the major use of flexible micropillars was found in bio-engineering applications.

Flexible micropillar topographies have been patterned mainly on silicone surfaces, using the biocompatible polydimethylsiloxane (PDMS). One of the first reported use of such topography was the measurement of traction forces applied by cells on the micropillars [29]. Since then, a plethora of studies on biomechanical and topographical interactions of diverse cell types on micropillars were undertaken [30, 31, 25]. To the best of the author's knowledge, none of those investigated the interactions of cells from the peripheral nervous system on micropillars. One of the great advantage of micropillars in the context of physical interactions with cells is the possibility to geometrically modulate the topographic and mechanical cues, without affecting the surface chemistry, ligand concentration, or polymer chain length.

The emergence of PDMS micropillars as a bio-engineering tool has been promoted by the democratization of soft lithography technologies in academic institutes and labs, where they could be used by bioengineers. However, the fabrication of high-resolution arrays often requires to create a hard mold by conventional UV photolithography and etching technologies. In the following sections, these techniques are reviewed, to serve as an introduction to the protocol of fabrication of micropillars used for this work.

The essential characteristics of micropillar arrays are covered in this Chapter 2. A detailed procedure for the fabrication of a positive hard silicon mold, presenting arrays of pillars with different diameters and spacings is included. The design of the mold is optimized for the

rapid production of substrates for in vitro assays, allowing to probe multiple configurations on the same culture. The coating of the array surfaces with adhesion-permissive molecules and extracellular matrix proteins is a crucial parameter for the attachment and growth of cells. The optimization of the coating protocol for in vitro experiments is discussed in this chapter. Micropillars constitute mechanical cues for the cells, which bend them by applying forces in the plane of the array. The behaviour of micropillars under bending was characterized in order to evaluate their flexibility. The effective modulus presented by micropillared surfaces is compared to continuous elastic substrates, and an equivalent modulus is proposed for micropillar arrays. Finally, additional designs of micropillar arrays with multiples heights of pillar patterned on the same arrays are demonstrated. These multiple heights can serve to study cellular traction forces in ideal conditions or provide additional topography or 3D cues for the cells.

### 2.1.1 Photolithography

Microfabrication methods encompass an ensemble of techniques which rely on diverse physical, chemical and mechanical treatments. Among those, photolithography constitute the primary technique for transferring patterns on a substrate. It has been used now for decades for the fabrication of integrated circuits (IC). One of the great merit of this technology is the ability to batch-process features in parallel, which enables mass-production. The general steps in photolithography include the spin-coating of a thin layer of photosensitive material (called photoresist) on top of the substrate such as a silicon wafer. The film is then exposed to a radiation source through a photomask, with transparent and opaque zones of the mask defining the exposed and unexposed areas, respectively. Chemical compounds absorbing at certain wavelengths are present in the photoresist. When the film is immersed in a developing solution, these chemical compounds render the exposed areas either soluble, in the case of positive-tone resist, or insoluble for negative-tone resist. As a result of developing, the dissolved parts leave a pattern of photoresist on top of the substrate. The patterned film then typically serves as a mask for subsequent processes, such as etching, thin film deposition or doping.

The resolution of features that can be obtained depends on several factors, such as the wavelength of light used for the exposure, the thickness of the photoresist film or the numerical aperture of the lens in projection systems. Modern improvements of the standard technique, such as multiple patterning or immersion lithography, now allow to pattern nods down to a few nanometers.

While photolithography is inevitable for the fabrication of most microelectronics devices,

it has a number of disadvantages for applications in other domains such as biology or chemistry. For instance, the financial cost of this technology is relatively important, especially if one considers the investment for the infrastructure and equipment. This may preclude its use by non-specialized researchers. Secondly, the fact that it is highly optimized for microelectronic-related materials reduces its compatibility with some materials and with conventional methods in cell and tissue culture.

### 2.1.2 Soft Lithography

Soft lithography was developed with the motivation to overcome the limitations of conventional photolithography. It allows the rapid prototyping of diverse structures on the micro- to nano-scale at a modest cost [32]. As indicated by its name, soft lithography is amenable to use with materials with a considerably lower elastic modulus than those used in traditional photolithography. Central to this approach is the use of an elastomer, generally PDMS, to serve as a mold, a stamp or a mask. The usual steps of a soft lithography process flow include: 1) the design of the pattern, most often with computer aided design (CAD) softwares. 2) the fabrication of a rigid master with a positive imprint of the structures, generally by photolithography. 3) the fabrication of the PDMS stamp or mold. 4) the replication, embossing or printing of the final microstructure/micropattern. This process still implies the use of conventional microlithographic methods. However, once the master is obtained, the remaining steps can usually be performed in the lab environment, outside of the cleanroom facility. The solidity of the master mold allows for highly repeated use, preventing further need of photolithography. One of the great advantages of soft lithography is the compatibility of its processes with a plethora of materials, most interestingly with bio-compatible organic polymers [33]. Since the first developments during the nineties, soft lithography has rapidly expanded its toolbox and now represent a whole family of techniques [34]. These can be broadly associated with two main groups: Microcontact printing and Micromolding techniques.

In microcontact printing, a stamp with a relief pattern is inked and brought in contact with a target substrate. This technique allows to form patterns of molecules on the micron scale. It is now commonly used to print self-assembled Monolayers (SAMs) and bioactive compounds, thereby providing functionality and spatial control over the surface. By extension, microcontact printing can be used to pattern living matter: printing motifs of pro- or anti-adhesion molecules will confine cells to the desired area. This has notably enabled to study the effect of cytoplasm shape on cellular programs like apoptosis and proliferation [35].

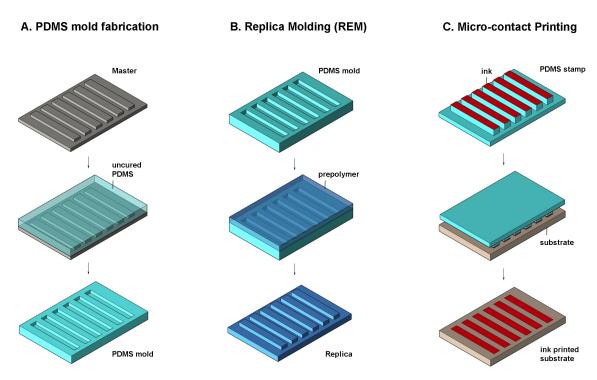


Figure 2.1 – Soft Lithography techniques. Schematic representation of the principles of microfabrication with soft lithography. A) Fabrication of the elastomeric mold or stamp by replication from a rigid master. B) Replica molding of microstructures from a elastomeric mold. C) Elastomeric stamps used to pattern molecules by micro-contact printing.

The general concept of **Micromolding** is to replicate of the structural information of a master, both on the microscopic scale, with surface micropatterns, and on the macroscopic scale, with the general shape of the master. Micromolding has been widely used for replicating microstructures from the surface of hard molds fabricated by conventional photolithography. The mass-production of compact disks with sub-micron features illustrates well the efficiency of this approach, both in terms of cost and pattern resolution. By introducing an elastomer instead of hard material for the mold, the process gained flexibility, and a new set of methods were developed, for example: Micro-transfer molding [36], Replica molding (REM) [37], micromolding in capillaries [38] or solvent-assisted micromolding [39]. A diversity of microstructures can be fabricated with these methods, as illustrated on Fig.2.2.

### 2.1.3 Replica molding

REM is of prime interest in this thesis, as it is the method used to produce micropillar patterns. Starting from a rigid master with 'positive' structures, elastomeric molds with a negative imprint are created. A liquid precursor of the final material is then drop casted on the negative molds. Once solidified, the casted material is peeled off the mold to release the final structures. This method allows the straight-forward replication of three-dimensional

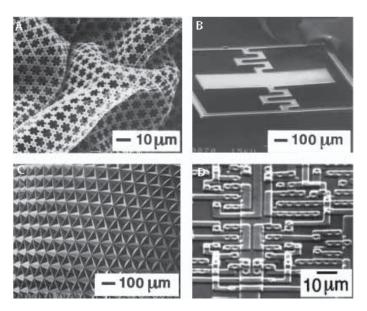


Figure 2.2 – Examples of microstructures fabricated by soft lithography. SEM images of polymeric microstructures fabricated using: A) Micromolding in capillaries , B) Micro-transfer molding, C) Replica molding (REM), D) Solvent-assisted micromolding.

shapes, in multiple copies and over large areas. It is particularly well suited for high aspect ratio structures, such as micropillars. Moreover, the resolution that can be obtained with this method is not limited by light diffraction like with photolithography. Features down to  $10 \,\mathrm{nm}$  in lateral resolution and  $5 \,\mathrm{nm}$  in vertical resolution have been reported over a  $1 \,\mathrm{mm}^2$  area [37].

The use of an elastomeric material for the mold offers significant advantages. Firstly, its elasticity permits the release of complex, fragile structures, which might not be possible if both materials were hard. This also participates in the high fidelity of the replicated features over numerous rounds of replications with the same mold. Another interesting feature of elastomeric mold is their deformability. By applying mechanical deformation, one can modify the shape and dimensions of the resulting molded structures. For instance, the bending of a mold structured with nanometric lines resulted in a reduction of their thickness from 50 to 30 nm on the polyurethane replica [37]. On the macroscopic scale, the ability to deform the mold allows to readily pattern non-planar surfaces. This will be demonstrated in this thesis with the patterning of high aspect ratio micropillars on the inner surface of a tube with a 1.6 mm inner diameter.

#### 2.1.4 PDMS

Among the vast choice of elastomers available, the silicone rubber PDMS is the most frequently used in soft lithography techniques. Its chemical structure, properties and availability make it particularly attractive, not only for microfabrication, but also for several biomedical applications [40, 41, 42]. PDMS is characterized by the presence of organic methyl groups attached on the silicon atoms of its inorganic silioxane backbone. Its low glass transition temperature (ca. 150 K) makes it liquid at room temperature, and it is easily cross-linkable to form a solid. The Sylgard 184 from Dow Corning, which was used in this thesis, comes as a two parts system: A prepolymer base and a catalytic curing agent containing a platinum complex. Upon mixing and heating, an hydrosilylation reaction occurs between the vinyl and hydrosilane groups in the mixture, which triggers the solidification of the elastomer. The ratio of base to curing agent determines the elastic modulus of PDMS, along with curing time and temperature. Thus, it is possible to tune its elasticity over a fairly wide range, from 50 to 4000 kPa [43].

PDMS has a number of interesting features in various contexts: (i) its elasticity allows a conformal contact with surfaces that are non-planar both on the macro and micrometric scales. This is useful for releasing intricate 3D structures after solidification, but also to form water-tight sealing in microfluidics. (ii) PDMS has a low interfacial free energy and is chemically inert. This prevents reactions or bonding of the polymers which are casted during REM. Its stability enables to fabricate durable molds which can be utilized tens of times over a long period of time. (iii) PDMS is also optically transparent down to 300 nm, which is critical for certain applications. It allows the cross-linking of photosensitive polymers through the mold in soft lithography. Its use in optical applications includes the fabrication of optical components for adaptive optics [44]. It is also well adapted for biological research, which often requires optical microscopy inspection. (iv) The properties of PDMS surfaces can be readily modified. A brief treatment with an oxygen plasma will expose hydroxyl groups, thereby turning the surface from hydrophobic to hydrophilic. This enables the absorption of molecules, the formation of SAMs, and the bonding to other substrates. (v) Finally, PDMS is easily available for purchase in large quantities at a relatively affordable price. This makes PDMS an attractive solution for manufacturing and mass-production.

# Fabrication of micropillars

In this section, the materials and methods for fabricating the different configurations of micropillar are described and discussed in details, from the initial design to the characterization of the substrates.

## 2.2.1 Design considerations

The very first steps of this project involved the design of the patterns to be fabricated on PDMS surfaces. Micropillars are physically defined first on photomasks, as arrays of dots. These photomasks are the central elements for structuring masters by photolithography, and will thus determine the critical dimensions (CD) of the pattern. The layout of photomasks is initially generated with a computer-aided design (CAD) tool. The geometrical parameters are critical and were tailored to use micropillar arrays as in-vitro and in-vivo experimental tools. These parameters include the dimensions of pillars, their spatial arrangement, the surface of the arrays and the arrangement of different arrays, etc.

The different configurations of pillars are primarily defined by the diameter of pillars D, the spacing of pillars S, and the height of pillar H. Table 2.1 recapitulates the definitions of these variables and their associated symbols, which are used throughout this text.

Table 2.1 – Definitions of the geometrical parameters of pillar arrays.

Dimension	Symbol	Definition
Diameter	D	Diameter of the pillars
Spacing	S	Distance from edge to edge of neighboring pillars
Spacing in x	Sx	Spacing in the direction of the X-axis
Spacing in y	Sy	Spacing in the direction of the Y-axis
Height	H	Length of the pillars from bottom to top surface

These parameters are assumed to have an impact on cell spreading and behaviour, since they alter the topography on which the cell has to adhere and evolve. It may also be necessary to optimize these dimensions for traction force measurements and proper mechanosensing by the cell. The spacing should be large enough to allow sufficient deflection of pillars

without contact between them, and it should be compact enough to mimic as much as possible a pseudo-continuous substrate for the cell. The density of pillars also defines the spatial resolution of traction force maps. On the other hand, the diameter D will modulate the stiffness of the pillar and the area available for cell focal adhesion (FA) complexes. Excessively large diameters render pillars too stiff for traction force detection, whereas diameters too small complicate the measure of pillar displacement. Ideally, pillar top surfaces should host a single FA site for efficient cell mechanosensing and force estimation. If D is too small, it might prevent the formation of FA sites. Alternatively if D is too large, the presence of multiple FAs on the same pillar might interfere with the effect of reduced substrate stiffness introduced by the pillar geometry. All these parameters have to be balanced in order to suit the desired effect or application.

Cellular traction forces and mechanosensitivity can vary greatly depending on the cell type. Therefore both D and S have to be optimized to fit best the cell type which is targeted by the study. One of the goals of this thesis is to assess which would be the optimal configuration for the regeneration of nerves and the prevention of fibrosis. In order to efficiently probe the effect of different parameters, a range of configurations were patterned on a single silicon master. The diameter, spacing and arrangement of pillars were successively varied on the wafer. However, to test the effect of pillar height, new silicon masters had to be fabricated for each target height.

The first part of the project investigates cellular behavior in vitro. Thus, the master is primarily designed to fit cell culture equipments. Samples were defined on the master as chips of approximately  $1\,\mathrm{cm}^2$ , fitting inside of round  $35\,\mathrm{mm}$  diameter petri dishes. On the surface of each sample, 4 small areas with variations of the same parameter are present, with flat surfaces surrounding the pillar arrays (Fig.2.3 A-B). The advantage of such layout is that the effect of the parameter can be observed simultaneously on the same sample, in the exact same conditions.

The layout of the silicon master features nine different chips and is represented on Fig.2.3 C. Two designs of chips with different arrangements of arrays were created. The design A, which is featured on Chips 1 to 6, has 4 square areas of  $4\,\mathrm{mm}^2$  with pillars, separated by 1 mm wide flat PDMS spaces (Fig.2.3 A). The zones noted S1, S2, S4 and S8 are designating 4 types of arrays with variations of pillar spacing of 1, 2, 4 and 8 µm respectively. The diameter is kept constant on individual chips, but is varied from chip to chip: Chips 1 and 4 have  $D=1\,\mathrm{\mu m}$ , Chips 2 and 5 have  $D=2\,\mathrm{\mu m}$ , and Chips 3 and 6 have  $D=4\,\mathrm{\mu m}$ . Chips 1 to 3 feature arrays with a square lattice, whereas Chips 4 to 6 feature an hexagonal lattice.

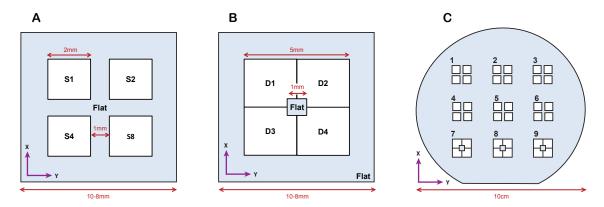


Figure 2.3 – Design of the chips for in vitro assays. White zones represent micropillar arrays and blue zone represent flat areas. A) Sketch of the design from Chips 1 to 6: Configurations S1, S2, S4 and S8 have arrays with interpillar spacing of 1, 2, 4 and 8  $\mu$ m. (B) Sketch of the design from Chips 7 to 9: Configurations D1, D2, D3 and D4 have arrays with post diameters of 1, 2, 3 and 4  $\mu$ m. (C) Layout of the nine chips on a Si wafer.

For the design B, on Chips 7 to 9, there is no flat space in between the arrays of pillars, and the arrays areas are slightly bigger, with 6 mm<sup>2</sup> (Fig.2.3 B). The absence of flat zone in these chips allows to observe cell simultaneously experiencing different configurations, as they cross the limit of the arrays. The different arrays feature variations of diameter instead of spacing. Arrays D1, D2, D3 and D4 have pillars with diameters of 1, 2, 3 and 4  $\mu$ m, respectively. The spacing is varied from chip to chip: Chip 7 has  $S = 1 \mu$ m, Chip 8 has  $S = 2 \mu$ m and Chip 9  $S = 4 \mu$ m. Pillars are arranged in a square lattice on these chips.

With this design, 27 configurations of pillar arrays can potentially be produced on a single wafer out of the 9 chips. The dimensions of arrays from each chips are recapitulated on Table 2.4.

Ch	Chip 1		Chip 2		ip 3	_				
D:	= 1	D	= 2	D = 3						
S=1	S=2	S=1	S=2	S=1	S=2	square				
S=4	S=8	S=4	S=8	S=4	S=8	lattice				
Ch	ip 4	Ch	Chip 5		ip 6	_				
D:	= 1	D	D = 2		D = 3					
S=1	S=2	S=1	S=2	S=1	S=2	hexagonal				
S=4	S=8	S=4	S=8	S=4	S=8	lattice				
Ch	Chip 7		Chip 8		ip 9	_				
S =	S = 1		S = 2		S = 2		S = 2		= 4	
D=1	D=2	D=1	D=2	D=1	D=2	square				
D=3	D=4	D=3	D=4	D=3	D=4	lattice				

Figure 2.4 – Initial design and dimension of chips. All numbers are in micron units. D=diameter, S=spacing. Sx and Sy are considered equal to S in the initial design.

#### 2.2.2 Silicon master

Creation of the silicon master is the longest and most critical part of the entire fabrication process. It requires several steps that need to be individually optimized. An overview of the entire process flow can be found on Fig.2.5.

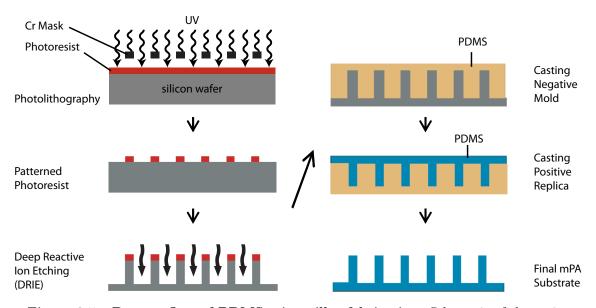


Figure 2.5 – Process flow of PDMS micropillar fabrication. Schematic of the major steps of the fabrication process. The left column depicts the fabrication of the silicon master by photolithography. The right column shows the double molding step for replication of the microstructures by REM and production of the final micropillar surfaces.

Photomask The first element to obtain is the photomask for photolithography. Chromium blank plates (Nanofilm, USA) were patterned at the CMi by direct laser writing with an optical pattern generator (Heidelberg DWL200). The light source used for exposure was a krypton gas laser (413 nm). The minimal spot size of exposure with this system is  $0.8 \,\mu\text{m}$ , according to the equipment documentation. Thus, the maximal resolution of features will be limited around this dimension. The layout of the masks, which design was described earlier, consisted of dark circles on clear background. After the exposure, masks are developed with an automatic developer system (Süss DV10), and the chromium film was etched for 90 s in a commercial solution of perchloric acid (HClO<sub>4</sub>) and ceric ammonium nitrate (NH<sub>4</sub>)<sub>2</sub>[Ce(NO<sub>3</sub>)<sub>6</sub>]. Finally, the mask were stripped from the remaining photoresist by immersion in a dedicated bath (Technistrip P1316) and cleaned in deionized water.

**Photolithography** A high-resolution positive photoresist (AZ ECI 3000, Merck Performance Materials) was used as mask for the etching of silicon wafers. The adhesion of the photoresist on silicon is generally poor, which can result in loss of fine features during the

development. This is especially a challenge in our case with small dots down to  $1 \,\mu m$ . A stringent pre-treatment was applied to wafers in order to increase photoresist adhesion:

- 1. Immersion in Piranha solution at 100 °C for 10 min
- 2. Exposure to Oxygen plasma (500 W) for 10 min
- 3. Dehydration on a contact hotplate at 200 °C for 15 min
- 4. Priming with vapor phase deposition of Hexamethyldisilazane (HMDS)

Once treated, wafers were spin-coated with a 0.6 µm thick layer of AZ ECI. An automatic coater (Rite Track 88 series) executed theses steps: Wafers were spun at 5610 rpm for 30 s to create an homogenous film, followed by a softbake in proximity mode at 115 °C for 90 s. Coated wafers were exposed to UV light through the previously fabricated photomask. Exposures were performed on a mask aligner Süss MJB4, equipped with a Hg lamp and i-line filter (365 nm), delivering 15 mW cm<sup>-2</sup>. The optimal light dose varied from batch to batch between 55-75 mJ cm<sup>-2</sup>. Hard contact mode between the wafer and the mask has to be used to reach a resolution near the 1 µm range. Post-exposure baking was not found to improve the outcome of the patterns. Exposed wafers were immersed in the developer solution MF-CD-26 (Shipley) in a beaker with constant gentle manual agitation. The development was stopped by immersion in water when all features were resolved, generally after a few minutes.

Etching Highly anisotropic etching is needed to achieve pillars with proper vertical walls. This is especially critical with high aspect ratio structures such as micropillars. The most adequate solution in this case is to use Deep Reactive Ion Etching (DRIE). The Bosch process, which is a widely used DRIE technique, relies on the alternative use of fluorine chemistry (SF<sub>6</sub>) to isotropically etch silicon, and the deposition of a teflon-like passivation layer ( $C_4F_8$ ) to protect the structure from further etching. The directional ions that are bombarded on the substrate during the etch phase only remove the polymer from the bottom surface, leaving the side walls protected. By switching between these modes every few seconds, quasi-vertical profiles are obtained. However it does produce slight undulating sidewalls artifact on the vertical surfaces.

Wafers patterned with photoresist were etched with the DRIE equipment Alcatel 601E. The parameters of the optimal recipe are reported in Tab.2.2.

Etch depth was monitored with a mechanical profilometer (Tencor Alpha-step 500) and adjusted to reach the desired height of pillars by incremental etch steps. Once the desired height was reached, the remaining photoresist was stripped from the wafer by exposure to

	Etching	Passivation
Gas	SF <sub>6</sub>	$C_4F_8$
Flow rate	300  sccm	150  sccm
Process time	$3 \sec$	$1  \mathrm{sec}$
RF source power	$1500~\mathrm{W}$	$1500~\mathrm{W}$
RF Bias power	100 W	$100 \mathrm{W}$
Etch rate	$2.25\mu\mathrm{mmin^{-1}}$	

Table 2.2 - Parameters for etching micropillar structures in silicon wafers.

an oxygen plasma for a couple of minutes. Several etch depths were produced on different wafers. However, a wafer with  $10\,\mu m$  etch depth was the one typically used later for in vitro experiments.

The last step for finalizing the fabrication of the master is silanization of the etched wafer. This step ensures that the cast PDMS will not stick permanently to the silicon master during the production of negative molds. The wafer is placed in a desiccator jar along with few drops of the silanizing agent 1H-1H-2H-2H-perfluoro-octyl-dimethylchlorosilane (Sigma-aldrich). The jar is put under weak vacuum for 20 h. The vaporization of the silanizing agent forms a self-assembled monolayer of silane on the silicon surfaces, protecting them durably from unwanted interactions.

The positive Si masters prepared with this process can be used repeatedly to cast PDMS molds. The wafer can be diced into individual chips and reinforced with a hard baking in order to ease the handling. Figure 2.7 shows different configurations of micropillar arrays etched in a silicon master.

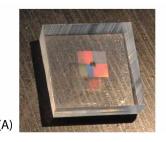
#### 2.2.3 PDMS micropillar substrates

Negative molds Stamps with the negative image of the micropillars first need to be created from the master. They were formed as a relatively thick piece of PDMS (1 cm) in order to facilitate their manipulation during the casting of replicas. For this, the masters are first placed in an adequate container, typically formed with aluminium foil. PDMS (Sylgard 184, Dow Corning) is mixed at a 10:1 weight ratio of base to curing agent, and poured over the master. Air bubbles are inevitably trapped between the master and the uncured PDMS. The container has to be degassed in a vacuum desiccator for at least 10 min or as long as bubble are visible. The PDMS is then cured by placing the container in an oven at 80 °C for at least 2 h.

Once cured and peeled from the master, the PDMS negative molds are cut to the appropriate

shape, typically a square of  $1\text{-}2\,\mathrm{cm}^2$  of surface (Fig.2.6 A). As for the master, the molds have to be silanized to avoid sticking of PDMS upon curing. For this, the surface of the molds are first activated with a short exposure to an oxygen plasma (Plasma Harrick,  $300~\mathrm{mTorr}~\mathrm{O}_2,~29~\mathrm{W},~25~\mathrm{s}$ ). Within 30 minutes from the plasma activation, the molds are silanized. The same procedure as for the master is followed, i.e overnight incubation in a vacuum desiccator.

Final substrates For in vitro experiments, the micropillar arrays were patterned on top of fine borosilicate cover slips, conventionally used for microscopy. This allowed the observation of the samples with high-magnification objectives having working distance down to  $150 \, \mu m$ . The cover slips should fit in petri dish used for cell culture. In most cases,  $24x24 \, mm^2$  cover slips were chosen (Menzel,thickness no1) fitting in conventional  $35 \, mm$  diameter dishes (Falcon BD) for tissue culture (Fig.2.6 B).



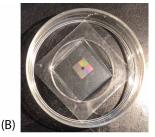


Figure 2.6 – Negative mold and a micropillar substrate mounted on a petri dish Photographic illustrations of a negative PDMS mold (A) and final substrate ready for cell culture (B). Micropillars printed on a coverslip are mounted in a petri dish with central hole for high resolution microscopy.

Parameters for the preparation and the curing of the final PDMS were strictly controlled in order to ensure the reproducibility of the mechanical characteristics of the polymer. The most important parameters in this process are the ratio base to curing agent, the temperature and duration of curing. A PDMS mixture of precisely 10:1 is prepared and degassed for 10 min in a desiccator to remove trapped air. Negative molds are placed with their patterned surface facing upwards and a drop of uncrued PDMS mixture is deposited on their surface. An additional degassing step of 10 min is needed to ensure good penetration of the liquid PDMS in the small cavities of the mold. The molds are then pressed against the cover slips, which are placed in a flat glass plate beforehand. The manual pressure applied on the molds has to be as uniform as possible in order to ensure the most consistent thickness of PDMS. The PDMS which is squeezed out forms a ring around the mold upon curing. This is used to confine liquid on the test surface during the preparation of in vitro experiments.

The substrates are cured at 80 °C for 16 hours  $\pm$  2 h. For the release of the microstructures,

the mold-substrate assemblies are first immersed in isopropanol (IPA). This prevents the collapse of high aspect ratio micropillars upon mold removal, which would occur in dry environment. The molds are readily detached from substrates by gently peeling off with fine tweezers. The molds can be reused several times to pattern additional replicas. While still in IPA, the substrates are sonicated for 5 min at 80 kHz in an ultrasonic cleaner bath (Fischerbrand 11205). This step allows to release to an upright position of pillars that remained collapsed. It also detaches particles that might be stuck on PDMS, thereby providing cleaner surfaces. Soaking the replicas in IPA has the additional advantage to leach out potential uncrosslinked PDMS oligomers which could contaminate cell culture medium.

Subsequent treatment of the substrates depended on the experimental design. If the substrates did not need to be exposed to air, they were directly transferred from IPA to 70 % ethanol for sterilization before cell culture. However, if the substrates needed to be exposed to dry environment, a critical point drying was performed to avoid collapsing of the micropillars. For this, the substrate are transferred to pure ethanol and placed inside the chamber of a critical point drier (Leica EM CPD300). The ethanol is replaced with liquid  $\rm CO_2$  at 6 MPa, and pressure and temperature are raised beyond 7.39 MPa and 31 °C to reach the supercritical state. The pressure is then decreased, turning the  $\rm CO_2$  into gaseous phase without crossing the phase boundary between liquid and gas. With this process, the pillars do not experience capillary forces due to liquid evaporation and are left in their upright position.

The sterilized substrates were stored in petri dishes at 4 °C for up to one week before in vitro experiments.

#### 2.2.4 Characterization

The process of fabrication was monitored closely after each step. The fidelity of features was assessed after Cr etching on the photomasks, after photoresist development on Si wafers, after etching of the master with DRIE, and after replica molding for the final PDMS structures. Several techniques were used for the different steps. Optical microscopy was used for quick inspection at all steps, and for measuring dimensions of arrays on photomasks and patterned resist on Si wafers. Scanning electron microscopy was the primary technique for the measurements of micropillars dimensions both at the level of the silicon master and final PDMS microstructures. It also allowed to determine the outcome of the DRIE on the Si master in terms of pillar shape, verticality, scalloping effect and surface roughness. Images from the Si masters were obtained with the Zeiss MERLIN

or Zeiss LEO 1550 systems. Figure 2.7 shows examples of SEM pictures from different configurations on the silicon master. PDMS pillars samples had to be coated with a layer of sputtered gold before imaging with the SEM. Images were obtained with a Phillips XL 30-FEG SEM. Examples of such images can be seen on Figure 2.8.

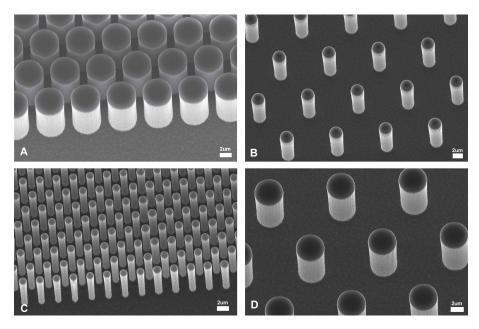


Figure 2.7 - SEM pictures of micropillars etched in a silicon wafer.

The diameter and spacing of pillars were determined on SEM pictures taken from profile or top views. Heights of pillars were measured with a technique based on white light coherence scanning interferometry (CSI). The technique can build three-dimensional surface profiles with nanoscale resolution in the vertical axis. CSI was used to measure height of Si master and PDMS pillars. Samples have to be light reflective for the measurements, thus PDMS pillars were coated with gold in the same way as for SEM preparation. Optical profiling data was obtained with Veeco Wyko NT1100 system, in the vertical scanning mode (vertical and lateral resolution were 3 nm and 550 nm respectively). Figure 2.9 illustrate the three-dimensional data and rendering obtained with CSI measurements. For the dimensions of final PDMS pillars, a minimum of 10 randomly chosen pillars were measured and averaged from SEM images or CSI data.

#### 2.2.5 Results

The outcome of the fabrication process showed significant differences compared to the initial digital design. Some configurations were particularly difficult, or even impossible, to obtain. The difficulty increased with the resolution of features: Small interpillar gaps of  $1 \,\mu m$  were most often not resolved, in particular for pillars with  $1 \,\mu m$  diameter. Improvements could be achieved for a particular configuration by optimizing photolithography and etching.

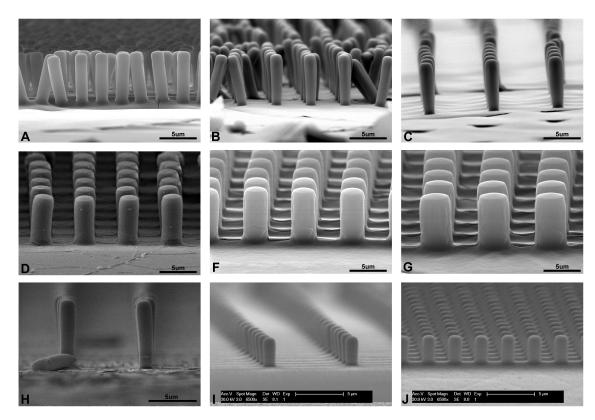


Figure 2.8 – SEM pictures of micropillars molded in PDMS by REM. Configurations from Chip 1 and 9 are represented: A) S2, B) S4, C) S8, D) D2, F) D3, G) D4. Comparison of pillar heights: H) 8 μm; I,J) 4 μm.

However, it was generally at the expense of other configurations, or induced unwanted artifacts. A process which gave satisfying results for the pillars with small diameter was chosen. Most of the configurations were well defined, with exception of configurations with S=1  $\mu$ m. Small variations occurred between Si masters, but the general trend for all configurations was larger diameters and smaller spacings than intended on the design. The offset values were between 0.05 to 1  $\mu$ m, depending on the configuration. Larger diameters translate to higher pillar spring constant, which can be counterbalanced by augmenting the height of the pillars.

The etching process was not entirely homogenous across the wafer. Significant variations in height were observed between chips and between arrays, with up to  $2\,\mu\mathrm{m}$  of difference between the extremum. Inter-chip variations came from differential etch rate dependant on the localization on the wafer, with the periphery regions being etched faster than the center. Inter-array variations came from differences of areas to be etched. The difference was significant for dense arrays (S= $2\,\mu\mathrm{m}$ ) which had slower etch rates.

The PDMS molding process resulted in high fidelity replication of the micro-structures. The dimensions of final PDMS pillars were not significantly different from the dimensions observed on Si masters. Table 2.3 shows the dimensions of PDMS pillars from Chips 1 and

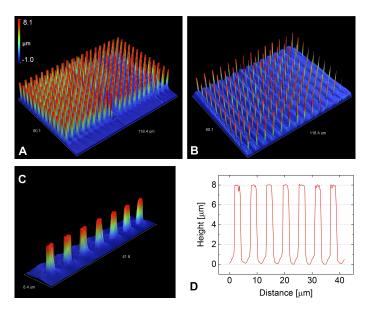


Figure 2.9 – CSI pictures. Representative images from the data acquired with coherence scanning interferometry. 3D rendering of the scanned surface of a D2 configuration (A) and S4 configuration (B). C) close-up of a region from (A). D) 2D profile of (C).

9, which were the most used for in vitro studies.

The shape of final pillars were close to cylindrical, with relatively smooth sidewalls. A slight decrease of diameter was generally observed at the lower part of pillar shafts. The effect became less noticeable for configurations with larger diameter and smaller spacing. Typically, a difference between 0 to 10 % was observed for configuration with  $S=2 \mu m$  or with  $D>1 \mu m$ . It increased up to 25 % for  $D=1 \mu m$ ,  $S=8 \mu m$ .

The spacing between pillars was slightly different between the x and y direction of the arrays. The difference was not found to depend on the configuration of the arrays and typically ranged between 0.15 to 0.36  $\mu$ m. For S8 configurations, this constituted only a few percent of difference. However, for S2 configurations, which were in fact smaller than 2  $\mu$ m, this discrepancy increased to 20% of difference between spacings of the two axis. Such variation was found to have an impact on the guidance of neurites, as described in the next chapter.

Table 2.3 shows the dimensions obtained for micropillars on the Chips 1 and 9 from the Si master with  $10 \,\mu m$  etch depth. These configurations were the most used for the in vitro experiments.

#### 2.2.6 Discussion

The dimensions of the design and the presence of multiple configurations on the same wafer constituted serious challenges for the fabrication process. The most demanding array

Table 2.3 - Dimensions of micropillars configurations on Chip 1 and Chip 9.

Chip 9				
Array:	D1	D2	D3	D4
Diameter, D [μm]	$1.2 \pm 0.1$	$2.2 \pm 0.1$	$3.2 \pm 0.1$	$4.2 \pm 0.2$
Height, H [µm]	$10.3 \pm 0.2$	$10.3 \pm 0.1$	$10.3 \pm 0.1$	$10.3 \pm 0.2$
Spacing in $x$ , $Sx$ [ $\mu m$ ]	$2.9 \pm 0.2$	$3.0 \pm 0.1$	$2.9 \pm 0.1$	$3.0 \pm 0.1$
Spacing in y, Sy [µm]	$3.2\pm0.1$	$3.2\pm0.2$	$3.2\pm0.1$	$3.2\pm0.1$
Chip 1				
Array:	S2	S4	S8	
Diameter, D [μm]	$1.5 \pm 0.1$	$1.2 \pm 0.1$	$1.3 \pm 0.1$	
Height, H [µm]	$9.4 \pm 0.2$	$10.3 \pm 0.2$	$10.3 \pm 0.2$	
Spacing in $x$ , $Sx$ [ $\mu m$ ]	$1.0\pm0.1$	$3.3 \pm 0.1$	$7.3 \pm 0.4$	
Spacing in y, Sy [µm]	$1.1\pm0.1$	$3.6\pm1.3$	$7.6\pm0.1$	

from the layout featured dots of 1 µm spaced by a gap of 1 µm. This requires to pattern 1 million dots on 4 mm<sup>2</sup> for the sole array S1. The principal bottleneck for this process was the equipments and technologies that were used. For the writing of the photomask, the system had a 0.8 µm spot size in the ideal case, which is almost at the level of the design's CD. In practice, many iterations were required in order to obtain acceptable results. Parameters like the energy of the laser and the shape of feature on the digital file were optimized to the best possible outcome. Another limitation stands with the contact photolithography system used. In contact printing mode, the resolution is limited by the thickness of the resist and the diffraction of light. The problem of diffraction is particularly relevant in the case of dense arrays of periodic elements, which create a diffraction grating. Indeed, some attempts resulted in pillars with holes in their center, due to the diffraction pattern. The next difficulty resides in the adhesion of the resist to the wafer. During the development, the very small dots of resist often detached from the surface, resulting in truncated arrays. The exposure time was decreased below the recommended light dose in order to counterbalance this effect. However, development time had to be increased and the fidelity of features was affected. The diameter of pillars was larger than expected and the spacing was smaller, due to less efficient dissolution of the resist. At this point, all configurations with S=1 µm were not resolved.

The etching process is another critical step which demanded optimization. In DRIE, the verticality of etched walls can be affected by the high aspect ratio of features. Incomplete removal of polymer bottom layer by  ${\rm SF_5}^+$  ions is amplified at each step, leading to inclined walls. Other artifacts of DRIE that were observed include: undulating vertical walls (scalloping), vertical ridges due to mask roughness, bottom roughness or "silicon grass" effect, due to micro-masking from contaminants or redeposited mask material. These

problems can be reduced by modulating process parameters such as source power, gas flow, pulse durations and substrate temperature. Good results were obtained, with relatively smooth surfaces and few artifacts. The verticality of sidewalls was satisfying, even if slight negative angle were observed for sparse configurations. The heterogeneity of pillar array configurations resulted in local variations of etching rate. Aspect Ratio Dependant Etching (ARDE) is a well known phenomenon which was most probably responsible for these differences. ARDE results from gas transport limitation: the availability of etching species is reduced at the bottom of high aspect ratio structures relative to lower aspect ratio structures, leading to slower etching. As a result, the height of pillars from configurations with  $S=2\,\mu m$  were more shallow than the S4 and S8. The same Si master was used to produce all the samples with a certain height, in order to ensure a high reproducibility of the pillar spring constants.

The production of a Si master with positive structures instead of negative ones, i.e pillars instead of pits, was chosen. It induces the need for an additional molding step for fabricating the final PDMS pillars. However, this strategy has several advantages: 1) the use of the Si master is minimized by reusing the same PDMS negative molds 5 to 10 times. This reduces the probability to damage the master, which is difficult and costly to replace. 2) the flexibility of the negative molds allows for easier release when peeling away from stiff coverslip used for in vitro studies. 3) the deformability of negative molds permit to pattern features on a non-planar surface. This was crucial for patterning the inner lumen of the tubes for in vivo experiments in Chapter 4.

Out of the nine chips that can be simultaneously produced with the Si master, only chips 1 and 9 with H=10 µm were extensively used for the subsequent in vitro studies. The chips 1 and 9 were chosen for their variations of spacing and diameter, allowing to probe both effects on a range of values. Restrictions of time and objective prevented the use of the entire scope of configurations in the frame of this thesis. For future works, the design of the Si master is amenable for implementation with a high-throughput system, where automated data acquisition could readily probe the full spectrum of arrays.

In conclusion, possible directions for ameliorating the fabrication of pillars could include photomasks written with higher resolution (from commercial source for instance) and use of a projection photolithography system such as a stepper. Other technologies such as e-beam or x-ray lithography for direct writing of photoresist, or focused ion beam milling could be used to achieve pillar with diameter in the nanometer range. However these technologies have a relatively low throughout and are more difficult to implement.

# PDMS Surface functionalization

# 2.3.1 Tailoring the proprieties of PDMS surfaces

PDMS is intrinsically hydrophobic due to the methyl groups covering its surfaces [45]. This results in poor adhesion of cells on pristine PDMS surfaces [46]. Compared to other cell types, neurons are particularly sensitive to their physical environment and bind weakly to substrates not specifically prepared. In preliminary cultures experiments, DRG-derived cells were unable to attach to untreated PDMS substrates. To overcome this limitation, surface functionalization was performed to make the substrates suitable for cellular adhesion and growth.

Surface functionalization includes any sort of treatment resulting in the addition of chemical functional groups at the surface of the material. By extension, bio-functionalization concerns modifications intended for increasing cellular adhesion and biocompatibility. Activation of PDMS is a widely used treatment which replaces CH<sub>3</sub> groups by -OH groups on the surface [47]. Exposure to oxidising species from oxygen plasma or UV source make PDMS hydrophilic to varying extents, depending on the treatment duration and other process parameters. Mainly used for silanization and bonding purposes, it was shown to improve cell attachment compared to unoxidized PDMS [46]. A side effect of this treatment is the potential apparition of a thin silicate layer, which potentially increases the stiffness of the surface [47].

Common strategies for PDMS bio-functionalization rely on extracellular matrix (ECM) coatings, with proteins such as fibronectin, laminin or collagen. The most straight-forward method is to let the proteins adsorb by hydrophobic interactions with the PDMS surface [48]. This technique was chosen for coating the micropillar substrate in the in vitro studies of this thesis. Other methods include electrostatic coating with oppositely charged polyelectrolytes layers [49], or covalent immobilization of proteins through various chemical reactions [50, 51].

The bioactivity of the bound molecules can be affected by the coating technique and the

conditions imposed to the sample. Uncontrolled adsorption of proteins on the surface may alter their biological activity by steric hinderance. The homogeneity of the coating, its stability in aqueous medium or its resistance to mechanical deformation are parameters which may ultimately affect the growth of cells. Optimal coating procedure can be empirically determined for specific proteins and culture conditions.

## 2.3.2 Functionalization of PDMS micropillar substrates

In order for neurons and neurites to adhere in vitro, micropillar substrates were coated with two successive layers of molecules: Poly-D-lysine (PDL) and laminin (LN). PDL is an amino acid-derived polymer widely used for enhancing the adhesion of cells on plastic petri dishes. PDL coating induces a net positive charge on the surface, which promotes the binding of cells through electrostatic interactions with negative ions of the cell membrane.

Laminins are a family of ECM glycoproteins which are an essential component of the basement membrane architecture [52]. With numerous functional domains, laminins are known to modulate important aspects of cell behaviour such as adhesion, growth, migration and survival [53]. Laminins play an important role in neural development and regeneration, by providing guidance for axons and promoting neurite outgrowth and neuronal migration [54]. The influence of laminin was demonstrated in vitro as well, and LN coatings are regularly used for promoting neurite outgrowth on various substrates [55].

From experimental observations, the combination of PDL and LN was found to support best the adhesion of cells and the growth of neurite networks. Fig.2.10 shows representative images of the outcomes of DRG cell culture on flat PDMS coated with PDL only or a combination of PDL + LN. PDL on its own was sufficient for the attachment and survival of non-neuronal cells on PDMS. Small neurites emerged from the few neurons which can be seen on PDL coated samples. The addition of the LN coating resulted in higher number of cells, and neurons harbored prominent neurite outgrowths.

## 2.3.3 Coating strategy

Two approaches were tested for functionalization of micropillar substrates: Either coating the entire surface area, or printing the molecules only the top surface of the pillars (Fig.2.11). The latter option has the advantage of restraining the cells on the top of pillars. Repulsive molecules can be deposited on the bottom and shaft walls to further prevent cell crawling in between pillars. This selective coating is particularly useful for biophysical studies. Cells can be patterned into specific shapes on pillars by controlling the spatial deposition of

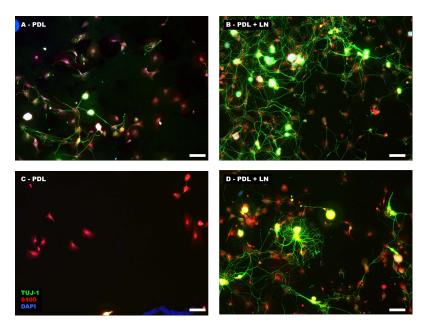


Figure 2.10 – Comparison between PDL and LN coatings on DRG cells. Fluorescence images from DRG-derived cells cultured on coated PDMS substrates. Flat PDMS samples were coated either with PDL only (A,C) or PDL+LN (B,D). Cells were cultured for 3 days in vitro, fixed with paraformaldehyde (PFA) and immunostained for neurons (TUJ-1, Green) and Schwann cells (S100, Red). Nuclei were labeled with DAPI (Blue). Scale bars=75 µm.

ECM proteins. Moreover, the mechanical feedback sensed by cells is entirely given by pillar deflection since focal adhesions are restricted to pillar top surfaces. However, this method has a number of limitations. First, the microcontact printing process showed large variations in terms of deposited proteins. Homogenous deposition was hardly controllable and zones of poorly coated pillar tops often present (Fig.2.12). A dependance on pillar diameter was found, with smaller diameter absorbing less proteins per surface area than larger ones. More globally, such coating might be of limited relevance as a model for in vivo cell-material interactions. For an implanted interface, the effect of repulsive molecules along pillar shafts will likely be annihilated by the deposition of ECM proteins from the surrounding environment. Ultimately, cells will be able to invade the entire pillar geometry.

For these reasons, micropillar substrates were coated unspecifically on their entire surface with PDL then LN.

## 2.3.4 Absorption of Poly-lysine and Laminin on PDMS

#### PDL

The effect of plasma oxidation, incubation time and temperature on the deposition of poly-lysine were investigated. A fluorescently labelled version of poly-lysine was used to quantify the amount of deposited protein. Poly-L-lysine instead of poly-D-Lysine had to

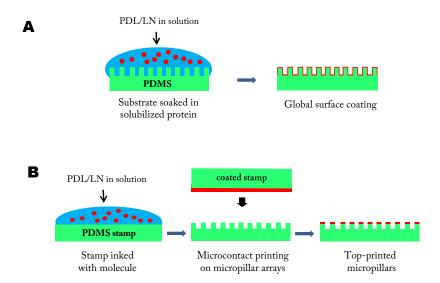


Figure 2.11 – Global vs selective coating of micropillars. Schematic of two strategies for the functionalization of PDMS micropillar substrates. A) Molecules in solution are absorbed to the surface of PDMS, coating the entire surface area. B) Molecules are absorbed on a PDMS stamp, which is brought in contact with the micropillar arrays. The molecules are selectively transferred to the top surface of micropillars.

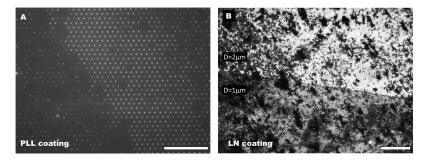


Figure 2.12 – Examples of defects of pillar tops-printed molecules Micrographs showing the fluorescence signal of poly-lysin and Laminin printed on the tops of micropillars by microcontact printing. Poly-lysin was conjugated with FITC and LN was detected by immunofluorescence. The transfer of molecules is less efficient on pillars with small diameters, as shown on the right figure. Scale bars are 100 µm.

be chosen due to unavailability of the PDL form.

Protocol Slabs of flat PDMS were prepared with the same protocol as for micropillars. Plasma treated samples were exposed to an oxygen plasma (Plasma Harrick, 300mTorr O<sup>2</sup>, 29 Watts, 30 sec). The FITC-PLL (sigma) was dissolved at 100 μg ml<sup>-1</sup> in H<sub>2</sub>O. A drop of 200 μl of solution was placed on the PDMS slabs and incubated with different conditions. The fluorescence of FITC-PLL was detected by taking picture with a microscope (Zeiss Axioplan, 10x objective) equipped with a band pass filter for green light (515-565 nm. The exposure time was kept constant. The fluorescence intensity on pictures was quantified by calculating the average pixel values on region of interests of 300x300pixels.

**Results** Fig.2.13 presents the levels of molecule absorbtion expressed in fluorescence intensity. The plasma treatment doubled the absorption of the PLL compared to untreated samples for all four conditions. Increasing the incubation time from 1h to 2h resulted in appreciably higher amounts of absorbed PLL. Overnight incubation (ca. 20 hours) resulted in slightly higher absorption for the non-plasma treated samples. Finally, O/N incubation at 4 °C seems preferable to 37 °C.

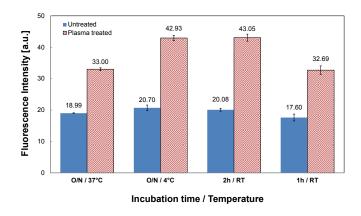


Figure 2.13 – Absorption of Poly-L-lysine on PDMS substrates. Graph depicting the effect of different treatment modalities on the absorption of PLL-FITC. Bars represent the mean fluorescence of absorbed FITC-labeled poly-L-lysin and error bars the standard deviation.

#### Laminin

The homogeneity and relative amounts of absorbed laminin were compared between PDMS, glass, and polystyrene (PS) substrates. Untreated and plasma-exposed samples were also compared.

Protocol PDMS samples were prepared with the same procedure as for micropillars substrates. Standard cover slips and perti dishes were used as glass and PS substrates. Plasma treated samples were exposed to an oxygen plasma (Plasma Harrick, 300mTorr O², 29 Watts, 30 sec). All samples were incubated in 100 μg ml<sup>-1</sup> of PDL overnight at 4 °C. Samples were washed with H<sub>2</sub>O 3 times for 5 min. Laminin extracted from murine sarcoma (sigma) was solubilized in PBS to a final concentration of 20 μg ml<sup>-1</sup>. A drop of 150 μl of LN solution was placed on samples and let to incubate for 3 hours at 37 °C in an incubator. Samples were washed with PBS and stained by immunofluorescence. Briefly, after 1 hour of incubation in blocking buffer (2 % goat serum, 1 % BSA), an anti-laminin antibody (sigma) was applied to sample overnight at 4 °C. After washing with PBS, the secondary antibody was applied on samples for 1 hour and washed extensively. Samples were imaged at fixed exposure time with a fluorescent microscope (Leica DM6600) with

a 10x objective and appropriate filters. The amount of absorbed LN was quantified by extracting the mean intensity of fluorescent signal on 5 fields of view (500x500 pixels) per samples across 2 to 3 independent samples.

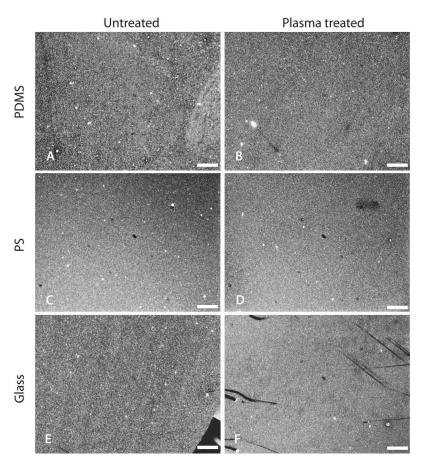


Figure 2.14 – Laminin coating imaged by immunofluorescence. Representative micrographs of LN absorption on PDMS, Glass and Polystyrene (PS). Images in the left column are from untreated samples and on the right from plasma treated ones. The brightness of images was normalized on these pictures. Scale bars are  $100\,\mu\text{m}$ .

Results The morphology of the films of absorbed LN showed granular aspect (Fig.2.14). Plasma treated samples had finer and denser morphologies than non-treated. The PDMS and glass samples were comparable, and PS had the most uniform and fine aspect. With the exception of scratches on glass samples, most samples were uniformly coated, without important inhomogeneities.

The absorption of LN was comparable between PDMS and Glass substrates (Fig.2.15). Plastic dishes in PS absorbed significantly more LN, with fluorescence signals 4 to 7 times higher. Like for the poly-lysine, plasma treated sample exhibited higher amounts of absorbed laminin compared to untreated ones. We conclude that this kind of treatment is efficient for increasing the absorbtion of molecules to commonly used substrate materials. However, untreated samples still absorb a fair amount of molecules, as they are almost

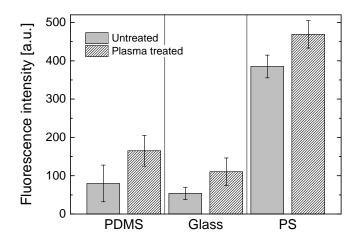


Figure 2.15 – Absorption of Laminin on PDMS, Glass and PS. Bars represent the mean fluorescence of absorbed LN detected by immunofluorescence and error bars the standard deviation.

within the error range with their plasma treated counterparts. Plasma treatment has the disadvantage to stiffen the PDMS surface by producing a thin silicate layer on its top. Moreover, plasma treatment requires to place the samples in dry environment, which is problematic for micropillar arrays. For these reasons, the samples were finally left untreated for in vitro studies.

The definitive coating protocol was based used for most in vitro studies was:

- 1. incubation with  $100 \,\mathrm{\mu g} \,\mathrm{ml}^{-1}$  of PDL (sigma P6407) in  $\mathrm{H}_2\mathrm{O}$  at  $4\,^{\circ}\mathrm{C}$  overnight
- 2. washing 2 times with H<sub>2</sub>O and 1 time with PBS, for 5 minutes each
- 3. incubation with 20 μg ml<sup>-1</sup> of LN (sigma L2020) in PBS for 3 to 4 hours at 37 °C
- 4. washing once with PBS to remove unabsorbed LN

# Mechanical behaviour of micropillars

The flexible geometry of PDMS micropillars provide mechanical properties to the substrate which differ greatly from a continuous planar surface. For cells, who constantly probe their environment, these properties alter mechanosensing mechanisms and may have implications on cellular behaviour. Therefore, the mechanical properties of micropillars have to be carefully assessed. In this section, the behaviour of pillars under bending is characterized with an analytical model and with an finite element method (FEM).

## 2.4.1 Analytical model

The application of a force by a cell on a pillar can be modeled as a load applied to the central point of the top surface of the beam, perpendicularly to its longitudinal axis (Fig.2.16). The resulting deformation of the pillar is a function of its dimensions and of the bulk elastic modulus of the PDMS.

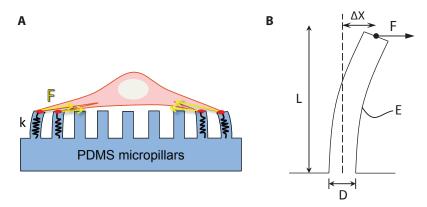


Figure 2.16 – Analytical model of a pillar bend by cellular force. A) Schematic representation of a cell probing its environment by exerting traction forces F on micropillars. The pillars can be considered as vertical springs with constant k. B) Sketch of a pillar deformed by a force F applied to its top. Parameters: L=pillar length, D=pillar diameter,  $\Delta x$ =displacement of the central point of the pillar tip, E=Young's modulus of the bulk material.

If we consider the pillar as a linear elastic material (with Poisson ratio  $\nu$ =0.5), a reasonable estimation can be obtained with the classical Euler-Bernoulli beam theory approximation. Micropillars are modeled as cantilever beams, fixed at one extremity, and subjected to a

point load on the free extremity. Under pure bending regime, the displacement  $\Delta x$  of the tip of the beam is given by Equation 2.1:

$$\Delta x = \left(\frac{L^3}{3EI}\right)F\tag{2.1}$$

where I is the area moment of inertia of the beam, L is the length of the beam, E is the Young's modulus of the beam bulk material and F the force applied. If we consider pillars as ideal cylinders, the area moment of inertia for a circular cross section is given by  $I = \frac{1}{64}\pi D^4$ , where D is the diameter of the circle. Equation 2.1 then becomes:

$$\Delta x = \left(\frac{64L^3}{3\pi E D^4}\right) F\tag{2.2}$$

In this model, the micropillars behave like ideal springs, with deflection directly proportional to applied force. From Hooke's law, the spring constant k of pillars is given by  $k = F/\Delta x$ . An expression for these spring constants can be derived from Equation 2.2:

$$k = \frac{3\pi E D^4}{64L^3} \tag{2.3}$$

Spring constants quantify the stiffness of pillars from their geometric dimensions and bulk Young's modulus. However, this model is only valid within certain limits. Most importantly it should be applied to small deflection of pillars in order to stay in the linear range. The aspect ratio (AR) of micropillar is determinant for this question. If the AR is too large, typically over 8, the deformation cannot be considered linear anymore. On the other hand, if the AR is too small, typically below 2, mechanical deformation of the pillar includes a shear component, in addition to bending. An other limitation is found with the boundary conditions. The model assumes that the beam is fixed on a completely rigid substrate, which is not the case with PDMS. Correction factors for the wrapping of the substrate at the base of the pillars have been proposed to account for this effect [56].

Validation of micropillar spring constants has been demonstrated with an experimental method relying on glass micropipette of calibrated stiffness [29]. Piezo micromanipulators are used to pushed the tip of the pipette against the tip of a single micropillar. Measuring the displacement of the pipette and pillar tips allows to calculate the spring constant of the pillar. This technique was applied on micropillars with relatively large dimensions,

typically D=3  $\mu$ m and L=10  $\mu$ m [29, 57]. However, pillars with small diameter (<1.5  $\mu$ m) and high AR would make this method much more difficult to execute. First, glass pipette tips might be too stiff for being deflected by high AR pillar. Secondly, the tip of the pipette might be to large to be correctly positioned against pillar with small diameters. The softest micropillars fabricated here correspond to this case. Therefore the estimation of spring constant with this method will not be efficient for those configurations.

# 2.4.2 Finite Element Method (FEM) analysis

In order to provide more accurate estimations of spring constants for all dimensions of micropillars, Finite element modeling (FEM) simulations were performed. It allowed the comparison with the values obtained from the analytical model. The analysis concentrated on the Chip 1 and Chip 9 configurations, as those were fully characterized under section 2.2.4. The simulation software Comsol Multiphysics was used for the FEM analysis. A neo-Hookean hyperelastic model was chosen to simulate the mechanical behaviour of PDMS. The micropillars were modeled as cylindric structures composed of fine hexahedral mesh elements, with one fixed extremity as boundary condition. The shape of these structures corresponded to the dimensions of micropillars measured from SEM and CSI data in previous sections. The elastic modulus of bulk PDMS was experimentally determined by stretching assays. For our standard preparation protocol (1:10 mix, 80 °C for 16 h),  $E_{PDMS} = 1.95 \,\mathrm{MPa} \pm 0.07 \,\mathrm{(n=12)}.$ 

The mechanical behaviour of micropillars was simulated for traction loads applied on the entire top surface, perpendicularly to the longitudinal axis of the pillars. The deflection of pillars was quantified by the displacement of the central node of the top surface. The spring constants of micropillars were computed from the slopes of the Force-displacement curves obtained with these simulations. The graph on Fig.2.17 A shows the force-displacement plot for micropillar configuration D1 to D4, which have distinct stiffness. The slopes of the curves were determined as the displacement approached zero. Spring constants were calculated for configurations on Chip 1 and 9. The graph on Fig.2.17 B plots the spring constants obtained by FEM simulation, as well as the curve corresponding to Equation 2.3, from the analytical model. Table 2.4 summarize the numerical values for k and quantifies the difference between the two calculation methods.

One can observe that both values were in good agreement for all configurations. The biggest difference (3.3%) was observed for D4, which has the lowest aspect ratio. The beam theory does not account for compressive effect or shear component due to the applied force. Therefore, the FEM simulations constitute better approximations of the spring constant

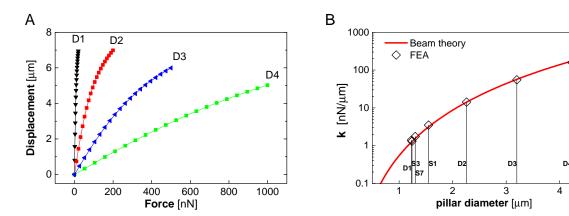


Figure 2.17 – Characterization of pillar mechanics with FEM simulations A)Force-displacement curves for pillars with different diameters (D1 to D4 configurations). B) Spring constants of micropillars calculated with FEM and elastic beam theory. The graph shows k as function of the diameter of micropillars. Black diamonds represent the data obtained with FEM simulations. The red curve is derived from the analytical model (Equ.2.3).

Table 2.4 – Spring constants obtained analytically and with FEM simulation.

		D1	<b>D2</b>	<b>D</b> 3	<b>D4</b>	S1	<b>S</b> 3	<b>S7</b>
Aspect ratio	L/D	8.6	4.7	3.2	2.5	6.3	8.6	7.9
k  (analytical) $k  (FEM)$	-							
Difference	%	1.8	1.1	0.5	3.3	1.7	1.8	2.7

for these pillars. A limitation of the FEM simulation is found with the hypothesis of a fixed extremity for the base of pillars. In reality, the PDMS bottom surface may slightly deform by tilting in the vertical plane upon pillar flexion. Thus, the spring constants of the stiffest micropillars might be subjected to overestimation.

Using FEM analysis, the behaviour of pillars with different flexibilities was observed upon bending. A fixed load of 20 nN was applied to pillars from the D1 to D4 arrays. This load is in the range of forces applied by diverse types of cells, as previously reported in the literature [58, 59]. The resulting deformations are showed on Fig.2.18. The 3D representation of deformed pillars demonstrates well the effect of diameter variation on pillar deflection. We can notably observe that the pillar from D1 configuration is not in the linear regime of small deformations. Thus, the D1 array may be irrelevant as substrate for cells exerting forces in that range. However, much lower forces were also reported for cell pulling on pillars, and therefore D1 is not discarded for in vitro experiments.

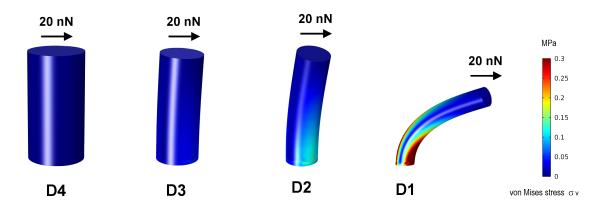


Figure 2.18 – FEM simulations of micropillar deformation. 3D representations of FEM-modelled pillars from Chip 9, deflected by a  $20\,\mathrm{nN}$  load applied to their top surface. The distribution of the von Mises stress along pillars is shown by color-coded texturing of the strucutres.

# 2.4.3 Effective stiffness of micropillar surfaces

Most substrates used for studying cell biomechanics take the form of deformable continuous gels, such as polyacrylamide or agarose gels [60, 22]. In contrast, micropillar arrays present a discontinuous environment for cells evolving on their top, with discrete zones for adhesion. Spring constants provide a measure of the flexility of individual micropillars, but they can not be related to surface compliance expressed in Pascal units. Tan et al.([29]) proposed an approximation of the spring constant of a flat PDMS surface which was on the order of  $10\,000\,\mathrm{nN}\,\mu\mathrm{m}^{-1}$ . In comparison, the range of spring constants produced by micropillars on Chips 1 and 9 (0.5 -  $80\,\mathrm{nN}\,\mu\mathrm{m}^{-1}$ ) represented a decrease of 2 to 4 orders of magnitude.

In order to compare the surface stiffness produced by micropillar geometries to those from flat substrates, a model for the deformation applied by a cell on a continuous elastic plane has been proposed [59]. The shearing stress applied on the plane through a circular surface figured the traction force applied by a cell on a focal point. The displacement  $\Delta x$  at the center of the focal point in response to the applied force F was given by:

$$\Delta x = \frac{9Pr}{4E} \tag{2.4}$$

where P is the shearing stress, r the radius of the focal point and E the Young's modulus. Considering the total force applied on the focal point  $F = \pi r^2 P$ , and assuming that the area of the focal point is equal to the pillar top surface area, the effective Young's modulus  $E_{eff}$  is given by

$$E_{eff} = \left(\frac{9k}{2\pi D}\right) \tag{2.5}$$

where k is the spring constant of the pillar and D its diameter. With this model, the effective Young's moduli produced by the pillars on Chips 1 and 9 ranged between 0.7 to 27 kPa. In comparison, the Young's modulus of PDMS was measured at 1950 kPa. The range of stiffness produced on Chip 9 corresponds to elastic moduli found in soft tissues [21], and used in other studies to probe cellular mechanosensitivity [61, 62, 63]. However, with reported modulus down to a few hundreds of Pascals, the brain tissue remains an order of magnitude softer than the lowest modulus configuration [64].

The effective modulus values for each micropillar array are given on Table 2.5. These values served as a basis for the comparison of the results obtained in vitro in Chapter 3 with other studies using continuous substrates.

Table 2.5 – Effective Young's modulus  $E_{eff}$  for Chips 1 and 9.

		D1	$\mathbf{D2}$	D3	D4	S1	<b>S</b> 3	S7
Spring constant $k$	$\rm nN\mu m^{-1}$	0.6	6.2	27.5	79.2	1.8	0.6	0.8
Effective modulus $E_{eff}$	kPa	0.7	4.0	12.3	27.0	1.7	0.7	0.8

# Multilevel micropillar arrays

In this section, the fabrication of substrates presenting micropillars with different heights on the same chip is described. Two designs specifically were created: The so-called "4-level" design has 4 distinct zones with regular increase of pillar height, from 4 to  $12\,\mu m$ . The second design, named the "Stripe" design, features pillars with 2 different heights, which are grouped in parallel bands of  $20\,\mu m$  width. Most importantly the top surface of all micropillar remains coplanar.

#### 2.5.1 Rationale

The creation of substrates with multilevel structures has 2 main purposes here: First, from the mechanical perspective, the height of pillars is used, instead of the diameter, to modulate the stiffness of the surface. Secondly, multilevel structures allow integration of additional topographic cues, thus enriching the three-dimensional environment with new features.

The spring constant of micropillars is geometrically defined by both the diameter and the height dimensions. Creating designs with varying pillar diameters is straight-forward, as it only requires a specific photomask for the fabrication of a Si master. Photomasks with dots of varying dimensions are readily achievable with laser writing systems such as the one described earlier in this chapter. Arrays of micropillars with unidirectional gradient of increasing diameters have been used to study cell durotaxis [65, 66]. However, these studies acknowledged the impossibility to assess the influence of variations of top surface areas on cellular motility. More generally, it is recognized that the adhesive surface area, which is linked to the diameter and density of posts, will impact the way cells form focal adhesions (FA) with their substrates [67]. Thus, having uniform diameter of pillars ensures a constant top surface area available for FAs and eliminates the potential effect of varying ECM densities.

Since the pillar top surfaces have to be on the same level, the bottom surface has to be

varied in order to create different heights. Thus, steps are created on the bottom surface between zones of different pillar heights. In the case of a global surface coating, cells are able to explore the 3D environment. The presence of these topographic cues on the bottom surface may be sensed by cells which send protrusions to lower depths.

# 2.5.2 "4-levels" design

A schematic representation of the "4-levels" configuration can be found on Fig.2.19. The design features 4 different heights of pillars, 4,6,8 and 10 µm, which translates in 4 pillar stiffnesses. The spacing, diameter and arrangement of pillars is kept constant for all configurations on the chip. The zones define square areas of 25 mm², which are contiguous to each other. The total pillared surface of the chip forms a continuous square area of 100 mm², without separation between zone. Cells can thus transit between zones of different stiffness without apparent modification of the topography on top of pillars. This "4-levels" configuration was intended to be similar to the Chip 9 design, which also has 4 spring constant, modulated by diameter variations.

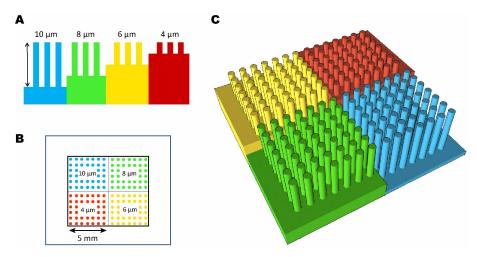


Figure 2.19 – Schematic of the "4-level" design. A) Side view of the design, showing the 4 heights of pillars with coplanar top surfaces. The sketch does not represent the real configuration: the 4 zones are placed side by side for visualization purpose. B) Top view of the chip, showing the arrangement of the zones. The surrounding flat surfaces are delimited by the external square which represent the total seeding surface. C) 3D representation of the center of the chip with color-coded heights of pillars.

# 2.5.3 "Stripes" design

Fig.2.20 shows a schematic representation of the "Stripes" design. Two different heights of pillar are present on the chip. They are arranged along bands of  $20 \,\mu m$  width which cover the entire surface of the pillared area  $(100 \, \text{mm}^2)$ . The topography on the bottom surface forms grooves and plateaus which are separated by a step corresponding to the

difference of pillar height, typically a few microns. The width of the bands was chosen to fit approximately the size of a cell. Therefore, a cell oriented perpendicularly to the axis of the bands will experience at least two different stiffness. If the cell body is located at the center of a band, its cytoplasmic protrusions will most probably both sense the opposite stiffness from the one experienced by the cell body. The behaviour of cells in this situation could give insights on the integration of conflicting mechanical cues by the cell. For instance, such design could assess if cells have a preferential stiffness to grow on. From a tissue engineering perspective, the rearrangement of the cytoplasm of the cell to fit on a specific zone of stiffness could produce large-scale orientation of cells in the direction of the bands. The orientation of Schwann cells was shown to influence the growth of axons [68, 69]. Thus, controlling the orientation of Schwann cells with stiffness or topography of the substrate would be a very valuable tool for improving the design of regenerative devices.

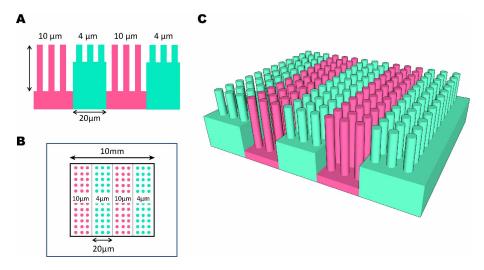


Figure 2.20 – Schematic of the "Stripe" design. A) Side view of the design. Alternating zones of short and tall pillars (4 and 10 µm) are arranged in bands of 20 µm width. The pillar top areas are coplanar, but the bottom surface is patterned with steps. B) Top view of the chip. The bands are covering the entire array, which is surrounded by flat surfaces. C) 3D representation of the "Stripe" configuration, with color-coded height of pillars.

#### 2.5.4 Fabrication process

The main steps of the process flow for producing multilevel designs are represented on the Fig.2.21. Most of the equipments used for this process are the same as those described under the Section 2.2.2.

To perform multiple etching steps on the bottom surface without altering the pillars, a mask resistant to the organic developer used to strip the photoresist is needed. A  $\mathrm{SiO}_2$  thin film was used to form a hard mask for producing the micropillar structures on the

Si wafer. The first step of the process was the patterning of the oxide mask into arrays of dots, with similar design as for classical micropillars. Si wafer with thermal wet oxide layers of 200 nm or 500 nm were purchased. The mask for initial etching of the  $SiO_2$  film was produced with similar conditions to the one created by the photolithography step under Section 2.2.2. Briefly, wafers were spin-coated with 1 µm of AZ ECI photoresist and exposed to the i-line UV light source of a mask aligner. The optimal light dose was found between 60-65 mJ cm<sup>-2</sup>. After development of the photoresist, the  $SiO_2$  was etched by RIE with  $C_2F_6$  as reactive gas. The result is a hard mask of silicon dioxide dots which protect the underlying silicon cylinders during the subsequent DRIE steps.

Once the  $SiO_2$  mask is patterned, the first silicon etching can be performed to define the height of the shortest micropillars (4 µm in this case). From that point, a new photolithography process is carried out for producing either the "4-level" or the "Stripe" designs. The latter is more straight-forward to fabricate since it requires only one additional photolithography step. For the "4-level" design, a total of 4 Si etch steps is needed. In both cases, new dedicated photomasks have to be created in order to pattern the photoresist to the desired shapes. The protocol for these photolithography steps differed from the one for pillars: 14 µm of AZ9260 was spin-coated on the wafers (EVG150 Automated Resist Processing System). Coated wafer were exposed to broadband light source of a mask aligner (Süss MA6), with light doses ranging from 280 to 400 mJ cm<sup>-2</sup>. The development was carried out in two steps: first an automated process (Süss DV10) with up to 14 min in the developer, and secondly a short oxygen plasma (1 min, 600 W, 400 ml/min  $O_2$ , Tepla300).

For the "Stripes" design, the photoresist is patterned to form bands of 20 µm and leave 20 µm of uncovered area. After the second DRIE step, the protected pillars remained at their initial height, while the shafts of pillars in the uncovered areas extended as the bottom surface was etched.

For the "4-levels" design, three additional photolithography steps are performed. In the first etch, the photoresist covers a square area of  $25\,\mathrm{mm^2}$ , corresponding to the quadrant of the chip with 4 µm tall pillars. A short Si etch lowers the global level of the wafer by a few microns, increasing the height of non-protected pillars. In DRIE rounds 2 and 3, the photoresist covers two and three quadrants respectively (50 and  $75\,\mathrm{mm^2}$ ), leaving the fourth quadrant exposed during all step. The final step before using the wafers as masters for PDMS molding is the removal of the SiO<sub>2</sub> hard mask by etching.

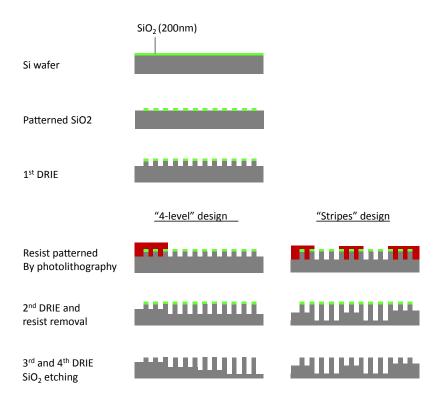


Figure 2.21 – Process flow for fabrication of multilevel pillars. The major steps for the fabrication of multilevel pillars are depicted. A description of these steps is found under the fabrication process section. After the first DRIE round, the wafer can be used to produce either the "4-level" or the "Stripes" designs.

#### 2.5.5 Results

The two multilevel designs were successfully fabricated on silicon wafers. The intimal patterning of the hard mask relied on process optimized previously for classical micropillars and was thus straight-forward. The additional photolithography steps were the most critical points, with the coating and development of resist on non-planar wafers. Short micropillars are already present on the wafers, and such high aspect ratio structures perturb greatly the formation of a homogenous layer of resist during spin-coating. Moreover, the photoresist has to be thick enough to cover the integrality of pillars and form a flat surface before exposure.

Thick layers of photoresist were thus deposited. It reduced the resolution of achievable features, but was sufficient to produce 20 µm trenches. The increased surface area created by the micropillar topography most probably resulted in strong adhesion with the wafer. This resulted in trapped photoresist chunks and uncomplete elimination after development or stripping. Short oxygen plasma treatments were implemented after the standard development recipe to ensure complete removal from the bottom surface in the middle of the arrays. Piranha cleaning was performed after DRIE to completely strip the photoresist.

Fig.2.22 shows representative SEM images of the "4 level" Si master, and Fig.2.23 the "Stripe" Si masters. A general observation is that the different steps of etching are visible on the shaft of micropillars. Although the DRIE protocols were identical, the sidewalls showed increased scalloping patterns from the second DRIE on. A slight reduction of pillar diameter is also noticeable at the beginning of each new DRIE. The homogeneity of micropillars dimensions in the x-y plan was very good, with no noticeable differences between arrays (Fig.2.22 C). The coplanarity of pillar surface was also maintained thanks to the resistance of the SiO<sub>2</sub> mask to the etch steps.

The dimensions of the different micropillars configurations of can be found on Table 2.6. Initially, step of 2 µm were designed for the "4 level" design. However the etch rate of the additional DRIE steps was faster than expected, and resulted in vertical steps of approximately 3 µm. The heights of tall micropillars in particular differed from the initial design. Two versions of the "Stripe" configuration were fabricated, with global difference of heights (Fig. 2.23).

Table 2.6 – Dimensions of the micropillars from multilevel designs.

$[\mu m]$	4-level	Stripes 9/4	Stripes $15/6$
Diameter	1.9	1.9	1.6
Spacing	1.2	2	2.4
Height 1	4.2	4.6	6.3
Height 2	6.6	8.9	14.4
Height 3	9.1		
Height 4	12.1		

The "4-leve" design was mostly destined to track the force applied by individual cells in vitro, on homogenous pillar diameters. Having every configuration in the same petri dish ensured identical experimental conditions for every probed cell. The "Stripe" design was intended to test if neurons and Schwann cell would align in the direction of the bands, due to topography or stiffness differences. This design was used in the in vivo part of this thesis, where a regenerative nerve tube was equipped with this texture.

The design of the multilevel substrates created here are relatively simple. However, this process could be used to pattern more complex configurations, with zones shaped into various forms, on the micro- and macroscopic scales. The differences of pillars spring constant in these zones would allow to pattern the stiffness of the substrate with a high resolution. One can imagine a design matching stiffness or topographic differences of relevant structures encountered by cells in vivo. For instance, shaping zone with the comparable stiffness and elongated morphology of Schwann cells could potentially induce faster directional axon elongation.

Table 2.7 - Mechanical characteristics of "4 levels" Chip.

"4 levels" Chip arrays		H4	H6	H8	H10
Aspect ratio	L/D	2.2	3.8	5.6	7.8
Spring constant (FEM) Effective modulus	nN μm <sup>-1</sup> kPa			2.7 2.3	

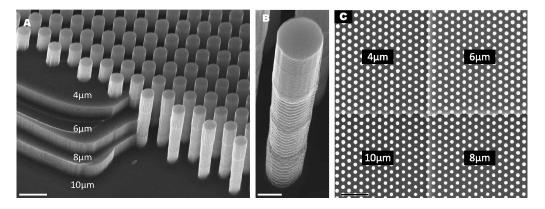


Figure 2.22 – SEM images of the "4 levels" Si master. Representative SEM images from chips present on the "4-levels" Si master. A) Intersection of zones with  $4\,\mu m$  and  $12\,\mu m$  tall pillars. The successive rounds of DRIE create vertical steps of  $3\,\mu m$ . B) High magnification image of a  $10\,\mu m$  tall micropillar. The 4 rounds of DRIE are visible on the scalloping patterns of the shaft. C) Top view of the central point of the array, where the 4 different heights of micropillars meet. Scale bars are:  $A{=}5\,\mu m$ ,  $B{=}1\,\mu m$ ,  $C{=}10\,\mu m$ .

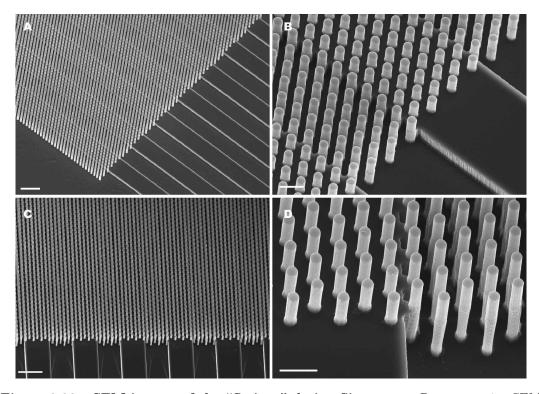


Figure 2.23 – SEM images of the "Stripes" design Si masters. Representative SEM images from 2 different Si master. B and D are close-up from A and C, respectively. Micropillars on A/B are 4 and 9  $\mu$ m tall, and on C/D 6 and 15  $\mu$ m tall. Scale bars: A,C=20  $\mu$ m, B,D=5  $\mu$ m.

# EVALUATION OF MICROPILLAR TEXTURES IN VITRO

This chapter exposes the study of peripheral sensory neurons and other cells relevant for neural regeneration on micropillar surfaces. The mechanical interactions between pillars and cells, as well as the effect of topography are demonstrated.

# Contents

3.1	Introduction
3.2	Materials and Methods
3.3	Results - Primary DRG cells
3.4	Results - Macrophages
3.5	Results - Adipose-derived stem cells
3.6	Discussion
3.7	Conclusion

# Introduction

The overall objective of the present work is to study the influence of mechanical and topographic cues on the biological response to implanted neural devices. A more specific aim is to alter, and possibly control the behavior of cells through modulation of the local mechanical micro-environment presented at the surface of a silicone implant. Consistent with these goals, in vitro experiments were conducted to elucidate the interactions between surfaces patterned with micropillars and cells implicated in peripheral nerve regeneration. Adult sensory neurons and glial cells derived from dorsal root ganglia (DRG) were cultured on micropillar arrays with variations of pillar diameter and spacing. They were probed for parameters such as relative cell density, 3D integration in the micropillar matrix, soma morphology or alignment to the micropillar array. Preliminary study were conducted on 2 additional cell types: Macrophages, which have a pivotal role in the host response to foreign material, and undifferentiated adipose-derived stem cells, which can be differentiated into Schwann cell to enhance nerve regeneration [70]. Both of these cell types reacted to the micropillar topography in terms of cell density and morphology. However, they showed distinct mechanisms of interaction with the pillars

Interactions of cells with their environment have been largely investigated in terms of biochemical signalling mechanisms for the past decades. Although recognized and highly investigated, the importance and the role of physical stimuli, especially mechanical and geometrical cues, at the single cell level as well as on the tissue level, is still far from being entirely defined. In order to comprehend cellular response to micropillar cues, the integration of environmental biophysical properties by the cells are reviewed in the following sections.

#### 3.1.1 Cell sensitivity to substrate stiffness

Cells integrate and react constantly to a variety of mechanical cues in their environment, forces like tensile stress or material properties like stiffness. This mechanosensing capacity is enabled by the generation of contractile forces by the cell which literally pulls on the

substrate to probe its rigidity [71]. These contractile forces are generated by the cytoskeleton thanks to myosin motors which cross-link the actin filaments. The resulting cytoskeletal tension is applied to the extracellular matrix (ECM) through focal adhesions. The latter are dynamic structures which mature and bind intracellularly to the actin cytoskeleton of the cell, creating a direct molecular link between ECM and cell. Transmembrane receptors like integrins bind to ECM components such as fibronectin or laminin, providing mechanical adhesion between the matrix and the cell.

The traction force generated by a single focal adhesion on the ECM can reach up to 100 nN, according to values reported by Ghibaudo et al. for a MDCK epithelial cell [59]. The cell eventually stabilizes its internal tension so as to match the spring constant of the substrate, giving rise to its rigidity sensing ability [72]. Continuous remodeling of the cytoskeleton occur by polymerization and depolymerization of the actin filaments, allowing the cell to dynamically respond to mechanical cues by changing its shape, orientation and contractile state [73]. The contractile state of the cell is influenced by the elastic modulus of the substrate, but also by the distribution of ECM anchorage points, which in turn influence the morphology of the cell. The complex interplay between these parameters still needs to be fully elucidated [74].

The mechanical cues sensed by a cell can trigger various phenotypic and functional responses. Adaptation to mechanical properties by cytoskeletal remodeling can lead to cell migration along gradients of rigidity (durotaxis). Mechanical stimuli are also translated into biochemical signals through many different molecular pathways, which include mechanosensitive ion channels, exposure of cryptic peptide sequences or force-regulated protein function [75]. The Rho family of GTPases are well known mechanoresponsive molecular switches which can regulate gene expression to induce specific cellular programs [73]. These mechanotransduction events can impact critical aspects of cell behavior such as morphology, migration, proliferation, differentiation or apoptosis (Fig.3.1).

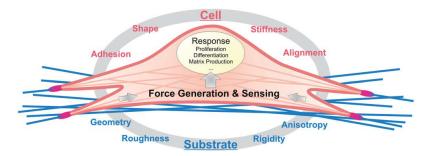


Figure 3.1 – Cells sense and respond to biophysical parameters of their microenvironment. Depiction of the interplay between substrate properties and cell response. Cell sense the substrate by contracting and remodeling their cytoskeleton. Mechanical signals can induce cellular biological programs such as proliferation, differentiation or ECM deposition. (From Kollmansberger et al. 2011 [73]).

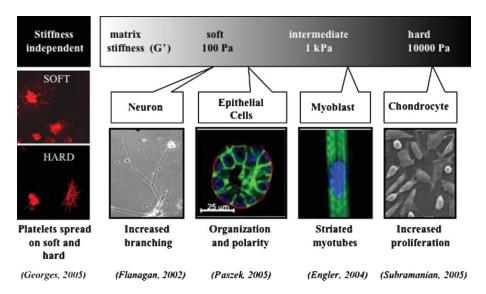


Figure 3.2 – Cell-type dependant reaction to substrate stiffness. Cells are seeded on polyacrylamide gels with varying moduli. Neurons and epithelial cells thrive on very soft matrices. Myoblasts exhibit actomyosin striation only on moderate compliance substrate. Chondrocytes grow and proliferate more on gels with modulus comparable to cartilage. (From Levental et al.(2006) [76]).

Importantly, cellular response to mechanical cues is highly cell type-dependant. An expending list of cell types were found to be mechanosensitive. The nature and magnitude of the response is specific to the cell and is most likely in correlation with the tissue they are derived from (Fig.3.2). For example, chondrocytes will proliferate more on hydrogels with elastic modulus above 10 kPa, whereas neurons survive better and send longer neurites on a soft matrices with modulus lower than 1 kPa. These values echo the natural stiffness of cartilage and brain [76]. The length of DRG neurites was shown to be directly related to the elastic modulus of agarose gels from 700 Pa to 100 Pa, demonstrating particular mechanosensitivity in this range of stiffness [22]. Glial cells from the CNS demonstrated inflammatory reaction to stiff (30 kPa) but not soft (100 Pa) substrates [77]. Research on the influence of the matrix on stem cell fate suggested a profound effect of the compliance on differentiation towards a particular cell type. Engler et al. (2006) demonstrated that mesenchymal stem cells will preferably differentiate into neuronal cells on a soft substrate (0.1-1 kPa), while moderate stiffness (8-17 kPa) promoted muscle cell types, and most rigid matrices (25-40 kPa) favored osteogenic differentiation [78]. This mechanism of mechanosensitive differentiation is thought to play a central role in the organization and formation of biological tissues during development [71].

#### 3.1.2 Neuronal mechanosensitivity

Owing to their exploratory nature, neurons are particularly sensitive to mechanical and textural cues. At the tip of axons, growth cones explore and integrate properties of their

environment in order to direct the growth of neurites. Unlike most cell types, neurons thrive on soft substrates, establishing densely branched network of neurites, and elongating longer processes [23]. The positive influence of a matrix with low stiffness was demonstrated in vitro on cortical neurons in the central nervous system (CNS), as well as on dorsal root ganglion neurons (DRG) of the peripheral nervous system (PNS) [64, 79, 22].

This particular mechanosensitivity reflects the special nature of neural tissues, which are among the softest in our organism. Elastic moduli reported in literature range between 0.2 to 1 kPa for the brain [80, 24], and 0.45 MPa for the peripheral nerves [81]. The poor regeneration of CNS neurons upon injury can find an explanation in terms of mechanical variables. Dense scar tissue is deposited as a normal wound healing process, stiffening the ECM at the site of injury. Neurons are unable to cross this mechanical barrier, unlike activated glial cells which invade scar tissue. This differential stiffness preference is targeted by repair strategies which use soft materials like hydrogels. The objective is to create an environment which is permissive for neural cells, allowing growth and extension, and non-permissive for glial cells which are unable to migrate in soft matrices [82].

## 3.1.3 Cell sensitivity to substrate topography

Topography constitutes another attribute of the extracellular environment which can influence cell behavior in numerous processes. Sub-cellular pattern down to the nanometer scale can be recognized by cells, although the precise mechanisms of recognition and response remain at the level of hypotheses. Current ideas propose that the nanoscale topography might affect the way proteins are adsorbed on the surface, thereby modifying their structure, stability and activity [83]. By extension, the biochemical configuration presented to the cell at the surface is altered, which possibly impacts its adhesion properties, morphology and behavior. This is particularly relevant for implanted materials, where surfaces are first covered by a layer of protein which is known as a pivotal mediator of the biological response to foreign body [84]. Response to topography is also thought to result in a reorganization of the cytoskeleton and re-orientation of the cell. It has been suggested that cells accommodate to the most energetically favorable cytoskeletal conformation, which produces minimal distortion of the filaments [85]. For instance, cells placed on micro-grooved surface will align parallel to the grooves, along with their actin stress fibers and microtubules.

## 3.1.4 Guidance of neurons by topography

As for stiffness, cells react differently to topography depending on their types. Contact guidance exerted by the substratum and by glial cells has been recognized as a pathfinding mechanism for growing neurites for decades [86, 87, 88]. Establishment of dendritic and axonal connections with synaptic target tens of centimeters apart implies robust pathfinding mechanisms. This process requires the ability to navigate in a well directed manner through the extracellular environment. Growth cones are highly dynamic probing structures at the tip of growing axons which explore the environment and react by advancing, turning or branching to guide axonal growth. This axonal pathfinding activity is central for the wiring of neural networks in the developing brain, as well as for re-establishing the connections of neurons upon injury [89]. Guiding of regenerating axon is a complex process where Schwann cells are thought to play a major role by providing not only biochemical signals but physical cues as well [83]. Indeed the bands of Büngner constitute a scaffold, which suggests such kind of structural orientation mechanism. Growth cones are guided through various mechanisms, including haptotaxis (ligand density gradient), chemotaxis and mechanical guidance [90]. Another essential mechanism is found with contact guidance, by which the growth cone identifies topographical cues and reacts accordingly. The detection range can go from nano- to micro-scale, and geometrical parameters such as dimensions and spacing of cues influence the pathfinding behavior. Response to a large panel of features was investigated in vitro and in vivo. This goes from anisotropic topographies like grooved surfaces, aligned fibers (Fig.3.3(A)) and cell profile replicates, to isotropic cues like pillars or nanorough surfaces. Directional control of axonal growth by contact guidance is currently envisioned for enhancing nerve regeneration. Highly oriented microstructures, such as grooves and aligned nanofibers, promoted axonal regeneration and directed Schwann cell motility and neurite orientation [91, 92, 93]. Future developments in the field of biomaterials will integrate these biophysical parameters for optimizing the functional outcome of regenerative implants.

Pillars constitute an interesting case of contact guidance which triggers particular cell behaviors. Surfaces covered with well arranged arrays of micron-size pillars were shown to induce alignment of neuronal processes to pillar geometry [94]. Astroglial cells were demonstrated to preferentially grow on a silicon substrate comprising pillar topography than on a flat surface (Fig.3.3(C))[95]. Although guidance cues are disjoint, as opposed to continuous fibers, a very high degree of fidelity to array orientation can be reached. Varying the diameter and spacing of the posts will modulate this fidelity as demonstrated by Dowell-Mesfin et al.(2004) [94]. Highest alignment is produced by larger pillars with the smallest spacing, inducing  $0^{\circ}$  and  $90^{\circ}$  orientation (Fig.3.3(B)). When the spacing is

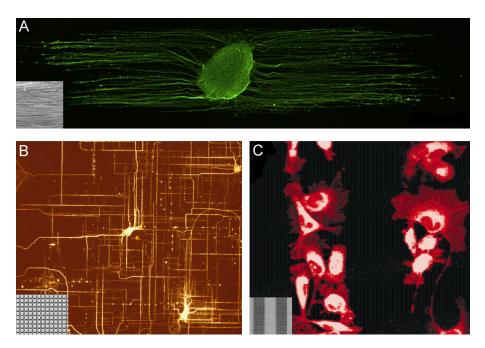


Figure 3.3 – Effect of surface topography on neuronal and glial cells. Insets show SEM images of corresponding substrates.(A) DRG neurites orientation is governed by aligned poly-L-lactic acid fibers (Adapted from Hurtado et al.(2011) [91]).(B) Hippocampal neurons showing directed orthogonal growth on silicon pillar arrays substrate (Adapted from Dowell-Mesfin et al.(2000) [94]).(C) Astroglial cells prefer micropillar substrate over flat surface (Adapted from Turner et al.(2000) [95]).

enlarged, the fidelity decreases, leading to a more random outgrowth. This phenomenon may illustrate the mechanism of axonal pathfinding. The growth cone seeks for the closest permissive cue and responds by structural consolidation before looking for the next one. A functional effect of pillar interfaces on neurons was noticed. Extension of neurites is superior on patterned substrate compared to flat surface and formation of a single axonal process is observed very early [94]. Taken together, these observations suggest that guidance by pillar structures might be efficient for directing neuronal growth in therapeutic applications.

## 3.1.5 Micropillars as soft, topographically rich environment

The approach proposed in this thesis for modulating the neural tissue-biomaterial interface relies on arrays of flexible elastomeric micropillars. Growing cells on a surface covered with micropillars provides a combination of mechanical and topographical cues, which can be easily tailored by geometrical parameters. As described in the previous chapter, micropillars act as springs that bend according to their aspect ratio and the bulk elastic properties of the material when subjected to a force. The effective compliance of the surface is thus artificially reduced. This modality has been used previously to lower the stiffness of the substrate of cells in vitro [29]. Importantly, the geometrical control of topographic and mechanical cues from micropillars is independent from the surface properties and ECM

ligands, as the chemistry of the material is not altered [25, 30].

Micropillar arrays constitute a versatile tool for studying cell-matrix interactions and mechanobiology, by probing cellular behavior in tightly controlled mechanical and chemical contexts. Previous studies notably investigated mechanisms related to stem cell differentiation, cell motility and mechanosensing [65, 96, 59]. Modulation of substrate rigidity thanks to micropillars was shown to influence human mesenchymal stem cells differentiation [25]. Another central feature of micropillars is the possibility to measure cell forces. Each pillar acts as an independent micro-sensor which can capture contractile forces by measuring the deflection of the top surface of the pillar. This modality of the micropillars can be used to unravel biomechanical aspect of cellular adhesion, response to stiffness, and possibly neural process navigation. More recently, micropillars have been considered for tissue engineering approaches, where the control of the cellular response at the interface of medical implants is critical [97, 98].

A central hypothesis of this thesis is that surfaces patterned with arrays of flexible micropillars combining mechanical compliance with topographical cues will provide a stimulating environment for regenerating neurons and accompanying glial cells. Surfaces with various micropillar geometries and densities were used to assess effects of compliance and topography on peripheral neuronal cells. In particular, the influence of interpillar spacing, with Chip 1, and pillar diameter, with Chip 9, was examined. Pillars with high aspect ratios (more than 8:1 for the highest ratio) were targeted in order to produce interfaces with stiffness relevant for neural tissue.

Glial cell densities, neurite orientation and neuronal soma morphology are factors that were modulated by the mechanical and textural cues of the silicone micropillars. Contrasting effects were discovered between neurons and glial cells in terms of surface preferences after 7 days of in vitro culture. The spatial arrangement of micropillars affected neurites navigation and network establishment. Interestingly, neurites were found mostly near the top part of pillar shafts. Consistent with previous studies, pillar spacing-dependent neurite alignment on the arrays was observed as well. Finally, a dramatic increase of macrophage and stem cell adhesion was found on the micropillars versus flat PDMS surfaces. Taken together, these results provide meaningful information on the interaction of multiple cell types with micropillars, with possible use for the design of future bio-integrated nerve implants.

## Materials and Methods

### 3.2.1 Preparation of substrates

The micropillar substrates used for the in vitro experiments described in this chapter were fabricated with the protocol described under section 2.2. The preparation of substrates for cell culture included a sterilization step for 10 minutes in 70 % ethanol. Following this, the substrates were coated by incubation in  $100 \,\mu \mathrm{g} \,\mathrm{ml}^{-1}$  poly-D-lysine overnight at 4 °C, and then in  $20 \,\mu \mathrm{g} \,\mathrm{ml}^{-1}$  laminin (LN) in PBS for 3-4 hours at 37 °C. Thorough washing with sterile PBS (3 times for 5 minutes at least) ensured removal of unattached PDL in solution. An additional incubation with a lipophilic dye (DiI) was performed when pillars needed to be imaged with fluorescence. The substrates were immersed in a sterile solution of DiI ( $10 \,\mu \mathrm{g} \,\mathrm{ml}^{-1}$ ) for 1 h at RT, protected from light. Thorough washing was again needed to remove the dye from solution. At least 20 min before seeding cells, the substrates were equilibrated in cell culture media, which differed across cell types.

## 3.2.2 Harvesting and dissociation of dorsal root ganglia

All the procedures involving animals were conducted in accordance with animal experimentation licence established by local institutional veterinary authorities (Canton de Vaud). The primary sensory neurons probed in this study were obtained from the dorsal root ganglia of adult Sprague-Dawley rats (11-15 weeks old females, 250-300 g). The rats were euthanized by  $\rm CO_2$  suffocation in a gas chamber and their vertebral columns were extracted under a ventilated hood. An opening in the vertebrae bones was cut to expose the spinal cord and locate the DRGs from the interior of the spinal canal. DRGs were excised and trimmed from nerve tissues using a stereo microscope in a ventilated hood. Once cut, the DRGs were kept in Hank's balanced salt solution (HBSS, Life Technologies) on ice. DRGs were harvested from all regions of the spinal cord, with a total varying between 20 to 30 DRGs collected per animal.

The DRGs were then enzymatically digested in 0.83% weight/volume (w/v) collagenase IX

(Sigma) diluted in a 1:2 mix of Dulbecco's Modified Eagle's Medium (DMEM) and HBSS. The total incubation time was 3 hours at 37 °C, 5 % CO<sub>2</sub>. DRG tissues were transferred to 1 ml of DMEM and mechanically triturated by pipetting up and down several times with decreasing diameter of tips, until an homogenous cloudy suspension was obtained. The solution was centrifuged at 800g for 3 min and resuspended in 1 ml of DMEM. In order to purify cells from myelin and tissue debris, the dissociated cells solution was centrifuged for  $15 \,\mathrm{min}$  at  $200 \,q$  through  $2 \,\mathrm{ml}$  of a  $15 \,\%$  w/v bovine serum albumin (BSA) solution in DMEM. Care was taken to pour the cell solution very delicately over the BSA, in order to form a distinct layer on top. After the centrifugation, most of the debris were found in the supernatant, whereas the cells were pelleted at the bottom of the tube. The supernatant was removed very gently to avoid disturbing the pellet, which was subsequently resuspended in 1 ml DMEM. An additional centrifugation was performed for 2 min at 800g to further remove the BSA solution. Finally, the cells were resuspended in 1 ml of prewarmed cell culture medium consisting of DMEM mixed with F12 (1:1), supplemented with 1% Glutamax, 10% fetal bovine serum (FBS), 1% penicillin-streptomycin (all from Life Technologies), and 100 ng ml<sup>-1</sup> nerve growth factor (NGF, Sigma).

## 3.2.3 Seeding and culture of DRG cells

Trypan blue was used to detect and count viable cells in the dissociated cell suspension. A mix of  $15\,\mu$ l of cell suspension and  $15\,\mu$ l of trypan blue was loaded in the 2 chambers of haemocytometer. The exact number of cells recovered after the harvesting protocol is difficult to assess with precision, due to the small number and high variability of cells in each quadrant of the haemocytometer. However, the typical yield was estimated to be between 60 000 to 80 000 cells per animal (20-30 harvested DRGs). In a similar way, the total number of cells seeded on the substrates was subjected to variations, imputable to multiple factors such as initial number of DRGs, procedure time, dissociation efficiency, etc. A range of approximately 3000 to 6000 cells per substrate was targeted in most experiments. The cells were seeded on samples which were equilibrated in culture medium beforehand, and which had a  $100\,\mu$ l droplet of medium remaining on the seeding area. After overnight incubation, an additional  $2.5\,\mathrm{ml}$  of cell culture medium was added on each sample. The culture media was exchanged every 2-3 days. Cells were placed in a biological incubator at  $37\,^{\circ}\mathrm{C}$ ,  $5\,^{\circ}\mathrm{CO}_2$  and  $100\,^{\circ}\mathrm{ml}$  humidity.

Table 3.1 - List of antibodies and stains used for in vitro experiments.

Compound	Dilution	Target	Manufacturer
Primary Antibodies			
Beta-III Tubulin (Tuj-1)	1:200	Neurons/neurites	Abcam(78078)
S-100	1:200	Schwann cells	Sigma(s2644)
Vinculin	1:250	Focal adhesions	Sigma (V9131)
Ki67	1:200	Proliferating cells	Abcam(ab15580)
Secondary Antibodies			
Mouse IgG-Dylight 488	1:100	Tuj-1/vinculin	Abcam(ab96879)
Rabbit IgG-Alexa 568	1:200	S100/Ki67	Life Technologies (A11036)
Rabbit IgG-Atto 647N	1:50	S100	Sigma(40839)
Mouse IgG-Atto 647N	1:100	Tuj-1	Sigma(50185)
Stains			
Phalloidin-Alexa 488	$6.6\mu\mathrm{M}$	F-actin	Life Technologies (A12379)
DiI	$5 \mathrm{\mu g}\mathrm{ml}^{-1}$	Pillar visualization	Life Technologies (V22885)
DAPI	$10\mathrm{\mu gml^{-1}}$	All cell nulcei	Sigma(D9542)

### 3.2.4 Immunofluorescence staining and imaging

The procedure described here is valid for all assays employing immunofluorescence detection with antibodies and stains, unless otherwise stated. Samples were fixed with 10% neutral buffered formalin (Sigma) for 20 min at room temperature (RT) then rinsed 3 times with PBS. Non-specific staining was prevented by incubating the samples for 1 h in blocking buffer consisting of 4% normal goat serum, 1% BSA, 0.1% Triton-X (all from Sigma). Primary antibodies were diluted in the blocking buffer and incubated on the samples overnight at 4°C. After rinsing 3 times for 5 minutes with PBS, secondary antibodies diluted in blocking buffer were incubated on the samples for 1 h at RT in the dark. All secondray antibodies were raised in goat. The list of stains, primary antibodies and secondary antibodies used throughout the chapter can be found on Table 3.1. Cell nuclei were counterstained with  $10 \,\mu \mathrm{g} \,\mathrm{ml}^{-1}$  4,6-diamidino-2-phenylindole dihydrochloride (DAPI, Invitrogen). Coverslips were mounted on glass slides with ProLong Gold antifade reagent (Life Technologies) and stored at 4 °C. Imaging of the samples was performed either with an epifluorescence microscope (Leica DM6000) or with a confocal microscope (Zeiss LSM700 or Leica SP5 WLL). Objectives and relevant parameters are indicated on figures for each assay.

#### 3.2.5 Scanning electron microscopy

The samples destined for electronic microscopy imaging were fixed at 8 days in vitro (DIV) with  $1.25\,\%$  glutaraldehyde in PBS for  $15\,\mathrm{min}$  at RT. After rinsing 3 times with PBS and once with  $0.1\,\mathrm{M}$  cacodylate buffer, the samples were postfixed in  $1\,\%$  OsO<sub>4</sub> (osmium tetroxide) in  $0.1\,\mathrm{M}$  cacodylate buffer for 1 h. Samples were then dehydrated by incubation in graded ethanol:water mixtures ( $0\,\%$ ,  $25\,\%$ ,  $50\,\%$ ,  $75\,\%$ ,  $100\,\%$  twice) in deionized (DI) water for 5 min at each grade. Samples in pure ethanol were dried with a critical point drier (Leica EM CPD300) in order to avoid collapsing of fine structures. Finally, the samples were sputtered with a gold-palladium layer and imaged with a Phillips XL 30-FEG SEM.

## 3.2.6 Quantification of cell densities

Distribution of neurons and glial cells were quantified on cultures fixed after 7 days in vitro (DIV). Tuj-1-positive neurons and DAPI-positive nuclei were counted from field of views (FOV) representing a 0.6 mm<sup>2</sup> surface area (acquired with a 10x objective). A total of 6 to 9 FOVs were acquired for each sample. A total of 8 to 9 independent samples, from 3 to 4 animals, were averaged per condition (n=8-9). For a given sample, the fraction of cells on a surface type was obtained by summing the counted cells on the surface type, and dividing by the total number of counted cells for all conditions. This represents the relative percentage of cells on each surface type. An equal distribution of cells on all surfaces amounts to 0.2 for Chip 9, and to 0.25 for Chip 1. Dotted lines indicate these thresholds on the corresponding graphs. The same protocol was used to determine the distribution of neurons on the different substrates.

#### 3.2.7 Proliferation and viability assays

Proliferation of glial cells was assayed at 7 DIV on surfaces from Chip 1 and 9. The marker Ki-67, present in the active phases of the cell cycle, was used to assess the fraction of cells in growth phase. Ki-67 is mainly present in the nuclei of cells. The ratio between Ki-67-positive nuclei and total nuclei (DAPI-stained) on FOVs (from 10x objective) gave the percentage of proliferative cells. Protocol for the culture, fixation and immuno-staining were as described in the previous sections.

The viability of the cells was assessed with a live/dead assay (Invitrogen) on cultures after 4 DIV. It relies on 2 dyes: Calcein AM, which is retained in live cells and produces green fluorescence, and Ethidium homodimer (EthD-1) which produces red fluorescence in contact of nucleic acids from cells with damaged membranes. The cell cultures were washed

with PBS and incubated in fresh media containing  $2\,\mu\text{M}$  Calcein AM (staining live cells) and  $4\,\mu\text{M}$  EthD-1 for  $30\,\text{min}$  at  $37\,^{\circ}\text{C}$ . After incubation, the cultures were washed with PBS and new fresh media without additives was added. The samples were then immediately imaged under a fluorescence microscope with green and red filters, for Calcein AM and EthD-1 respectively. The viability of cells was expressed as percentage of dead cell, which was given by the ratio of EthD-1-stained cells to total cells per FOV.

## 3.2.8 Quantification of neurite and glial cell orientation

Neurites FOVs of 400x400 pixels (ca. 255x255 µm) were selected from epifluorescence images acquired with a 10x objective. The images were rotated beforehand to present the Sx and Sy pillar matrix directions aligned at 0° and 90° respectively. Skeletonized representations of the neurite networks were obtained with the plugin "NeurphologyJ" for imageJ (NIH) [23]. Neurite orientation was defined as the angle between the branches of the skeleton and the vertical axis of the image. The datasets were filtered to retain only branches longer than 15 pixels (ca. 10 µm) and with a ratio Euclidian distance to branch length larger than 0.85. This ensured removal of most artifacts, keeping only straight neurite segment longer than 10 µm. The relative frequencies of each angle were calculated, averaged across FOVs, and plotted as circular histograms with OriginPro. At least 20 FOVs were acquired for each of the 5 samples across 3 experiments. Alignment with the pillar grid was quantified by comparing values at 0° and 90°, corresponding to Sx and Sy, between pillar surfaces and flat control areas.

Glial cells The orientation of glial cells was assessed from the angle of the major elliptic axis of their nuclei. This method is particularly suited for detecting the orientation of Schwann cells, which constitute most of the non-neuronal cells. Schwann cells most commonly display elongated bipolar morphology with thin cytoplasmic processes. Their nuclei are recognizable by their small, dense, elongated form, which aligns to the tightly wrapped cytoplasm. Therefore the angle of longest axis of the nucleus effectively describe the orientation of the Schwann cell. ImageJ was used to compute this angle. Fluorescence microscopy images of DAPI-stained nuclei were thresholded in order to segment the nuclei from the background. An ellipse was then fitted to describe the shape of each nucleus and the angle of the major axis was calculated by the "analysis particle" plugin of imageJ. Angles were analysed and compared to pillar grid and neurite orientations.

#### 3.2.9 Quantification of soma morphology

The somas of neurons were delimited on cell images stained for Tuj-1 with to a threshold-based segmentation method. The projected surface area and circularity of somas were measured with the "analysis particles" plugin of ImageJ. Circularity is derived from the following formula:  $C = 4\pi A/P^2$ , where A is the projected area of the soma and P its perimeter. The distributions of soma areas and circularities were reported as cumulative and relative frequencies, in bins of  $200\,\mu\text{m}^2$  and 0.05 intervals respectively. Significant differences between cumulative distributions were reported on tables inside the plot areas. The mean values for each dataset was plotted on bar graphs, with indicated significant difference .

#### 3.2.10 Traction forces analysis

The traction forces exerted by DRG neurons on micropillars were evaluated after 4 hours on substrates with variations of diameter (Chip 9). The samples were fixed and stained as previously described (sec.3.2.4). Confocal microscopy was used to obtain images of pillar cross-sections. The pinhole of the microscope was set to 1 airy unit in order to obtain the best possible resolution in the z-axis. One image was acquired at the level of pillar tops and one image at a level just above the bottom surface. The deflection of pillars was measured by calculating the difference of position between top and bottom cross-sections of pillars. ImageJ was used for the image analysis. Fluorescence images were thresholded to binary images presenting white spots for the pillar sections. The TrackMate plugin of imageJ was used to compute the pillars displacement in the x-y plane. The background "noise" displacement of pillars was estimated on pillars which were not in contact with cells, and subtracted from the cell-generated displacements. The forces were computed by multiplying the displacement with the pillar spring constant k, obtained from FEM simulations (cf. Chapter 2). A critical point in this protocol was to select DRG neurons which were not in contact with other cells. Tuj-1 staining was used to locate cells and compute the spread area of somas on pillars. DAPI staining was used to detect non-neuronal cells that might interfere with neurons.

### 3.2.11 Immortalized bone macrophages culture and assays

A frozen stock vial of immortalized bone marrow macrophages (IBMM) was kindly offered by Dr. de Tita (Laboratory of Lymphatic and Cancer Bioengineering, EPFL). The cells were plated in 100 mm diameter petri dishes, grown near confluence and sub-cultured. The

culture medium for these cells consisted in IMDM (Iscove's Modified Dulbecco's Medium) supplemented with 20 % FBS, 1 % penicillin/streptomycin and 50 ng ml<sup>-1</sup> macrophage colony-stimulating factor (m-csf). The cells were passaged three times before plating on micropillar substrates. The attached cells were recovered from the plate by incubation in 5 ml of trypsin for 10 min. Once detached, the cells were centrifuged at 2000rpm for 8 min, resuspended in 1 ml of medium and counted with a haemocytometer. A total of 60 000 cells were seeded per sample, giving a plating density of 6250 cells/cm<sup>2</sup>. The cultures were stopped after 24 h by fixation with 4 % PFA and stained for actin and DAPI with the same protocol as before (sec.3.2.4).

The samples used for this experiment were replicates from Chip 1 and Chip 9 for micropillars, and glass coverslips and plastic dishes for the controls. All samples were coated with  $0.1 \text{ mg ml}^{-1}$  PDL, following the same procedure as described previously. No laminin was used to coat these samples. The cell number and cell area were measured as previously described for DRG cells.

## 3.2.12 Adipose-derived stem cells culture and assays

Adipose-derived stem cells (ASC) were harvested from visceral and inguinal fat of adult male Sprague-Dawley rats. The adipose tissue was minced in small pieces and digested in presence of 0.2% w/v collagenase type I (Sigma) for 1 hour at  $37\,^{\circ}$ C. Undissociated tissue pieces were filtered by passing the suspension through a cell strainer with  $100\,\mu\text{m}$  pores. After neutralization of the enzyme with growth medium containing fetal bovine serum (FBS), the solution was centrifuged at  $300\,\text{g}$  for  $5\,\text{min}$  in order to pellet the stromal vascular fraction at the bottom of the tube. The pellet was then resuspended in  $1\,\text{ml}$  of red blood cell lysis buffer to remove blood cell contamination. After  $1\,\text{min}$  of pipetting, the tube was filled with  $10\,\text{ml}$  of stem cell growth medium and centrifuged at  $300\,\text{g}$  for  $5\,\text{min}$ . After discarding the supernatant, the pellet was resuspended in  $10\,\text{ml}$  of stem cell growth medium and transferred to  $75\,\text{cm}^2$  culture flasks. Cell were incubated at  $37\,^{\circ}\text{C}$ ,  $5\,^{\circ}\text{CO}_2$  and maintained at sub-confluent level, changing medium every  $3\,\text{days}$ . The stem cell growth medium was composed of Minimum Essential Medium ( $\alpha$ -MEM, Invitrogen) supplemented with  $1\,^{\circ}\text{m}$  penicillin/streptomycin,  $10\,^{\circ}\text{m}$  FBS and  $200\,\text{mm}$  L-glutamine.

The glass and PDMS substrates were coated with  $0.1 \,\mathrm{mg} \,\mathrm{ml}^{-1}$  PDL following the same protocol described earlier. Stem cells were plated at a plating density of  $10\,000 \,\mathrm{cells/cm^2}$  and incubated for 3 days before fixing with PFA and staining. The samples were stained for actin, vinculin and DAPI following the protocol previously reported. The expression of the stem cell markers Nestin and Stro-1 were assessed through immunocytochemistry on

cells plated on glass coverslips.

## 3.2.13 Statistical analysis

The general statistical methods used for analysing the different assays are described here. Statistical tests were conducted with the software OriginPro (OriginLab corp.). Homogeneity of variance between groups was determined with Levene's test. In case of equal variances, one-way analysis of variance (ANOVA) with Tukey's post-hoc test was chosen for multiple comparisons of means. In case of unequal variances, Kruskal–Wallis ANOVA rank test for non-normal distribution was performed to assess if significant differences exist between groups. The Mann–Whitney U test adjusted with the Bonferroni method was used for comparison between group means. The two-sample Kolmogorov-Smirnov test adjusted with Bonferroni method was used to establish significance between cumulative distributions. The level of significance, if not indicated on the graph, was set at P < 0.05.

## Results - Primary DRG cells

#### 3.3.1 Micropillar substrates for in vitro experiments

In order to investigate the effect of micropillar geometry on the different types of cell, Chips 1 and 9, from the library of designs (Chapter 2), were used for in vitro experiments. Dimensions and characteristics of the different micropillar configurations are reported in Table D from Fig.3.4.

Chip 1 was designed to present variations of micropillar densities, while keeping a minimal stiffness (Fig.3.4C). The relative surface area SA/PA quantifies the increase of surface area due to micropillars, compared to an un-patterned area of equal size. The configurations S1, S3 and S7 resulted in SA/PA of 7.7, 2.8 and 1.5, respectively. Cells on dense configurations were therefore presented with increased potential attachment sites, as laminin covered ubiquitously the PDMS surface.

Chip 9 was designed to offer 4 different surface stiffnesses, while keeping constant surface area (Fig.3.4C). The effective moduli  $E_{eff}$  of surfaces D1, D2, D3 and D4 were 0.7kPa, 4.0kPa, 12.3kPa and 27.0kPa, respectively. This range of stiffness represents a decrease of 1 to 3 orders of magnitude compared to the modulus of bulk PDMS (1.95 MPa). The distinct mechanical behaviour of the micropillars can be observed on their force-displacement curve (Fig.3.4B). A shear load of 1 nN, commensurate with forces applied by cells, resulted in different extents of pillars tip deflections. This difference is important in force tracking experiments, where the flexibility of micropillars determines their sensitivity to a range of forces.

## 3.3.2 Culture of DRG cells on Chip 1 and Chip 9

DRG cells were grown on replicates from Chip 1 and 9, and cultures were examined after 7 days in vitro. By that time, the cells had proliferated and dense neurite networks were established on the Flat PDMS control. The samples were observed with immunofluorescence microscopy to detect specific targets such as neuron/neurites, Schwann cells, nuclei and

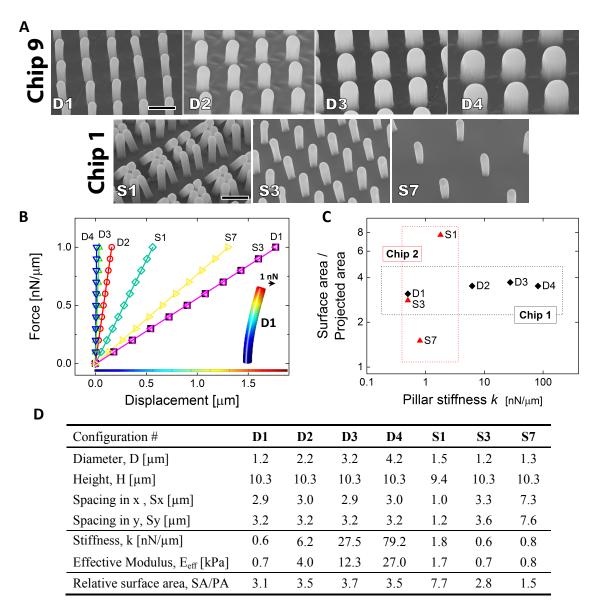


Figure 3.4 – Recapitulation of Chips 1 and 9 characteristics. (A) SEM images from PDMS micropillars on Chips 1 and 9. Scale bars =  $5 \,\mu\text{m.}(B)$  Force-displacement curves of micropillars under a 1 nN load applied to their top (FEM simulations). The deformation of a D1 micropillar is represented in the right corner of the graph. (C) Configurations are mapped according to their calculated pillar stiffness k and surface area to projected area ratio SA/PA. Black dotted rectangle encompass the configurations pertaining to Chip 1, which have varying k constants but similar SA/PA ratios. Red dotted rectangle encompass configurations from Chip 2, which have varying SA/PA ratios but similar k constants. (D) Dimensions of the different arrays, with corresponding k constants, effective moduli and relative surface areas.

pillars (Fig.3.5). DRGs contain non-neuronal cells which were seeded together with the neurons on the substrates. Most of these non-neuronal cells stained against the Schwann cell-specific marker S-100, as observed in Fig.3.6 B. The percentage of non-neuronal cells was typically lower than  $10\,\%$  in these cultures. The pool of non-neuronal cell was referred to as glial cells.

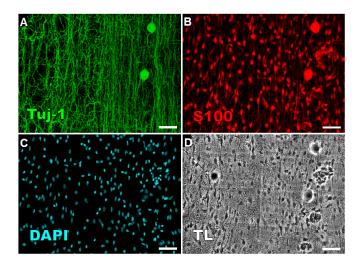


Figure 3.5 – Immunostaining of DRG cell cultures. Representative fluorescence images of DRG cultures on S1 stained after 7 DIV against Tuj-1 for neurons (A) and S-100 for Schwann cells (B), and counterstained with DAPI for cell nuclei(C). (D) Bright field image of the same FOV. Neuronal somas stained as well for S-100. The percentage of cell that did not stain for S-100 here was 5.7%. Scale bars =  $50 \, \mu m$ .

SEM imaging was used to assess the morphology of cells on the different configurations (Fig.3.7 and 3.8). The micro-topography alters the density, composition and morphology of the cultures. These aspects are quantified in the following sections, but we can observe qualitative differences on SEM and fluorescence pictures . The reduction in cell number is particularly visible on arrays with smaller pillar diameter and lower pillar densities (Fig.3.6 A and B). Alignment of neurites with pillar grid is dependent on pillar spacing, with strong alignment observable on S1 (S=1.0  $\mu$ m), gradually lost on S3 (S=3.5  $\mu$ m) and S7 (S=7.5  $\mu$ m).

The morphology of cells, as seen on SEM images, revealed differences in the shape, position and orientation of cellular processes. We observed the alignment of processes on the densest array S1, whereas S3 and S7 showed no preferential direction (Fig.3.7). The small diameter pillars on chip 9 induced thinner cellular processes, which gradually became thicker and more spread as the diameter increase from D1 to D4 (Fig.3.7A). We also observe the different flexibilities of these pillars, through cell-applied forces: pillars on D1 are considerably bend at the periphery of cells, whereas on D4 they barely experience any deformation (Fig.3.8B). The positions of cells along pillar height is dependant on the inter-pillar spacing. We observe cells mostly located on the top of pillars on S1. As pillars

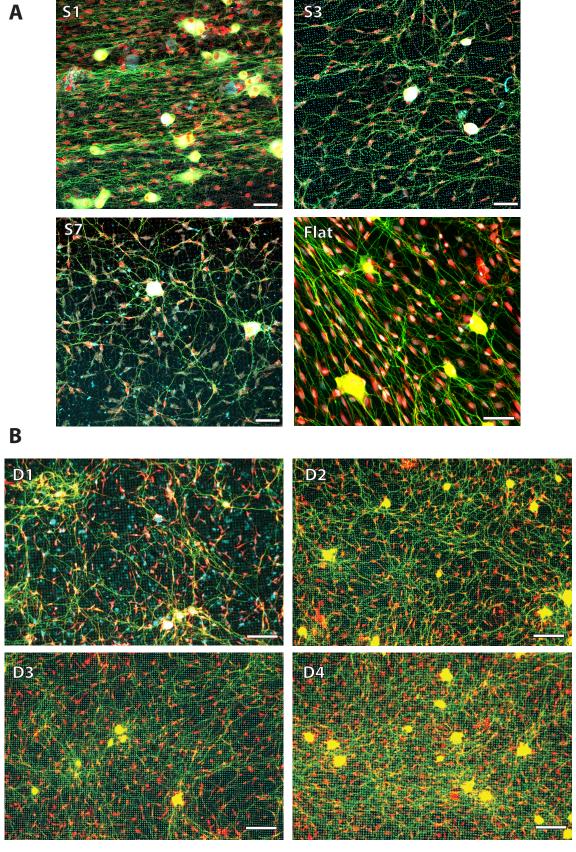


Figure 3.6 – Representative images of DRG cells on Chips 1 and 9 after 7 DIV. The samples were immuno-labelled with Tuj-1 for neurons (green), S-100 for glial cells (red) and pillars were stained with DiI (cyan). (A) Configurations on Chip 1, imaged with confocal microscopy. Scale bars =  $50\,\mu m$  (B) Configurations on Chip 9, imaged with epifluorescence microscopy. Scale bars =  $100\,\mu m$ .

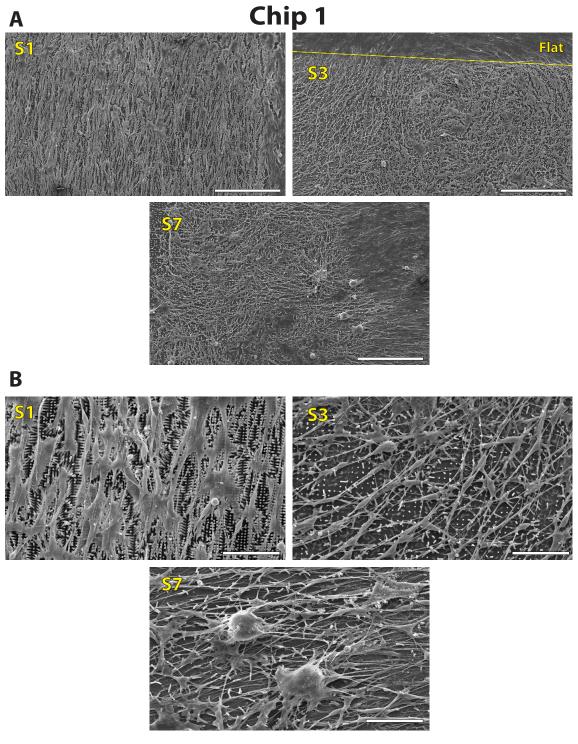


Figure 3.7 – SEM images of DRG cells on Chip 1 after 8 DIV. The configuration S1 shows the alignment of cells to the pillar matrix in the direction of the X-axis. The alignment is lost on S3 and S7.(A) 120x magnification, scale bars=200  $\mu$ m. (B) 500x magnification, scale bars=50  $\mu$ m.

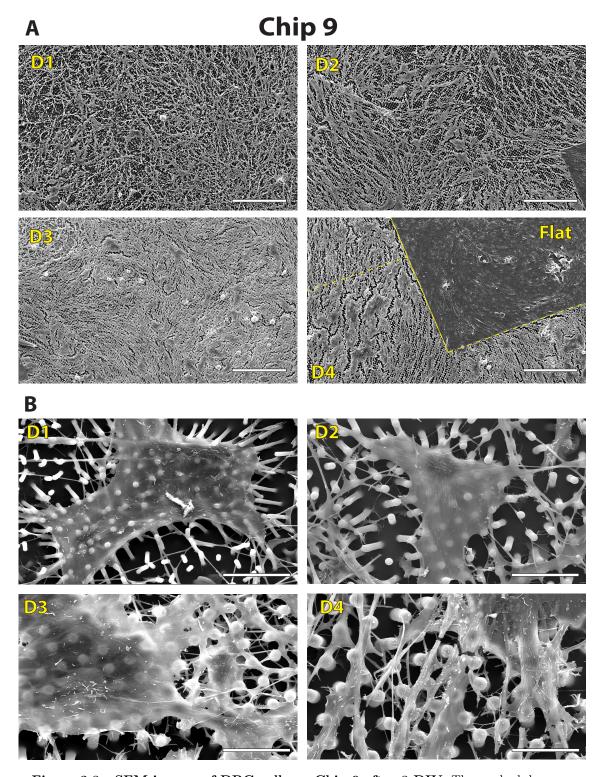


Figure 3.8 – SEM images of DRG cells on Chip 9 after 8 DIV. The gradual decrease of the flexibility of the micropillars from D1 to D4 is observable through their deformation by cells. (A) 120x magnification, scale bars= $20\,\mu m$ . (B) 1500x magnification, scale bars= $20\,\mu m$ .

spread apart, the interpillar space is increasingly invaded with cellular processes.

## 3.3.3 Integration of DRG cells on micropillars in the XZ plane

Three-dimensional information on cellular integration in the micropillar environment was acquired with confocal microscopy. To assess the position of neurites along the Z-axis, stacks of images in the X-Z plane were acquired over 30 to 80 µm distances along the Y-axis. Maximal projections of the stacks regrouped the information on neurite or soma position on a single plane (Fig.3.9). Neurites explored the entire Z-dimension of the micropillar environment, from the bottom surface to the top of pillars. Regardless of pillar spacing, the majority of neurites were found well above the bottom surface (Fig.3.9 C). The proportion of neurites near the top of pillars increased with small interpillar spacings. Similarly, most neuronal somas and glial cells were also located on top of pillars of dense arrays. Cytoplasmic protrusions invaded the interpillar space of the less dense arrays, where pillar collapsing could occur due to cellular forces (Fig.3.9 A-B). In all cases, we observed substantial deformation of the pillar arrays induced by traction forces exerted by glial cells and neurons.

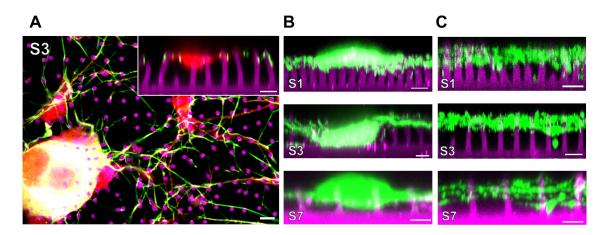


Figure 3.9 – Confocal imaging of DRG cells in the XZ plane. Stacks of images acquired by confocal microscopy. Green is for neurites/neurons, red for Schwann cells and magenta for DiI-labelled micropillars. Configurations are indicated on images. All scale bars are 5 μm. (A) XY plane image taken at the level of pillar tops, showing a neuronal soma with outgrowing neurites and neighboring glial cells. Inset: XZ plane image of a glial cell interacting with micropillars and supporting neurites. (B) Neuronal somas on S1, S3 and S7 in the XZ plane. Each image is reconstructed from the projection of a stacks of XZ images spanning 30 μm in the Y-axis direction. A single XZ image is used for micropillars (magenta) for clarity. (C) Position of neurites along the shaft of micropillars seen in the XZ plane. Again, the green signal is reconstructed from Y-projections of stacks spanning 70-80 μm in the Y-axis direction. A single image of micropillars (magenta) is superimposed.

## 3.3.4 DRG cell density

As a first step to assess the preferential topography for neuronal growth, the relative percentage of neurons as function of pillar spacing and diameter was probed with Chips 1 and 9. The relative number of glial cells on each surface was assessed in the same way.

#### Neurons

After 7 days in vitro, numerous healthy neurons with neurites were observed on each type of surface (Fig.3.10 A). The fractions of neurons on the surfaces with diameter variations (Chip 9) did not differ significantly (Fig.3.10 B). One can observe a trend indicating a decrease of neuron number with thinning micropillar diameter. D1 matrix hosted about 17.3% of the total neurons, while D4 and flat surfaces had 21.7% and 20.9% respectively. Pillar spacing (Chip 1) was not found to exert an influence on the distribution of adhering somas. S1, S3 and S7 all displayed a number of somas within error range from equal distribution (Fig.3.10 C).

#### Glial cells

After 7 DIV, the cells had proliferated and formed a dense, confluent population on the flat PDMS control. The distribution of cells was affected by the micropillar textures (both in pillar diameter and spacing). The number of cells decreased with decreasing pillar diameter (Fig.3.10 D). D1 ( $16.0 \pm 0.4\%$ ) supported significantly less cells than D3 ( $20.6 \pm 0.9\%$ ), D4 ( $22.6 \pm 0.5\%$ ) and Flat ( $23.2 \pm 0.8\%$ ) surfaces. Similarly, D2 ( $17.6 \pm 0.9\%$ ) was significantly different from the D3, D4 and Flat configurations. However, D3 and D4 matrices displayed fractions of cells comparable to the Flat control, with no significance difference. The effect of interpillar spacing on Chip 1 is illustrated Fig.3.10 E. Large gaps between pillars correlated with decreased cell populations. Both S3 ( $21.0 \pm 1.6\%$ ) and S7 ( $23.5 \pm 1.1\%$ ) surfaces supported significantly fewer cells than the Flat control ( $29.3 \pm 1.6\%$ ), and no significant difference was found between the densest pillar S1 ( $26.2 \pm 1.3\%$ ) and Flat configurations.

#### 3.3.5 Viability and proliferation

Differences in the cell proliferation capacity were assessed on the test surfaces at 7 DIV. The fraction of non-neuronal cells in active growth phase was assessed with the proliferation marker Ki-67 (Fig.3.11 A-C-E). Results show the opposite behaviour from what is seen on the graphs of cell distributions: More cells are in a proliferative state on the softest,

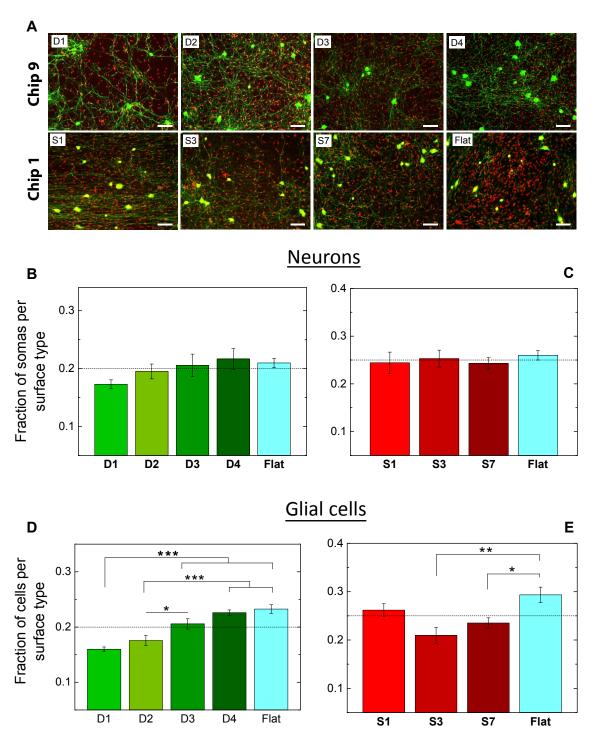


Figure 3.10 – Distribution of neurons and glial cells on Chip 1 and 9 after 7 DIV. (A) Typical FOV used for the quantification. Neuronal bodies are green and cell nuclei red. Scale bar =  $100\,\mu\text{m}$ . Graphs of the distributions of neurons (B-C) and total cells (D-E) on the different conditions presented by Chip 1 (B-D) and Chip 9 (C-E). Data are averaged from 9 samples across 4 independent experiments for (B-C) and 8 samples across 3 independent experiments for (D-E). On all graph, bar heights represent the means and error bars the standard error of mean (SEM). The dotted lines on the graphs indicate the point of equal distribution among all conditions (Chip 1=0.2 and Chip 9=0.25). Significance levels: \*P < 0.05, \*\*P < 0.01, \*\*P < 0.001.

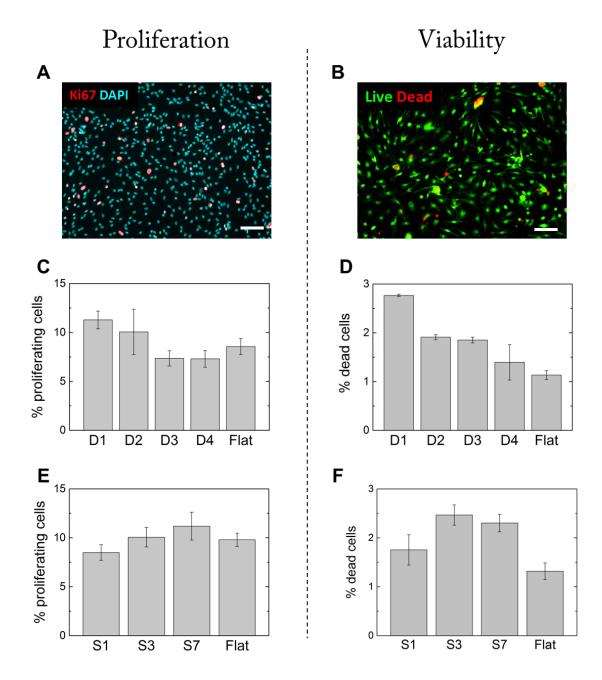


Figure 3.11 – Proliferation and viability of cells on Chip 1 and 9. (A) Fluorescence image of Ki-67 positive cells among DAPI-stained nuclei. (B) Fluorescence image of live/dead assays, showing live and dead cells in green and red, respectively. Proliferation after 7 DIV, expressed as percentage of Ki-67 positive cells, on Chip 9 (C) and Chip 1 (E). Data averaged from 24 to 45 FOVs per condition (4 independent samples). Cell viability after 4 DIV, expressed as percentage of dead cells on Chip 9 (D) and Chip 1 (F). Data averaged from 8 FOVs per condition (2 independent samples). Bar heights indicates the mean and error bars the SEM.

sparest configurations D1 ,D2, S3 and S7, compared to D3, D4, S1 and Flat. By extension, the surfaces supporting the highest densities of cells have lower percentages of proliferating cells. This counter-intuitive observation may come from the fact that the cells are almost confluent on these surfaces and thus need to avoid overgrowth. Contact inhibition may occur at this stage to regulate the number of cells and keep the cells as a monolayer. On the other hand, surfaces with fewer cells have more uncolonized space and cells are not stopped from proliferating.

The viability of cells, expressed as percentage of dead cells, was evaluated at an earlier time point (4 DIV). The results, illustrated on Fig.3.11 B-D-F, are in accordance with the distribution of cells at 7 DIV. The fraction of cellular death increases as the effective modulus of surfaces decreases. D1 showed two-fold increase in cellular death compared to flat control. On the other hand, D4 remained within the error range from the flat surface. This situation is reflected later by the smaller densities of cells present at 7 DIV on the softest surfaces. On Chip 1, cellular death was more important on configurations with larger interpillar spacing. As for cell densities at 7 DIV, S1 and Flat had comparable values, whereas S3 and S7 induced markedly higher dead cell percentage.

## 3.3.6 Neuronal somas morphology

The stiffness of the substrate is known to affect the morphology of several cell types [99]. Using Chip 1, we tested this hypothesis by quantifying the surface area and circularity of neuron somas as a function of the effective stiffness of the substrate (Fig. 3.12). We observed a non-normal distribution of the soma areas and circularities: Small and round somas (<400 µm<sup>2</sup>) were predominantly found across all surfaces. However, comparing cumulative frequencies, we found significant difference between the distributions on soft (D1, D2) versus stiff (D3, D4) surfaces (Fig. 3.12 B-C). Detailed analysis revealed that the proportion of small somas was greater on D1 (62.84%) than on D4 (40%) (Fig.3.12 D). Inversely, large somas (1000-2600 µm<sup>2</sup>) represented 16.8% of the population on D4 but only 4.6 % on D1. The mean values of some surface area further confirmed this trend, with the significant differences between D1, D2 and all the other conditions (Fig.3.12 F-G). To further characterize the morphology of neurons, we quantified their circularity with a numerical descriptor (cf. methods). Consistent with the results for soma area, the softest surfaces D1 and D2 supported rounder somas compared to D3 and D4 matrices (Fig.3.12 C-E-G). The circularity of neurons cultured on flat surfaces was not significantly different from the softest D1 and D2 configurations, but from the stiffest one (D4). However, comparison with a flat topography might be less relevant in this case. The cytoplasm was

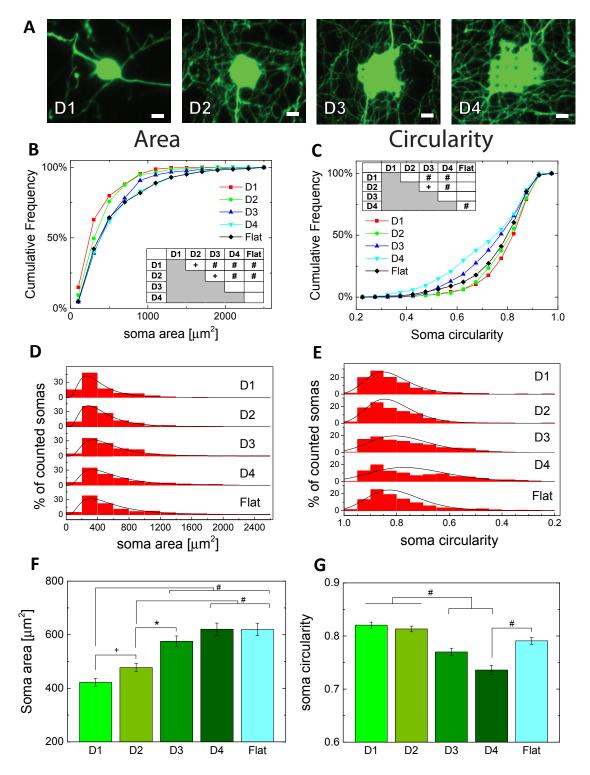


Figure 3.12 – Morphology of neuronal somas on surfaces with diameter variations from Chip 1. (A) Representative fluorescence images of individual neuronal somas used for the quantification. scale bars =  $10\,\mu\text{m}$ . The projected surface area of somas (B,D,F) and their circularity (C,E,G) were used as morphological descriptors. Graphs (B) and (C) present the cumulative frequencies, with significant differences between distributions indicated on the inside tables . The histograms (D) and (E) show the relative distributions (red bars), fitted with probability density functions (black curves) following a log-normal distribution for soma area and a Weibull distribution for soma circularities. The mean values and SEM are indicated on Graph (F) and (G), with associated significance. Data was generated from 6 independent samples across 3 experiments. The total number of somas analyzed for these measurements are: D1=323, D2=363, D3=335, D4=357, Flat=370. Significance levels: #P < 0.001; \*P < 0.01; \*P < 0.05.

occasionally deformed by micropillars at the periphery of somas, inducing artificially lower circularities compared to unperturbed planar growth.

#### 3.3.7 Neurite orientation

Square matrices of pillars provided guidance cues for the growing neurites. Using Chip 9, we monitored the orientation of growing neurites as function of pillar spacing. At 7 DIV, all configurations displayed well developed networks of neurites (Fig.3.13 A). The percentage of neurites oriented at each angle is reported in 10° intervals on circular histograms (Fig.3.13 B). The S1 configuration demonstrated a very strong alignment of neurites to the pillar pattern specifically in the 0°/ Sx direction. On this substrate, 17.8% of neurite segments were orientated between -5° to 5°, compared to only 5.2% for the control Flat condition (Fig.3.13 C). This strong effect was lost when the interpillar gap increased. S3 and S7 had relatively homogenous distribution of neurites at all angles. However, the guidance effect from sparse pillars remained to a certain extent, on shorter neurite lengths. The portion of neurite segments oriented in the Sx or Sy directions was still significantly higher than on flat surface control (Fig.3.13 C).

#### 3.3.8 Schwann cells orientation

The orientation of glial cells was assessed by the angle of the major elliptic axis of their nuclei. Schwann cells, which constitute most of the non-neuronal cells, displayed elongated bipolar morphology co-directional with their nuclei major axis on flat substrate. The morphology of Schwann cells was similar on pillars from Chip 1, with two thin elongated process. As on flat topography, Schwann cell orientation was highly correlated to neurites direction (Fig.3.14). Histograms of angular distributions of neurites and Schwann cell nuclei demonstrate very close patterns. The formation of concentrated bundles of aligned neurites, as seen on Flat and S1, is associated with high densities of Schwann cells orientated in the same direction. On S3 and S7, the alignment of neurites on pillar is gradually lost, which is the case as well for Schwann cells. Interestingly, highly dense and oriented neurite bundles are not seen on S3 and S7. Perturbation of Schwann cell growth due to unfavorable topography, corroborated by the reduced cell densities on these surfaces, might prevent the formation of such structures.

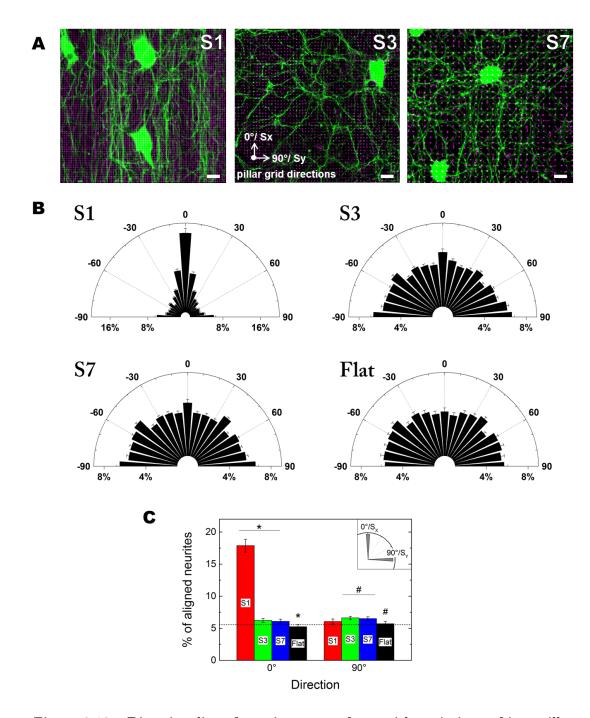


Figure 3.13 – Directionality of neurites on surfaces with variations of interpillar spacings. (A) Representative FOVs  $(255 \times 255 \, \mu\text{m}^2)$  from S1, S3, and S7 used for the quantification of neurite orientation. The 0° and 90° angles correspond respectively to the Sx and Sy directions of the pillar spacing measurements reported in Table 1. Neurons are green and pillars magenta. Images were segmented and skeletonized in order to register neurite angles. Scale bars = 20  $\mu$ m. (B) Angular distribution of neurites is depicted on circular histograms. The radial axes report the percentage of neurite orientated at a particular angle. The data was generated from 5 samples from 3 independent experiments, with at least 20 FOVs per sample. Angles were grouped in bins of 10°. Bar heights represent means and error bars are the SEM. Significance levels: \*P < 0.001; #P < 0.01.

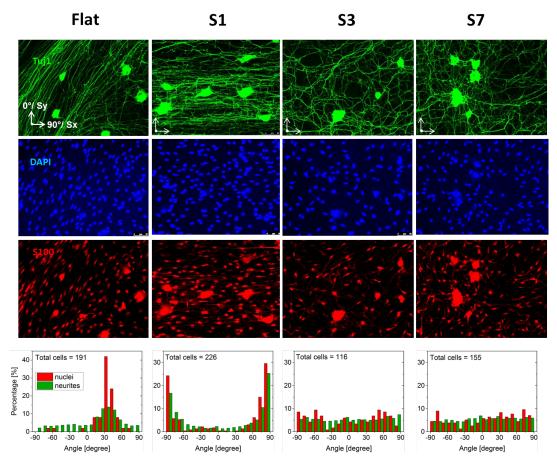


Figure 3.14 – Alignment of Schwann cells and neurites on Chip 9 topographies. Fluorescent images representing neurites/neuron (green), nuclei (blue) and Schwann cells (red) from FOVs acquired with a 20x magnification. The histograms on the bottom show the orientation of neurites and cell nuclei from the above images, grouped in bins of 10° and expressed as relative percentage. The total number of cells is reported in the top left corner. The directions of the pillar grid Sx and Sy are aligned at 90° and 0° angles, as indicated on the top left image.

#### 3.3.9 Soma traction force measurements

As mentioned earlier, micropillars provide an effective mean to measure forces applied by cells in vitro. The displacement of the pillar top surface is directly proportional to the force applied and to the pillar spring constant k. The latter is defined geometrically by the diameter and length of the pillar beam. The spring constants also determine the range of forces which can be accurately detected. Chip 9 provides variations of pillar flexibilities through different diameters. The D2 to D4 surfaces were therefore used to probe the traction forces applied by DRG neurons, as function of surface stiffness and soma spread area (Fig.3.15). A critical point for such experiment is to obtain individual cells. At 7 DIV, cells are confluent and the determination of cell forces are not possible. Therefore, early time points were used here. The DRG cells were fixed 4 hours after being seeded on the substrates. Thus, the very initial interaction of neurons with the micropillar

topographies is observed. Individual neurons were selected, taking care that no other interfering cell was present in the vicinity. At such early time points, most individual neurons did not extend neurite yet. Traction forces emanated from the soma or from very short processes sent on pillar neighboring the soma perimeter. Most of the individual somas were resting on the top of pillars, occasionally encompassing short portions of the upper part of pillars. The immunostaining revealed contrasting organisation of the cytoskeletal elements (Fig.3.15A iii and iv). Microtubules, visualized thanks to the neuron-specific tubulin antibody, showed uniform staining of the entire cytoplasm, with particularly strong staining near the surface. On the other hand, actin formed discrete bright puncta, visible throughout the cell cytoplasm. Similar actin structures were reported in the growth cones of DRGs [61]. These puncta were found everywhere in the cytoplasm, but concentrated particularly near the pillars and at the periphery of the soma (Fig.3.15A iii). Entire rings around pillars were occasionally seen. Traction stress applied by growth cones are thought to result from the coupling between actin cytoskeleton and substrate [90]. The presence of higher actin concentrations near pillars indicates coupling with the substrate at these location, and possibly the formation of focal adhesion points.

The traction forces exerted by neurons are reported on graphs B to E in Fig.3.15. Histograms on graph B show different distributions of forces according to pillar diameter. The mean and maximal net force per cell were averaged and plotted as function of pillar stiffness on graph C. The corresponding effective moduli were added on the top x-axis. A significant decrease of the mean and maximal forces can be observed for cells on the softest configuration D2 compared to D3 and D4 (Fig.3.15C). No such differences is observed between D3 and D4. This seems to indicate that the threshold force that can be applied by soma is reached at D3, and greater force cannot be applied on D4. Therefore, the soma might not be able to integrate the mechanical differences between D3 and D4.

The size of the soma influences the forces applied on the substrate. This is well showed on graphs D and E. In particular, the sum of the forces applied on all pillars by a cell demonstrates a strong linear correlation with soma spread area (Fig.3.15E). Additionally, for equivalent spread areas, there was no important difference in the total force applied by a cell found on D2, D3 or D4. Thus, the prevalence of large spread areas on D3 or D4 explains the difference in the averaged mean and max force of graph B. This is corroborated by the previous result which show a dependance of spread area on pillar stiffness (Fig.3.12). The average force per cell as function of spread area logically shows increasing force values between the more flexible D2 (with lots of bend pillars) to the more rigid D4 (with fewer pillar per cell).

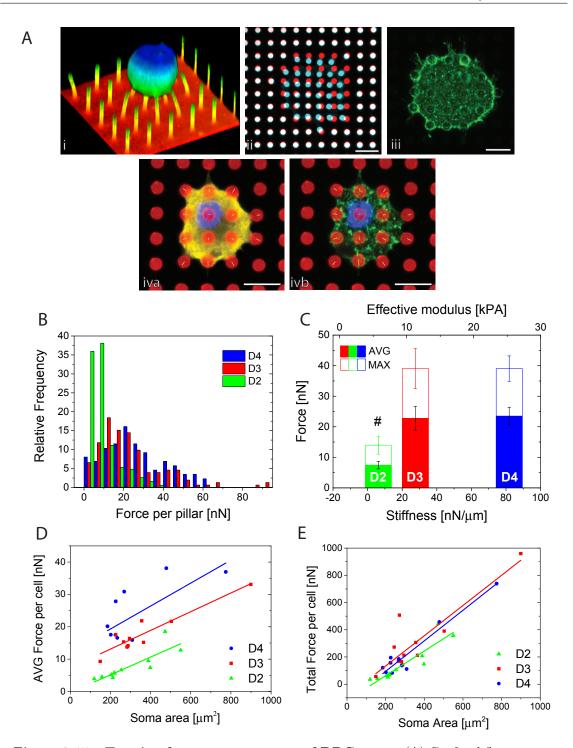


Figure 3.15 – Traction force measurements of DRG soma. (A) Confocal fluorescence images used for calculating pillar displacement under traction forces applied by cells. i) 3D representation of a soma on S7, with color-coded height. ii) Superimposed image of pillar top (red) and bottom (cyan) showing displacement. iii) Actin cytoskeleton forming puncta around pillars and soma periphery. iva+b) Soma bending pillars (red) with displacement vectors shown for each pillar. Microtubules and actin are in yellow and green, respectively. All scale bars =  $10\,\mu\text{m}$ . (B) Histograms of the forces regrouped by surface D2, D3 and D4. (C) Mean and maximal forces applied per cell. Bar height are averages from 10 to 12 analysed cells. Significance level: #P < 0.001 (D-E) Average and Total forces per cell as function of soma spread area. Curves are linear fitting from the data.

# Results - Macrophages

The reaction of macrophages to the micropillar topography is of particular interest here, given their importance in the modulation of inflammation reactions. The effect of both pillar spacing and diameter was tested with Chip 1 and Chip 9. The macrophages used in this experiment came from a murine immortalized cell line of bone marrow-derived macrophages. These immune cells, which pertain to the monocytic lineage, are undifferentiated precursors of the macrophages. Monocytes circulate in the blood and are recruited by inflammation signals at the site of infection or injury. Upon activation, they divide and differentiate into mature macrophages with different phenotypes. Here, the initial interaction and attachment of these cells on micropillar-patterned surfaces is explored.

#### 3.4.1 Attachment

The adhesion of macrophages was probed on micropillar arrays and compared to reference substrates for cell culture, such as glass and polystyrene petri dishes. The substrates were coated with PDL, which is the standard procedure for culturing these cells on petri dishes. Laminin was not used, as it is not required for the attachment of cells, and might interfere with our test by facilitating adhesion on all surfaces.

The cultures were examined after 2 DIV. The number of adhered cells was quantified on the different surfaces. It allowed to assess the initial capacity of attachment of the cells, which did not replicate extensively at this point. A global view of Chips 1 and 9 is shown on Fig.3.16. The cells detected by DAPI staining are visible as white dots on the dark green background, which is the false-colored bright-field image. The borders of the arrays are indicated by yellow dashed lines. Multiple images were taken and stitched to produce the global view.

Strikingly, the cells are almost exclusively located on surfaces with pillar arrays on both Chips. The graph on Fig.3.16 depicts the cell number as function of substrate. The Flat control has the lowest of all macrophages count, with significant difference compared to all

other conditions. The plastic petri dishes had the second lowest count, and most micropillar configurations had comparable values to the glass substrate. A slight increase was seen on the soft D1 compared to the stiffer surface D3 and D4. The interpillar spacing demonstrated a strong effect on macrophage attachment. The cell number increased markedly with increasing interpillar gap distance. The array S7 had almost 10 times more cells than Flat PDMS, and 2 times more than other configurations (Fig.3.16).

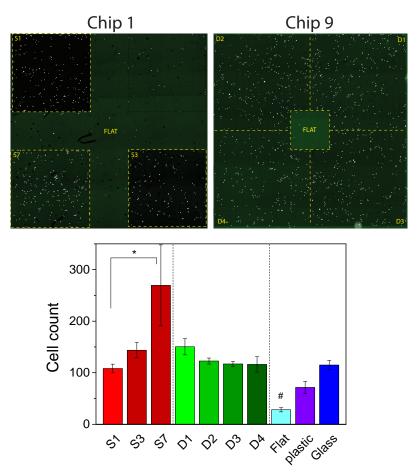


Figure 3.16 – Attachment of macrophages after 2 DIV. The upper panel of images show the global view of Chip 1 and 9, assembled by stitching images of 5x magnification. DAPI (white) and bright-field (dark green) images are merged. The bar graph represents the cell count on the different surfaces, averaged between at least 4 independent samples, and error bars the SEM. Significance levels: #\*P<0.05.

The effect of substrate stiffness on cell adhesion showed contradicting indications between controls and Chip 9 arrays. Among controls, the number of cells increased gradually with the elastic modulus of the substrate. At the lower end, PDMS ( $E = 1.95\,\mathrm{MPa}$ ) had 4 times less cells than glass ( $E \approx 70\,\mathrm{GPa}$ ). One should note that the modulus cannot be considered as the sole determining element in the increase of cell attachment, as surface chemistries are different between these substrates. Indeed, we previously saw that the absorption of laminin to the surface varied among these materials (Section 2.3.4).

As the effective modulus of PDMS was lowered with micropillars from the MPa to the

kPa range, the cell count augmented dramatically instead of decreasing. Variations of surface stiffness on D1 to D4 did not show remarkable differences between them. These observations seem to indicate that the cells are not particularly sensitive to the mechanical effect of pillars. The topography however might be the principal parameter inducing more robust cell attachment.

## 3.4.2 Morphology

To further study the attachment of cells on micropillars, their actin cytoskeleton was observed and their morphology assessed. The panel on Fig.3.17 A shows representative fluorescence images of macrophage stained for actin on the different surfaces. Cells on the control surfaces adopted round and compact shapes, without formation of actin stress fibers. In contrast, cells on micropillars displayed more complex and spread shapes, with distinctive rings of actin around pillars. These structures were observed as well on Schwann cells from the DRG cultures. The intensity of the actin signal at these sites compared to the rest of the cytoskeleton suggest strong anchoring to the PDMS pillars.

The morphology of macrophages was quantified in terms of spread area and circularity. A considerable increase in cell area was shown for cells on micropillar surfaces compared to the flat control (Fig.3.17 B). Additionally, the index of circularity indicated that cells were almost perfectly round on flat topography, compared to micropillars conditions (Fig.3.17 C). These observations can be correlated with the reduced number of macrophages on flat PDMS. Tight anchoring of a cell to its substrate, suggested by cytoplasmic spreading, is generally associated with increased cell attachment and proliferation. Altogether, these results give further indications that the macrophages are initially weakly bound to the PDMS interface upon seeding. However, as they encounter micropillars, the presence of three-dimensional structures seem to provide potent anchoring sites, and thus enhance their attachment capacity. This strong response to topography, with pillars partially or entirely enclosed in cytoplasmic processes, might originate from the attempt of the macrophage to internalize the pillars, as part of a phagocytosis process.

Interestingly, significant difference were found between the spread area of macrophages on soft matrices D1 and D2, compared to D3 and D4. With few exceptions, cells generally adopt smaller areas on soft versus stiff substrates. However, this difference between D1/D2 and D3/D4 is not reflected by smaller cell number on the graph from Fig.3.16. Thus, it is more probably simple geometrical considerations which alter the spreading of macrophages here, and not the mechanical flexibility of pillars. By inspecting the actin cytoskeleton of cells on Chip 9, we observe increasing number of actin rings as the diameter of pillars

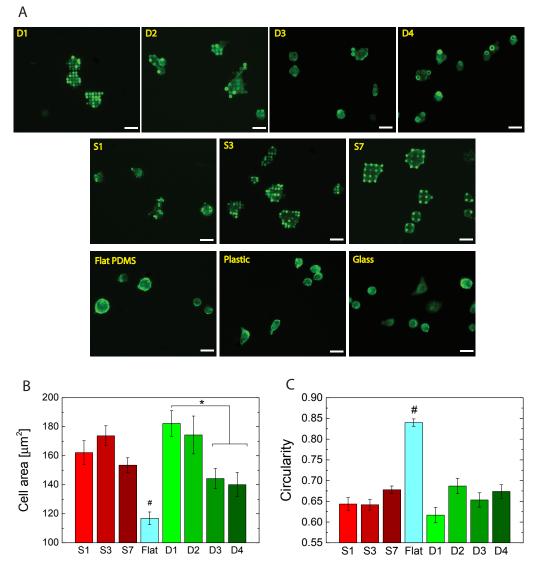


Figure 3.17 – Morphology of macrophages on Chip 1 and 9. (A) Fluorescence images of the actin cytoskeleton of macrophages on the different surfaces. Scale bars=20  $\mu$ m. Graphs of the mean cell area (B) and circularity (C) of macrophages. Error bars represent  $\pm$  1 SEM. 87 to 278 cells were analysed cells per condition. Significance levels: # \* P < 0.001.

decreases. Cells on D4 are able to form 1 to 3 actin rings around pillars, whereas tens of pillars are surrounded by actin rings underneath cells on D1 (Fig.3.17 A). Thus, the potential for spreading of these cells might be augmented by the smaller size of pillar diameter. This hypothesis is further advocated by the results of spread areas on the Chip 1 arrays. The constant pillar diameter on Chip 1 corresponds to the one found on D1. Accordingly, the values of spread area on chip 1 were close to the one obtained on D1/D2, regardless of the the spacing conditions S1, S3 or S7.

## Results - Adipose-derived stem cells

Adipose tissues were found to host a population of multi-potent mesenchymal stem cells which have the ability to differentiate into various cell types [100]. These adipose-derived stem cells (ASC) have the advantage of being readily available from fat tissues obtained by standard liposuction procedure. Of particular interest here is the commitment of these cells into a Schwann cell-like phenotype. The feasibility of such differentiation of ASCs has been demonstrated some years ago [101]. Their application in tissue engineering strategies for enhancing nerve regeneration has been explored on nerve conduits [70].

The attachment and survival of ASCs are critical parameters to address in the context of cell-based therapies. These parameters can be modulated by several properties of the substrate, such as ECM composition and mechanical rigidity [102, 103]. In this section, we assess if the adhesion and morphology of ASCs can be modulated by topographic or mechanical cues presented by the micropillar environment.

#### 3.5.1 Stem cell morphology and phenotype

The stem cells were extracted from the inguinal and visceral adipose tissue of adult Sprague-Dawley rats. The cells used for attachment experiments were kept undifferentiated, and originated from early subcultures (passage 3 to 4). As a first step, the morphology of ASC was observed on different substrates. As seen on Fig. 3.18, ASC on glass surface spread and formed prominent actin stress fibers. Bright red spots at the periphery of the cells indicate clustered vinculin, which delimit focal adhesion complexes linking the cytoskeleton to the substrate. On uncoated PDMS, the cells showed dramatically smaller spreading. Vinculin spots are absent, which suggest weak adhesion of cells to the substrate. However, when PDMS is coated with laminin, cells show very similar morphology as on glass, with large spread areas and numerous bright vinculin spots. In these experiments, the response of stem cells to micropillar arrays was assessed on substrates coated with PDL only. The absence of ECM molecules on the surface constituted a more challenging environment for cell adhesion and spreading. This accentuated the effect of the micropillars on cell density

and morphology compared to flat surface.

The phenotype of ASC was tested by observing the expression of biomarkers specific to stem cells (Fig.3.18B). The Stro-1 protein is cell surface marker which is expressed by mesenchymal stem cells and widely used for identifying stem cells. Nestin is a commonly used marker for neural progenitors and glial lineage. Expression of both markers, as seen on the pictures of Fig.3.18B, indicated that the cells had effectively a stem cell phenotype, with the potential to differentiate into glial lineage. By stimulation with appropriate growth factors, they can differentiate into Schwann cells, which could be used for cell-based nerve regeneration strategies.

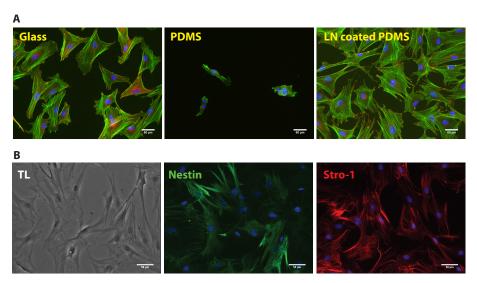


Figure 3.18 – Characterization of adipose-derived stem cells. (A) Fluorescence images of ASCs on Glass, PDMS and laminin-coated PDMS substrates. Actin=green, Vinculin=red, DAPI=blue. (B) Immuno-detection of the stem cell biomarkers nestin (green) and Stro-1 (red) on cells cultured on glass substrate. TL=bright-field image. Scale bars = 50 μm.

#### 3.5.2 Attachement and spreading

Cultures of ASC were performed on Chip 9, in order to probe their attachment on surfaces with different effective moduli. The samples were fixed after 3 DIV. Cells had proliferated and spread on glass substrates by that time. Similarly to the results obtained on Fig.3.18A, the shape and number of cells on Flat PDMS remained comparatively low. However, the presence of micropillar arrays dramatically increased the adhesion of ASC. The number of cells more than doubled between Flat and Chip 9 configurations (Fig.3.19B). Interestingly, a quasi-linear increase of cells was observed as the effective stiffness of the arrays decreased from D4 to D1. It constitute an indication that ASC actively respond to the gradual change in pillar stiffness. To further investigate this question, the morphology of cells was observed and quantified. Individual cells on the different topographies can be seen on Fig.3.20A, with vinculin and actin staining.

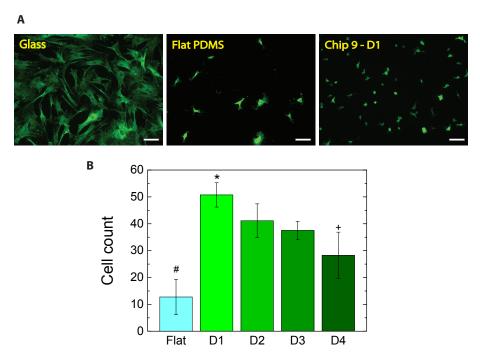


Figure 3.19 – Attachment of adipose-derived stem cells on Chip 9 arrays. ASC were seeded on PDL-coated substrates and cultures were fixed after 3 DIV. (A) Fluorescence images taken at 10x magnification. The samples were stained for vinculin (green) and DAPI (not shown). Scale bars =  $100\,\mu\text{m}$ . (B) Bar height show the mean cell number (from 8 to 40 FOVs)  $\pm$  1 SEM. Significance levels: \*+P < 0.05; #P < 0.001.

ASC adopted very contrasting morphologies in response to the different substrates. Globally, cells on softer surfaces were smaller and rounder compared to stiffer ones. Quantification of cell spread area and circularity confirmed this observation. Flat surfaces supported cells with spread areas at least 50 % larger micropillar surfaces (Fig.3.20B). Gradual decrease of spread area was observed between the stiff (D4) to soft (D1) micropillar configurations. These results are corroborated by the index of circularity of cells. Consistent with smaller spread area, ASC on micropillar surfaces displayed significantly rounder somas than on flat surface. Taken together these results seem to indicate that the ASC are able to integrate the gradual mechanical flexibilities of pillars and respond accordingly by modifying their morphology. More importantly, the number of cells was far greater on micropillar arrays than on flat PDMS. This is a major advantage in the context of a cell-based tissue engineering strategy. For instance, the loading of stem cells on artificial nerve conduits might be far more efficient with micropillar-textured surfaces. The increased density of attached cells might not only enhance the outcome of neural regeneration, but also reduce the time and resources necessary to expand the population of Schwann cells to the required level.

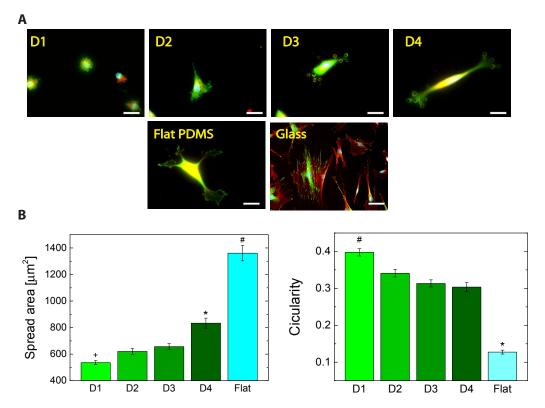


Figure 3.20 – Morphology of adipose-derived stem cells on Chip 9. (A) Fluorescence images of individual cells were taken at 63x magnification. Samples were stained for vinculin (green) and actin (red). Scale bars =  $20\,\mu\text{m}$ . Graphs in (B) depict the mean spread area of cells and mean circularity index. 191 to 349 cells were analysed per condition. Significance levels: #\*+P<0.001.

# Discussion

The general objective of this in vitro work was to evaluate whether PDMS substrates textured with micropillars could induce quantitative changes on the behavior of DRGderived neurons and glial cells in vitro. The rationale behind the design of micropillar structures lies mainly with the ability to modulate and reduce the perceived stiffness of the surface compared to a corresponding flat substrate [25]. Such reduction of stiffness is a priori desirable for matching relatively soft tissues found in the nervous system. The influence of substrate stiffness on DRG neurite growth has been recognized 15 years ago [22] and since then, a growing body of knowledge has been brought to the field of neuronal biomechanics [79, 104, 61, 105]. DRG neurons are considered as highly mechanosensitive cells, with peak sensitivity between 0.45 to 3 kPa [61]. Outgrowth and neurite traction forces are both dependent on substrate stiffness, with a maxima observed for Young's modulus around 1 kPa [61]. On the other hand, glial cells in the central and peripheral nervous system thrive more on stiffer substrates [64, 106, 107]. An optimal elastic modulus value of 7.45 kPa was proposed for Schwann cells on polyacrylamide gels [62]. Taken together, these observations indicate an asymmetric situation in terms of optimal growing conditions between neurons and glial cells. These differential mechanosensitivities might play a role in the early structuring of the nervous system, and reflect on the mechanical heterogeneity of the PNS [90]. Despite these disparities, glial cells and neurons constitute a symbiotic system, with important paracrine signalling mechanisms, influencing each other's fate. It is therefore particularly relevant to study both cell types simultaneously when investigating on a potential neural tissue-material interface. In this work, the response of DRG neurons and glial cells was analysed near confluence (7 DIV). Few studies are currently available on cultures of PNS cells under such conditions.

#### 3.6.1 Mechanical effects of micropillars

The range of effective stiffness produced in this study encompasses compatible values for DRG cells, with minima around 0.7 kPa for D1. Results indicated that glial cells were affected the most by the substrate stiffness variations, whereas neurons remained mildly

affected. Similar situations have been reported for mixed CNS culture [64, 108, 109].

Glial cells showed a quasi-linear reduction of their population as stiffness decreased from 27.0 kPa on D4 to 0.7 kPa on D1 (Fig.3.10 D). In particular, the softest surfaces D1 and D2 supported significantly fewer cells. This points out to a negative effect of low over intermediate or high stiffnesses, in accordance with previous studies [64, 110]. Neurons did not show preference for soft substrates, with a slight positive trend towards stiffer textures. This behavior might reflect a specificity of PNS neurons over CNS ones. Admittedly, cells from the peripheral nervous system face stiffer environments than in the CNS [105]. The result for D1 (0.7 kPa) corroborate observations that DRG neurons show steep decrease in growth for stiffness below 1 kPa [61]. An optimal substrate rigidity for soma adhesion is potentially found at higher modulus values [79]. The glial and neuronal cells interact and influence each other, potentially biasing a pure effect of micropillars. A strong positive correlation between the number of glial cells and neurons was observed on flat PDMS surfaces, as showed on Fig.3.21. Thus, reduced cell population on soft matrices could negatively influence the survival of adjacent neurons. The effect of lower substrate stiffness may in fact benefit more to neurite outgrowth than to soma attachment.

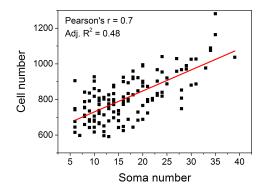


Figure 3.21 – Correlation between the number of somas and the total number of cells on flat PDMS. Cells were counted from field of views acquired at 10x magnification. The total number of cells was counted from DAPI-stained nuclei and the number of neurons from Tuj-1-positive cells. Data was generated from 127 FOVs (black squares) and fitted by a linear fitting (red curve). Pearson's r coefficient indicates a strong positive correlation between number of cells and somas.

Neuronal somas interact mechanically with micropillars by bending them (Fig.3.9 A). The influence of pillar flexibility was observed through morphologic parameters. Many cell types are known to adopt small, compact shapes on soft substrates, while high modulus surfaces induce spreading in complex forms [111, 112]. This study confirms it is also the case for DRG neuron somas (Fig.3.12 B). The softest configurations D1 and D2 displayed populations shifted towards small and round somas. On the other hand, the stiffer surfaces D3 and D4 were virtually equal to flat PDMS. These larger pillars did not reach an

appreciable flexibility for soma to induce a modification of their morphology. Interestingly, D1 and D2 are also significantly different from one another, indicating a stronger effect of stiffness lower than 1 kPa. The histograms of soma areas and circularities reveal a relatively stable percentage of small round somas, regardless of the substrate condition. However, the shapes of the distributions show longer tails for stiffer pillars, indicating an increase of area for the neurons that were already relatively spread. This suggests the presence of 2 populations of neurons with distinct reactions to pillars, and by extension distinct mechanosensitivities. This would not be entirely surprising, as harvested primary DRG neurons are inherently a heterogeneous population, with various types of somas with different characteristics.

Significant differences of morphologies were found again for the softest surfaces D1 and D2 compared to the other conditions, thus echoing the result of cell densities. Taken together, these observations point to an upper stiffness limit situated between D2 (4 kPa) and D3 (12.3 kPa) where the mechanical effect of pillars would start to fully impact the glial and neuronal cells. This range correlates with the upper limit of values reported for DRG elasticity and optimal Schwann cell growth [105, 62]. It also concurs to the fact that cells are mainly sensitive to a range stiffness comparable their own cortical rigidity. Interestingly, this hypothetical threshold of mechanosensitivity between D2 and D3 is also found with the results of the soma force tracking experiment performed here. Neurons on D2 applied weaker traction forces compared to neurons on D3. However, the stiffer D4 did not induce higher forces than D3. This suggests that the DRG is unable to further deform the pillars once a threshold stiffness is exceeded. Therefore the flexibility of these stiffer configurations might not distinguishable for the DRG neurons.

A linear correlation was also observed between projected areas of the soma and the total force summed on all pillars. The slopes of the fitting curves were relatively close for all configurations, indicating that the size of the soma is the primary determinant of the total applied force. This implies that a higher fraction of neurons with large somas are present on the stiffer configurations, which was quantitatively confirmed here. Finally, it should be noted that the change in pillar stiffness is accompanied by a change in the surface area available for cells on the top of pillars. This may also influence cell attachment and spreading. However the total surface area for a defined zone is kept constant between all diameter configurations, providing the same quantity of available ECM for cells.

# 3.6.2 Topographic effects of micropillars

Similarly to diameter configurations, the interpillar spacing affects primarily the response of glial cells. The 2 largest spacings S3 and S7 resulted in smaller cell populations, compared to S1 and Flat. Several potential mechanisms responsible for these differences can be envisioned. First, a perturbation of the cytoskeletal assembly of cells spreading between pillars may affect important events during mitosis. Cells spreading on S3 and S7 have higher portions of free standing cytoplasm between pillars, which cannot engage adhesion with the substrate. This can translate to higher cytoskeletal tension, due to the reduced number of focal adhesions and their fixed distance. On the other hand, the S1 configuration presents an almost continuous substrate with its dense pillar tops. Thus, cells may experience less tension compared to S3 and S7, thus avoiding the same perturbations of cellular proliferation programs. A second factor might be the increased surface area of the densest array S1. ECM molecules of laminin are covering the entire surface of the array, thus provide higher densities of attachment points for integrin engagement compared to S3 and S7. Interestingly, S7 demonstrate a weaker effect on cell density than S3. This trend might indicate that the limit of cell spreading without contact to the bottom is found between 3.5 and 7.5 µm, and consequently cells on S7 partly reside on the interpillar flat area.

## 3.6.3 Integration and orientation of neurite networks in micropillars

All DRG neurons extended neurites across the micropillar patterns, mainly without underlying solid support. Neurites were able to explore the Z-dimension of pillar matrices and were found at all levels of pillar height. However, the majority of neurite networks were established at a level corresponding to the upper half of the micropillars, independently on the pillar spacing (Fig.3.9C). In previous studies, neurites bridging nano- and microscopic grooves have been reported [113, 114]. Projecting neurites continually assess their spatial environment, and growth cone pathfinding guided by mechanical contractile and tensile forces applied along the growing neurites have been proposed as a critical element for explaining this phenomenon [90]. DRG neurons generate internal neurite tension, which can increase as the interconnected network is formed and undergoes rearrangement [61]. The internal neurite tension is mediated by the coupling between neurite adhesion points and substrate. It is thus interesting to observe that neurites were positioned on the top part of pillars, where they might fully experience flexibility of the pillar geometry.

Orientation of neurites along the pillar grid was shown to be strongly dependent on interpillar spacing. Dense pillar matrices (S1) induced substantial neurite alignment. Similar effect on neurites was observed in hippocampal neurons seeded on silicon surfaces

with comparable spacing dimensions [94]. In our case, Schwann cells might also participate in the alignment of neurites. A strong correlation was observed between the orientation of Schwann cells and neurite on all surfaces (Fig.3.14). Thus, the pillar grid may act indirectly by influencing the orientation of Schwann cells as well. However these elements are not assessed individually here and the overall effect only should be considered.

Interestingly, although the topography of the pillar grid is relatively isotropic in both the  $0^{\circ}/\mathrm{Sx}$  and  $90^{\circ}/\mathrm{Sy}$  directions, neurites on S1 demonstrate a strong preference for  $0^{\circ}/\mathrm{Sx}$  over  $90^{\circ}/\mathrm{Sy}$ . A possible explanation for that effect can be found with the  $20\,\%$  shift of interpillar spacing distances between Sx (1.0 µm) and Sy (1.2 µm). At this scale, the slightly more compact arrangement of pillar in the Sx direction might have tweaked the alignment in favor of this direction over the other. This hypothesis implies neurites respond to nanotopographies [115] and advocates for the investigation of spacing at much smaller scale than the on presented on Chip 1. Furthermore, Schwann cells are known to align their cytoplasmic process in one direction when grown with sufficiently high density (observable on Flat condition in Fig.3.14). On S1 matrices, the Schwann cells locally formed compact populations with cytoplasmic extensions aligned in the  $0^{\circ}/\mathrm{Sx}$  direction (Fig.3.6 B). These regions correlate with high density and high alignment of neurites in the same direction (Fig.3.14). Therefore the presence of Schwann cells certainly alters the DRG neuron extensions. However, this set of experiments does not allow to ascertain the biological from the topographical triggering element to neurite alignment.

#### 3.6.4 Behaviour of macrophages and stem cells on micropillars

Neurons and Schwann cells are not the only relevant cell type to consider in the context of an implanted neural regenerative device. Immune cells such as macrophages are major actors of the inflammation reaction and modulate the response to foreign materials both on the short and long term [84]. Upon activation, macrophages can assume diverse roles and functions, reflected by different phenotypes. Classification of macrophages into 2 main classes has been proposed: the classically activated macrophages (M1), which are proinflammatory, and the alternatively activated macrophages (M2), which have wound-healing and tissue remodelling capabilities [116]. The timely sequential polarization of macrophages into both phenotypes is thought to impact the success of tissue regeneration process, as well as the performance of implanted biomaterial [117][118]. Modulation of the phenotype of macrophages is currently one of the trending strategies for improving the outcome of regenerative therapies and long-term medical implant performance [117, 119, 120]. Some of the approaches to control macrophage polarization rely on the physical characteristics of the

biomaterial, such as roughness, porosity and stiffness [121, 122, 123, 124]. In this regard, the patterning of surfaces with micropillars can provide topographical and mechanical cues which might impact macrophage polarization.

In this chapter, experiments on the effect of micropillar topographies on the behaviour of monocytic precursors of macrophages were presented. All micropillar configurations provoked dramatic increase of macrophage adhesion, compared to flat PDMS. The interpillar spacing rather than pillar flexibility was found to impact adhesion. Observation of the actin cytoskeleton revealed intense actin polymerisation around pillars, forming tight rings around them. These structures may provide firm anchoring to the cells, explaining their higher density compared to flat surface. Whereas actin rings were found around all sizes of pillar, those with diameters on the order of 1 µm induced the most cell spreading of all conditions, along with slightly higher densities. One can hypothesize that pillars with such size may trigger phagocytic reactions from the macrophages, in an attempt to internalize these foreign elements. Interestingly, the rod-shaped bacilli bacteria commonly phagocytized by macrophages have a geometry and dimensions comparable to micropillars from the D1/S configurations. This geometrical resemblance might thus induce phagocytic process by the macrophage. The impossibility to fully internalize the pillar may lead to frustrated phagocytosis, leading to the formation of the actin rings. Such phenomenon has previously been observed on surfaces micro-patterned with immunecomplexes [125].

The higher number of macrophages on the micropillars can be a priori considered as a negative indication for reducing foreign body reaction. Increased densities of macrophages may trigger their fusion into multinucleated foreign body giant cells, which are notably implicated in the formation of the fibrotic capsule [84]. However, these experiments are restricted to 3 days of culture and only densities and morphology were assessed. Events occurring at longer time scales should be considered to fully characterize the effect of pillars on macrophages and foreign body reaction. Complementary analysis, such as cytokine release profiles, may provide information on the polarization of macrophages on micropillars.

#### 3.6.5 Behaviour of adipose-derived stem cells on micropillars

Mesenchymal stem cells (MSC) are currently considered in number of applications aiming at the regeneration of living tissues. They benefit from fast growth rates, multiple differentiation possibilities and reduced immunogenic potential, conferring them important assets for cell-based therapies.

A source of MSC was discovered in the stromal vascular fraction of adipose tissues. These adipose derived stem cells (ASC) share comparable phenotypic and gene expression profiles to bone marrow derived mesenchymal stem cells (BMSC), and are able to differentiate into many different cell types [101, 100]. Some of their advantages over BMSC include the ease of tissue isolation, the less traumatic harvesting procedure for the patient and the large quantities available [101]. The differentiation of ASC into Schwann cells constitute a promising alternative to the use of nerve-derived Schwann cells for clinical applications. Currently, adult Schwann cells have to be extracted from a donor nerve, which is associated with morbidity and slow cell expansion rates. ASC differentiated into Schwann cells were shown to enhance neurite outgrowth and nerve regeneration [101, 126]. The loading of ASC-derived Schwann cells into nerve regenerative conduits or interfaces might thus ameliorate the functional outcome of these devices.

In this thesis, a preliminary study was conducted to assess the initial adhesion and morphology of undifferentiated ASC interacting with micropillars of different flexibilities. Similarly to the results obtained for macrophages, the number of adherent ASC was multiplied by a factor 2 or more on all micropillar configurations, compared to the flat PDMS control. However, in contrast to the macrophages, ASC did not show intense actin formation around pillars. Their morphology, characterized by spread area and circularity, indicated that they integrated the mechanical flexibility of pillars. The softest surface D1 induced significantly smaller spread area and greater circularity compared to all the other configurations. The capacity of adipose-derived stem cell to change their morphology in response to substrate stiffness has been reported [127]. From these observations, we can hypothesize that the increased density of cells on D1 is linked to the lower stiffness of this surface. Adipose tissue is among the softest in the body [21]. Stem cells residing in this tissue are thus prone to thrive in environments with very low stiffness. This could hypothetically explain their preference for the micropillar-modulated stiffness found on arrays D4 to D1. However, the effect of the topography alone should be addressed to ascertain this hypothesis. Interestingly, the higher number of ASC on micropillars constitute a potential way of increasing the attachment and survival of cells loaded onto silicone constructs aimed tissue regeneration.

The mechanical patterning of the substrate was previously demonstrated to alter the adhesion and orientation of ASC [103]. Interestingly, the mechanical properties of the cells themselves were correlated to lineage-specific commitment and metabolite production [128]. Softer cells were more prone to differentiate into adipocyte than chondrocyte. Hypothesizing that ASC demonstrate mechanical phenotypes associated with preferred lineage, the cells found on the soft D1 surface might therefore differentiate preferentially into neuronal or

glial lineage. This modality might constitute a practical way of inducing potent cells for differentiation into neuronal or glial cell types.

# Conclusion

Biological and physical cues are essential components in regenerative medicine. In nerve repair, scaffolds with tailored mechanical and physical properties are an essential alternative to autografts. In this regard, surfaces textured with arrays of micropillars create a pseudo-3D environment presenting mechanical and topographic cues capable of modulating the tissue-implant interface at the cellular level. In this chapter, the interaction between primary cells from DRGs and micropillars with defined geometrical characteristics was assessed in vitro.

Pillar diameter and spacing were varied in order to modulate apparent stiffness and topography of the surface. Glial cell density was decreased by the most flexible and least dense pillars (D1, D2, S3, S7), and DRG neurons did not show strong preferential distributions across the evaluated matrices. The surface area of somas was shown to decrease on pillars with small diameter, most probably as a result of lowered apparent surface stiffness. The range of stiffness affecting DRG morphology, from 0.7 kPa to 12.3 kPa, was comparable to previously reported values. Similarly, traction forces measured by pillar displacement indicated that DRG neurons reduced the average net force applied on the substrate when the stiffness of the pillar decreased to 4 kPa. Neurites aligned with pillar array of short interpillar distance ( $<2\,\mu m$ ), and resided mostly near to the tip of the pillars. Finally, macrophages and stem cells demonstrated dramatic increase in cell number on micropillars compared to flat PDMS. For macrophages, frustrated phagocytosis might explained this increased attachment, whereas stem cell relied on mechanical and topographic features of the micropillars.

Taken together, these results point to contrasting effect of micropillars in the context of peripheral nerve regeneration. Very soft configurations should be avoided in order to preserve the proliferation potential of DRG-derived glial cells. The reduced populations of glial cells on soft pillar might negatively impact neuronal growth, even if neurons are favorable to softer environments. On the other hand, a soft and compact micropillar configuration will enhance the adhesion of stem cells. This could be useful for various

applications, such as patterning of cells on surfaces, studying mechanically modulated differentiation, or for nerve regeneration strategies using cell-loaded constructs. Further refinement of the micropillar array geometry might help tailoring more precisely the reaction of the different types of cell.

# EVALUATION OF MICROPILLAR TEXTURE IN VIVO

This chapter first describes the fabrication of 2 designs of micropillar-coated PDMS nerve conduits. The effect of the micropillar texture on sciatic nerve regeneration is assessed in terms of axonal regeneration and macrophage response after up to 3 months of implantation.

# Contents

4.	1 Introduction
4.	2 Material and Methods
4.	3 Results
4.	4 Discussion
4.	5 Conclusion

# Introduction

In parallel to the experimentation and observations made in vitro, the effect of micropillars was studied in an in vivo model. With the applications on regenerative peripheral nerve interfaces in mind, the model was chosen so as to present the closest situation to a silicone cuff electrode. The implants were designed as tubes made out of PDMS, with a micropillar texture covering the inner surfaces of the tube. This simple tubular structure corresponds to the elementary design of nerve guidance conduits [129, 130]. These devices seek to replace the nerve autograft, which is the current gold standard for peripheral nerve repair. The animal model chosen here for investigating nerve regeneration was the transection of the sciatic nerve of adult Lewis rats. An important amount of the research on nerve regeneration has made use of this model to unravel fundamental biological mechanisms and shape novel therapeutic strategies.

In this chapter, the process for the fabrication of micropillar-textured PDMS conduits is detailed. Dense arrays of micropillars were patterned on the curved surfaces of the tubes. Their aspect ratio provided a reduction of the effective stiffness of the surface equivalent to 2 orders of magnitude compared to bulk PDMS, reaching the kPa range. Such modulation of the mechanical properties of an implant may impact multiple levels of the tissue response. The navigation of axons, which thrive in soft environment, and the reaction of immune cells are targeted in particular. Let alone the mechanical stealth effect, the topography created by micropillars has also the potential to influence cellular behaviour in vivo, such as attachment and migration, which could ultimately affect the success of nerve regeneration. In the previous chapter, we notably observed the physical guidance of growing axons by pillars elements, as function of their interpillar spacing. Pilot experiments also revealed the influence of micropillars on the adhesion of macrophages, which was mainly modulated by the topographic cues. With these considerations in mind, the main parameters that were quantified to assess the outcome of micropillars on nerve regeneration were first the tissue and axonal growth, and secondly the macrophage distribution.

Elements of the peripheral nerve anatomy, injury and regeneration are introduced in the

following sections. Cellular events occurring upon implanted foreign material and strategies for nerve repairs are then reviewed.

#### 4.1.1 Peripheral nerve injury and regeneration

#### Anatomy

The peripheral nervous system (PNS) designate the nerves emerging from the spinal cord in the central nervous system (CNS) and expanding throughout the entire body in mammals. These nerves are composed of efferent and afferent fibers, respectively transmitting motor and sensory information to the CNS. The structural anatomy of a peripheral nerve is organized into a nerve trunk containing a bundle of fascicles, each composed of several axons, which can be myelinated or not (Fig.4.1). The outermost layer is the epineurium, a protective connective tissue made principally of collagen, fibroblasts and fatty tissue. It holds together the fascicles and forms a condensed sheath on the outside, delimiting the nerve trunk. Each fascicle is surrounded by a dense perineurial layer, formed by flattened cells (i.e., fibroblasts) and collagen. With its high mechanical resistance, the perineurium is the main contributor to tensile strength in nerves. The innermost layer is the endoneurium, which encloses individual axons and their Schwann cells sheath in a structure called the endoneurial tube. Composed of a loose collagenous matrix containing fibroblasts, resident macrophages and mast cells, the endoneurium nourishes and protects the neural processes. Peripheral nerves are irrigated by complex network of longitudinally oriented blood vessels. The main supply channels lie in the epineurium and are connected to a capillary plexus in the endoneurium. Endoneurial arterioles and venules are impermeable to most macromolecules, acting as an extension of the blood-brain barrier [131].

## Injury and Repair

Unlike neurons from the central nervous system, peripheral nerves have the potential to regenerate their neuronal processes to a certain extent. When a nerve endures a traumatic lesion, a cascade of metabolic and morphological changes takes place in the cell soma, in the axonal stumps near the injury site, as well as in the muscles end-plates and sensory receptors. A retrograde signal is sent from the site of injury to the cell body, changing its protein expression profile to decrease neurotransmitter-related substances and increasing the production of structural material for regeneration. Retraction of dendritic processes also occurs [133]. The proximal part of the severed axon degenerates generally to a limited extent, but death of the entire neuron can also occur depending on the severity of the

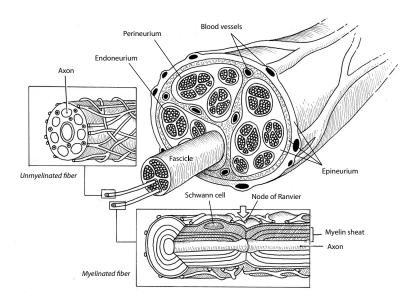


**Figure 4.1** – **Anatomical structure of a peripheral nerve.** Schematic depiction of the different structural layers composing a nerve, with myelinated and unmyelinated axons. (Adapted from Lee et al. 2000 [131]).

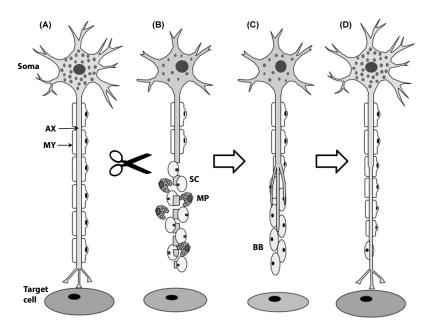


Figure 4.2 – Schematic of nerve injury and regeneration mechanisms. AX: axon, MY: myelin sheat, SC: Schwan cell, MP: macrophage, BB: bands of Büngner (A) Normal nerve with synaptic connection to target cell. (B) Transection results in Wallerian degeneration. Schwann cells and macrophages phagocyte the degraded segments. Cell soma switch to regeneration-related behavior. Target cell might suffer atrophy when synaptic contact is lost. (C) Scwann cells form bands of Büngner which guide and promote growth of the regenerating sprouts. (D) Synaptic connection is re-established but axon remains smaller in diameter than initially, with shorter internodes. (Adapted from Navarro et al. 2007 [132]).

trauma. Afferent and efferent neurons are not affected in the same way. Primary afferent neurons were shown to be more prone to die than efferent ones, with an estimated 7 to 50% total loss [132]. This imbalance between fiber type regeneration impacts the functional recovery of the nerve. On the distal side of the injury, axon stumps start to disintegrate gradually in a process called Wallerian degeneration (Fig.4.2(B)). Cellular and myelin debris are phagocytized by Schwann cells and macrophages. Attempts to regenerate begin shortly after the injury, with the formation of multiple axonal sprouts at the proximal stump. Successful regeneration imply that a certain number of these sprouts reach the appropriate distal target, and mature to a size close to the original axonal fiber (Fig.4.2(D)).

Four factors in particular have a determining influence on this process. Schwann cells may have the most critical role for the regeneration of the nerve. When they loose contact with the axon, a series of events takes place including the proliferation of dedifferentiated daughter cells, upregulation of growth factors and synthesis of surface adhesion molecules. Schwann cells organize themselves into a tube-like structure called band of Büngner, which serves as a guiding and growth promoting environment for regenerating axons (Fig.4.2(C)). The second factor is the production of several neurotrophic factors (NTFs), such as nerve growth factor (NGF) or brain-derived neurotrophic factor (BDNF), released by fibroblasts, macrophages and Schwann cells at the injury site as well as near cell body. NTFs promote the survival and the guiding of neurons after injury. The third factor is the presence of a basal lamina, which is a thin layer of extracellular matrix (ECM) incorporating adhesion molecules such as laminin, fibronectin, collagens and glycoproteins. It acts as a supportive scaffold for cells and was shown to promote the elongation of neurites in vivo. The last factor is the subsistence of the distal stump of the severed nerve. It supplies trophic factors that help proximal axon sprouts to navigate and reach their target organ [134, 135].

In conclusion, regeneration of an injured nerve depends on many parameters related to the severity of the trauma, including the length of the gap between proximal and distal stumps, rate of axon regeneration and correct guiding of sprouts to distal target [136, 132]. In the most severe cases, such as complete nerve transection, the loss of guiding structures and the deposition of scar tissue might prevent the axons from reaching their distal end target. As a result, the regenerating axons are misdirected and form a mass of tortuous immature sprouts and connective tissue called a neuroma [132]. Functional recovery is not assured by the sole axonal regeneration, and a maturation process involving enlargement and remyelination of the reconnected axons is needed.

## 4.1.2 Tissue response to implanted neural devices

In the context of neuroprosthetics, an essential target is to achieve a stable and efficient neural interface, not only shortly after implantation, but for potentially decades of use. The integrity of both device and surrounding tissues should be preserved on the long term, despite constraints of chemical, biological and mechanical nature, due to human body environment and activity. A key factor impacting this stability is the response of biological tissues to the implantation and prolonged presence of the device.

Two phases can be distinguished when foreign material is implanted in the body, an acute reaction occurring upon implantation, followed by a sustained chronic response. The first phase of acute inflammation is induced by the surgical insertion of the implant, as part of the normal physiological mechanism of protection and wound healing. This initial response is important for restoration of the tissue homeostasis and includes the release of neurotrophic factors and adhesion molecules, which play a supportive role on nerve regeneration [137]. Following this early response, persistence of inflammatory signals due to the presence of the implant leads to the onset of a foreign body reaction (FBR). Figure 4.3 illustrates the successive biological events that leads to the encapsulation of a foreign body. Unspecific adsorption of plasma proteins such as fibringen on the device's surface is the initial step of the FBR [4]. This triggers the recruitment of macrophages, monocytes and fibroblasts, which adhere to the surface in a process called biofouling. At a later time point, several macrophages fuse into multi-nucleated foreign body giant cells (FBGC), forming a compact layer enclosing the device and providing isolation from the local environment [138]. The space comprised between the cell membranes and the surface of the material constitutes a special microenvironment. Activated macrophages and FBGC can produce corrosive agents, such as reactive oxygen species, degradation enzymes or acids, which are released in this privileged microenvironment as an attempt to digest the foreign material [84]. Therefore, surface chemistry of the implant has to be carefully considered in order to avoid enzymatic and oxidative degradation of the material on the long term.

The ultimate step of the FBR is generally characterized by fibrotic encapsulation of the implant. Adherent fibroblasts, macrophages and FBGC modulate the deposition of fibrotic ECM as a function of activating signals at the tissue/material interface. The FBR has very detrimental effect on the interfacial communication between neurons and electrodes. The compact sheath which constitutes the fibrotic capsule is deposed around the electrodes and insulates them from the environment. It can continue to grow to several microns in thickness if the chronic response is sustained, which increases the distance between the electrodes and the target neurons [140]. More importantly, this change of ECM will

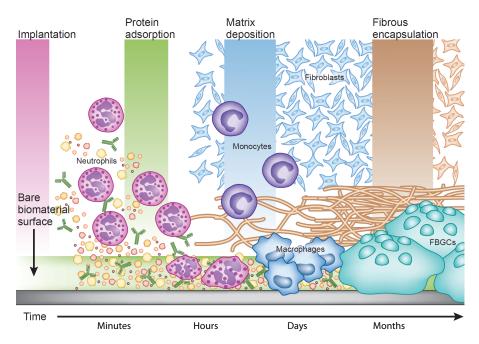


Figure 4.3 – Temporal evolution of the foreign body reaction. Immediately after implantation, host proteins from the bodily fluids are adsorbed to the surface of the material. Within hours, neutrophils interact with protein-coated surfaces and start producing proinflammatory signals (cytokines, chemokines, reactive oxygen species), which recruits resident macrophages and circulating monocytes during the following days. Fibroblasts are attracted to the implant surface by macrophage-produced signalling molecules and start depositing collagen. Later on, macrophages fuse into foreign-body giant cells (FBGC), which are a hallmark of foreign-body reaction. Within months, the implant is coated with a collagenous fibrotic layer which isolates it from the host tissue. (Adapted from Grainger et al. [139]).

alter the resistive properties of the tissue, increase the impedance of the electrode, and ultimately hinder the performance of the interface in the long-term [141]. Higher current or voltages will be needed for stimulation and the signal-to-noise ratio will decrease for recording.

The tissue response to an implant is characterized by a complex series of events depending on many intrinsic and extrinsic parameters. Tissue location is a first important factor. The potential of local cells to regenerate will affect the final outcome of the healing process [138]. For instance foreign body reaction and fibrosis in the CNS is more deleterious for the surrounding environment than in the PNS, due to the production of harmful agents for the neurons [145]. Surface chemistry of the material has a determinant role on the immunogenic potential of the device, notably influencing cell adhesion, inflammatory signals and ECM deposition. Ideal biocompatible materials should elicit minor inflammation and turn reactive cells into their inactivated state after the end of the healing response. Biomedical polymers were shown to trigger stimulation of fibroblast activity through activation of adherent macrophages, which supports the fibrotic response [146].

Surface chemistry is not the sole factor that should be considered when assessing bio-

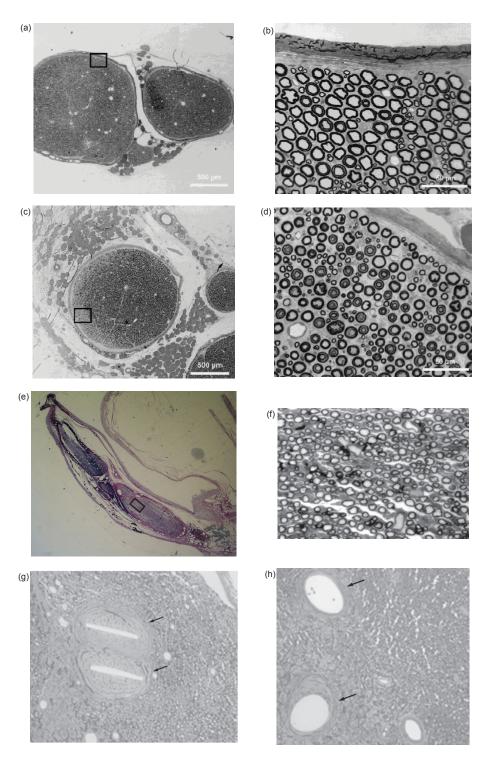


Figure 4.4 – Histological transverse section of sciatic nerves with implanted neural electrodes. (a)-(b) Control showing normal appearance of myelinated axon and perineurium (Grill et al.(2000) [142]). (c)-(d) Neve section 1cm distal to a spiral cuff electrode [142]. Subperineurial connective tissue, decreased myelination of axons and increased endoneurial connective tissue are observed. (e)-(f) Nerve section at cuff level with a narrow flat interface FINE implanted. Compression of the fascicules induced severe axonal injury and signs of neuromuscular impairment, with myelin sheath thinning and connective tissue increase (Leventhal et al.(2006) [143]). (g) Round section platinum longitudinal intrafascicular electrode (LIFE) interface and (h) laminar polyimide LIFE interface implanted for 3 months intrafascicularly. Arrows indicate fibrotic capsule formed upon FBR, composed of flattened fibroblasts and devoid of axons (Lago et al.(2007) [144]).

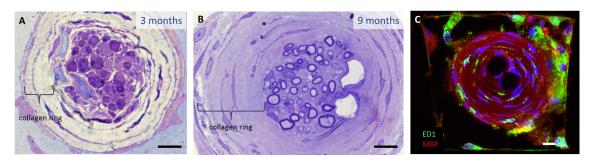


Figure 4.5 – Fibrosis of nerve constrained in microchannels. (A-B) Microscopy images of transverse sections of nerve regenerated through a 100 μm wide microchannel. (Courtesy of Dr. Katherine Musick) (C) Immunodetection of macrophage and myelin distribution inside a microchannel. Scale bars=10 μm.)

compatibility of an implant. Evidence has shown that its physical structure, including shape, size and elasticity, has an impact on the tissue response [4]. A striking example is the benefit obtained by the reduction of the cross-sectional area of electrodes thanks to microfabrication techniques, which was shown to reduce the tissue reaction [20]. The design of specific types of neural interface should take into account the mechanical constraints imposed. Cuff electrodes, and especially the flat interface electrode (FINE) design, exert compression force on the nerve. Fibrotic tissue is deposited inside and outside of the cuff, with potential demyelination of some axons (Fig.4.4c-f) [143, 142]. Intrafascicular electrodes are encapsulated in connective tissue with thickness depending on material and shape of the electrode (Fig.4.4g-h). Loss of neurons in the vicinity of the electrode is observed [147].

Regenerative electrodes may constrict the nerve fibers growing into the holes or channels because of abundant deposition of connective tissue on the inside [13]. Figure 4.5 depicts such phenomenon, occurring after the regeneration of nerve through a PDMS microchannel device. The evolution of tissue composition between 3 and 9 months demonstrate massive augmentation in collagen deposition and reduction of the axonal area. This illustrates well the challenge of regenerative interface: ideally, the axonal processes should be supported by a scaffold until a certain time point in order to accelerate the growth towards the distal side, but after a certain time they should be allowed to enlarge to their previous size [134].

A critical parameter which has recently attracted much attention is the elasticity or rigidity of the implant material, characterized by its Young's modulus. Neural tissues are among the softest in the human body. Reported values of elastic modulus range between 0.2 to 1 kPa for brain [76, 80] and 0.45 MPa for peripheral nerves [81]. On the other hand, electrodes used for interfaces are fabricated with hard materials such as silicon or platinum, which exhibit moduli that are above 10 GPa. More than 6 orders of magnitude separate those materials in term of stiffness. This mechanical mismatch created at the tissue-

implant interface may lead to cellular reactions that aggravates the FBR and the fibrotic encapsulation [148]. The field of cell biomechanics has recently shed light on the extreme sensitivity of cells to the mechanical properties of their environment [71]. Recent studies have demonstrated a direct link between substrate stiffness and activation of astrocytes and microglia in vitro and in vivo [63, 77]. In Chapter 3, the sensitivity of DRG glial cells and neurons to the micropillar mechanical cues induced changes in cell density and morphology.

Movements at the tissue-implant interface is an extrinsic factor which is correlated to the stiffness mismatch of materials. Evidences have shown that micro-motion can trigger enhanced chronic inflammatory response in CNS micro-electrode implants, leading to glial scarring and encapsulation, ultimately resulting in failure of the device [17]. Likewise, it has been suggested that the location of a peripheral nerve cuff implant in a flexion zone might cause deleterious responses [149].

# 4.1.3 Current strategies for neural implants

Several strategies are currently under investigation to overcome the problem of electrode-associated inflammation and long-term stability of devices. These include miniaturization of devices, reduction of implant stiffness, creation of anti-inflammatory surfaces, and impregnation of surfaces with trophic and adhesion factors [6, 150]. Targeted parameters specific to the case of regenerative electrodes include axonal regeneration rate, collagen deposition inside channels and functional recovery of severed nerves [16, 6].

A general strategy to improve the efficacy of these devices is to reduce the fibrotic encapsulation or encourage growth of the neurons towards the electrodes. Apart from design and miniaturization of the electrodes, surface coating of the electrode is a widely studied approach [140]. Coating with polyethylene glycol (PEG) has been shown to reduce the adsorption of protein at the surface, subsequently hindering adhesion of cells [151]. Other coatings subjected to investigation include hyaluronic acid, polysaccharides, hydrogels, and conducting polymers [150].

Drug-eluting coatings releasing anti-inflammatory agents might attenuate the reactive gliosis and fibrous capsule formation. Dexamethasone and  $\alpha$ -melanocyte stimulating hormone ( $\alpha$ -MSH) released from nitrocellulose coatings reduced reactive astrocyte numbers and proinflammatory cytokine production [152, 153]. However, a potential question with these drug-releasing methods concerns the effectiveness of the coating on the long-term, as the time course of the tissue response can span months to years.

Alternative strategies seek to modulate physical characteristics of implants, like mechanical compliance or topography. Replacing conventional stiff materials used for neural electrodes, like silicon, by compliant polymers with lower Young's modulus has already shown efficacy [4]. Polyimide and parylene, which are used to fabricate neural implants, have moduli between 2.5-2.8 GPa. It already represents an important reduction of stiffness compared to silicon, with its modulus above 100 GPa. The modulus of PDMS is variable and typically reaches 2 MPa, which is about three order of magnitude softer than the aforementioned polymers. Fabrication of a regenerative peripheral nerve interface made out of microchannels in PDMS has been demonstrated [154]. A soft subdural neural implant with elasticity matching the dura mater has shown reduced inflammatory response compared to stiffer implants [107]. The diminution of the mechanical mismatch between the tissue and the interface might result in decreased micro-motions, which are thought to sustain the chronic inflammation around stiffer implants. In that respect, the capacity of elastomeric material such as PDMS to deform and conform to 3D structures of the nervous system may constitute a significant advantage for the long-term performance of neural implants.

Finally, topographical modifications of the surface are envisioned to encourage neural cells growth towards electrodes. Topographical texture on the micro- or nanometer scale can act as guidance cues for neurons, which could be used to direct axons to implanted electrodes. Aligned nanofibers were shown to preferentially orient neuronal processes over random fibers in vitro and in vivo [91, 155]. A similar strategy used aligned nanofibers sheets with embedded microelectrodes in their vicinity to promote the growth of axons towards the electrode sites [156]. Other axonal guidance elements showing promise include biomolecules such as ECM components, adhesion proteins and neurotrophic growth factors [157]. These elements are already employed in peripheral nerve regeneration strategies, and thus they may prove particularly effective for the stability of implanted regenerative interfaces.

# Material and Methods

# 4.2.1 Creation of micropillar-textured nerve conduits

Two types of nerve conduit designs were created (Fig.4.6). The first design consisted of a simple tube with the inner surface covered with micropillars. A tube with a flat inner surface was used as a control condition. The second design consisted in a tube with a planar membrane separating the inner luminal space in two longitudinal halves. One of the halves is covered with pillars and the other is left flat, to serve as a control. The two designs are referred to as the 'simple tube' and 'theta tube' designs.

The micropillars patterned on the inner tube surface are simple arrays with pillar of the same aspect ratio (AR). The central membrane were patterned with the 'Stripes' design, presenting micropillars with 2 different AR due to grooves on the bottom surface. The dimensions of the micropillar arrays presented on the different surfaces of the tubes are reported in Table 4.1. The flat side of the membrane was patterned with the grooves only.

Table 4.1 – Dimensions of the micropillars patterned on nerve tubes. The Membrane short and tall arrays refer to pillars from the stripe design patterned on the central membrane of the Theta tubes.

Array location:	Inner Tube	Membrane (short)	Membrane (tall)
Diameter [μm]	1.2	1.6	1.6
<b>Height</b> $[\mu m]$	4.1	4.0	8.6
$\mathbf{Spacing} \; [\mu \mathrm{m}]$	1.9	2.1	2.1
Effective modulus [kPa]	10.3	26.4	2.7

#### Fabrication process

The dimensions of the tubes were designed to fit a the sciatic nerve of adult rats. The inner diameter was between 1.8-1.95 mm, with an outer diameter of 3 mm. The tubes were casted into cylindrical shape by injection molding, as represented on Fig.4.7. Sacrificial molds were formed by a teflon tube for the outer mold and a polystyrene rod for the inside mold. The micropillars were patterned on the inner surfaces of the tube thanks to a thin

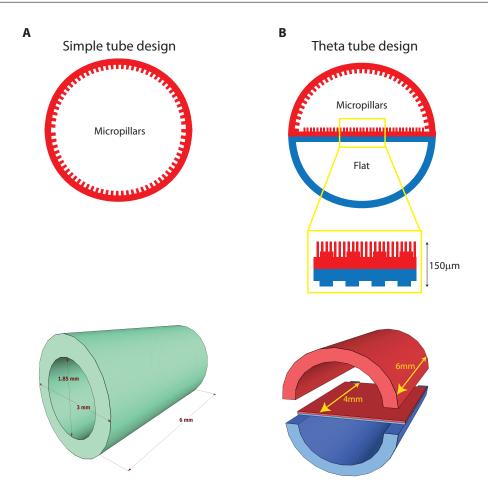


Figure 4.6 – Schematic of the 2 tube designs and dimensions. (A) Simple tube cross-sectional and 3D views. The tube length is 6 mm and walls thickness between 500-700 µm. The inner diameter varied from 1.8 to 1.95 mm. (B) Theta tube cross-sectional and 3D views. The yellow rectangle outline a close-up view of the central membrane. Theta tubes had the same dimensions as for simple tubes. The central membrane was 4 mm long.

negative mold membrane wrapped around the central rod, with micropits facing outwards. The negative mold membranes were fabricated by spin-coating uncured PDMS on a Si wafer presenting positive micropillars structures. The wafers were spun at 550rpm for 1 min, and PDMS was cured at 80 °C for at least 30 min. Once peeled off from the Si wafer, the negative mold membranes were cut to the appropriate dimensions, fitting the perimeter of the polystyrene rod. With a thickness of approximately 150 µm, the membranes allowed enough deformation to be wrapped around the 1.2 mm diameter polystyrene rods. The negative mold membranes were glued around the rods thanks to a thin layer of double-sided adhesive tape. Figure 4.7 present the mold assembly with the different layers visible in cross-section. For the control condition with flat inner surfaces, portions void from microstructures were cut out of the spin-coated PDMS membranes. The tubes were then prepared in the exact same way as for the micropillar-patterned membranes.

The rods with glued membranes were placed inside the teflon tubes and maintained in the

center with dedicated spacers. Uncured PDMS (1:10 ratio) was injected inside the teflon tube from one extremity, until the PDMS filled the entire mold, overflowing on the other side of the teflon tube. After degassing for 30 min, the filled molds were placed at 80 °C for curing (16±2 hours), taking care to maintain the tubes in upright position. After curing, the PDMS tubes were released from outer mold by cutting the teflon tubes in pieces and peeling off from the PDMS. Care should be taken here to avoid damaging the PDMS tube while cutting the teflon. Next, the inner mold assembly composed of the polystyrene rod, adhesive tape and PDMS negative mold membrane were removed from the inside of the tubes. For this, the polystyrene rod is first partly dissolved by sonication in acetone for 30 min. The rods could then easily be pulled out from the PDMS tubes. At this point, the negative mold membranes remained attached to the inner surface of the tubes. They were gently peeled off by twisting the membranes with a forceps inside of the tube, while keeping in isopropanol (IPA) to avoid collapsing of the micropillars.

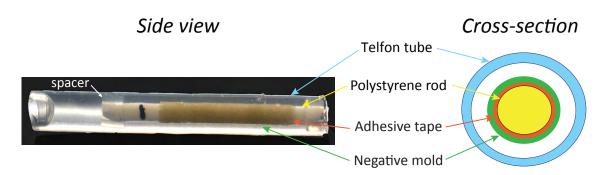


Figure 4.7 – Assembled mold for the injection molding of PDMS nerve tubes. The side view is from a photograph of the assembled mold after curing. PDMS is injected at the extremity of the tube on the left, until overflowing from the right extremity. The negative mold is barely visible here, due to matching refractive index with the surrounding cured PDMS. The cross-section view is a schematic representing the different layers of the mold assembly. The white portion is the void space where uncured PDMS is injected.

The tubes extremities were then trimmed to reach the desired length of 6 mm. The tubes were dried in a critical point drier (Leica CPD300) and sterilized for 20 min in a UV-chamber before implantation. In one of the experimental groups, the simple tubes were coated with Laminin (sigma) after sterilization. A sterile laminin solution at 20 µg ml<sup>-1</sup> filled the lumen of the tubes and was let to incubate for 3 hours at 37 °C. As a side note, the laminin solution was added in excess into the tubes, and thus the exterior of the tubes might have been partly coated as well. The tubes were then washed and stored in sterile PBS, until implantation.

#### Theta design

Some extra steps were required for the fabrication of the theta tubes. First, central planar membranes had to be fabricated. They comprise one side with a "Stripe design" micropillar array, and one control side without micropillars, displaying only the stripes topography. For this, uncured PDMS was spin-coated at 650rpm on a Si wafer patterned with 5 µm tall, 20 µm-spaced trenches. Once cured, the PDMS membranes were left in place on the wafer. Negative mold stamps with the Stripe design micropillars were inked with uncured PDMS and placed face-down, on top of the spin-coated PDMS membrane. At this point, the stripes patterns from both sides of the membranes have to be carefully aligned. After an additional curing step in the oven, the membranes were peeled from both the stamp and the wafer. The final membranes were 150 µm thick, with patterns on both sides.

PDMS tubes with and without micropillars were produced following the same protocol as for the simple tubes. After drying in air, the tubes were cut in half along their longitudinal axis. The central membranes were then glued between a half-tube with micropillars and half-tube with flat surface. Medical grade silicone glue (Kwik-seal, Dow Corning) was used to ensure biocompatibility. Care should be taken here to assemble the half tubes on the corresponding sides of the central membrane.

The assembled theta tubes are left overnight to cure to ensure complete sealing of the silicone glue. They were immersed in IPA and sonicated in the sonicator bath for 10 min, in order to restore collapsed pillars in upright position and clean the tubes from particles. The aspect of the micropillars was closely monitored here, and additional sonication in ethanol was performed when needed. Finally, as for simple tubes, the theta tubes were dried in the critical point drier and sterilized with UV before implantation.

#### 4.2.2 In vivo implantation

The regeneration of nervous tissue through the nerve conduits was evaluated on the sciatic nerves of adult male Lewis rats (200-250 g). All the procedures involving animals were conducted in accordance with animal experimentation licence established by institutional veterinary authorities from Canton de Vaud. The surgical implantations of conduits were carried out by Dr. Pietro di Summa (Department of Plastic and Reconstructive Surgery, CHUV). The rats were anesthetized by inhalation of isoflurane (2-5%) and maintained under 1-2% isoflurane during the surgery. The fur of rats above the sciatic nerve was shaved and the skin disinfected with betadine and ethanol. The sciatic nerves on the left-hand side of the rats were surgically transected above the bifurcation of the tibial

and peroneal nerves. The proximal and distal nerve stumps were placed approximately 1 mm into both extremities of the PDMS tubes and held in place with 1 or 2 suture points (Prolene 9-0, Ethicon). The muscle tissues were sutured with absorbable filament (Monosyn 3-0, Braun Medical) and the skin incision was sutured with Prolene 3-0 filament (Ethicon). After the surgery, the rats were left to recover in a chamber kept at constant humidity (40%) and temperature (20°C) until waking up. Postoperative medication of the rats consisted in antibiotic treatment for 5-7 days (1 ml Amoxicillin diluted in 100 ml water) and buprenorphine subcutaneous injections for 2-3 days (0.1 ml Buprenex, 2 times per day). The rats were housed in cages (2-3 rats per cage) with food and water access ad libitum, and 12/12h cycle of light/dark. The rats were monitored every day for clinical and behaviorial signs. In case of weight loss superior to 10% of body mass, supplementary nutritious mixture was added to the food.

**Table 4.2** – **In vivo experimental groups.** This table recapitulates the different conditions and time points for in vivo the experiments with the 2 tube designs.

Tube	No of animals	Time point	Surface
Simple	3	12 weeks	Micropillars
Simple	3	12 weeks	Flat
Simple	3	12 weeks	Micropillars + LN
Theta	3	2 weeks	Micropillars
Theta	3	4 weeks	Micropillars
Theta	3	12 weeks	Micropillars

## 4.2.3 Tissue fixation and sectioning

Nerve regeneration was evaluated at different time points depending on the experiment (48 hours, 2 weeks, 4 weeks and 12 weeks). On the day of tissue explantation, rats were sacrificed by intraperitoneal injection of pentobarbital (30-50 mg/rat). Once terminal anesthesia was confirmed by toe pinching, the sciatic nerves were excised proximally and distally from the PDMS conduit, leaving at least 1 mm long nerve stumps attached to the implant on both sides. The explants were immediately fixed in 4% PFA (pH 7.4) and stored at  $4^{\circ}$ C for at least 24 h. The explants were then washed with PBS 2-3 times and transferred to a solution of 30% w/v sucrose in PBS for cryoprotection. The explants were maintained in sucrose at  $4^{\circ}$ C for at least 48 h. After sucrose cryoprotection, the explants were put in a small container and flooded with liquid embedding matrix for cryostat sectioning (O.C.T., Tissue-Tek). The OCT-mounted explants were frozen by floating the containers in dry ice-EtOH or isopentane slurry, and stored at  $-20^{\circ}$ C until further processing.

Blocks containing the explants were mounted on a cryostat (CM30505, Leica) at -23 °C, sectioned and mounted on microscope slides (SuperFrost, Menzel Gläzer). The thickness of the tissue sections was either  $100 \, \mu m$  or  $200 \, \mu m$  for slices containing portion of PDMS tubes. Slide-mounted sections were stored at -20 °C until further processing.

# 4.2.4 Determination of muscle weight

The atrophy of Gastrocnemius et Tibialis anterior muscles was quantified by determining their weight and comparing to the weight of the contralateral muscles. This was done for experiments involving simple tubes, in order to evaluate the difference between micropillars and flat condition. The Gastrocnemius and Tibialis from ipsilateral and contralateral sides were explanted at the same time as the PDMS tubes. The mass of the muscles was determined with a scale immediately after explantation.

# 4.2.5 Immunohistochemical staining and imaging

Sections were stained with different markers to label specific component of the regenerated nervous tissue. Table 4.3 lists the antibodies used for the immunohistological staining. Before staining, cryo-stored slide-mounted sections were thawed at RT for 20 min. For thick sections containing PDMS tube portions, a thin piece of nylon mesh was glued on top of the tissue/PDMS to prevent the detachment of the PDMS and tissue from the microscope slide. However, care should be taken to avoid the trapping of bubbles between the nylon mesh and the slide. PBS was injected with a needle between the mesh and the slide to dislodge the air bubbles. The slides were washed thoroughly in PBS for at least 30 min and blocked from unspecific antibody attachment by incubation for at least 1 h in blocking buffer consisting of: 1% BSA, 2% normal goat serum, 0.5% Triton-X in PBS (pH 7.4). The primary antibodies were diluted in blocking buffer at indicated dilutions and 200 µl of solution was added to each section (2 sections per slides generally). The slides were incubated for at least 16 h at 4 °C, with humidified paper to avoid drying. After this, the slides were washed 3 times in PBS-Tween (0.05% Tween) for at least 5 min. The fluorescent secondary antibodies were diluted in the blocking buffer and added to the slides for at least 1 h of incubation at RT in the dark. The slides were then washed as previously with PBS-Tween. A solution of 10 µM DAPI in PBS was added to the slides for 30 min in order to stain cell nuclei. Finally, the slides were washed once again with PBS and the nylon mesh was removed from the sections. Excessive liquid was removed from the slides and 1-2 drops of ProLong Gold antifade mounting medium (Life Technologies) was added on the sections, which were covered with thin glass coverslips (Menzel Gläser, thickness

no1) and sealed with nail polish. Stained slides were stored at 4°C.

The stained sections were imaged with a confocal microscope (Zeiss LSM700) at different magnifications. In order to image large nerve sections, tile scan images were acquired and stitched with the dedicated microscope software (Zeiss ZEN). For certain sections, stacks of images in the Z-plane were acquired to compensate for out-of-plane portion of the tissue. The images were then rendered as maximum Z-projection.

Table 4.3 –	List of	antibodies	and	stains	used	for	in	vivo	experimen	ıts.

Antibody	Dilution	Target	Manufacturer
Tuj-1	1/100	Neurons and neurites	Abcam (78078)
MBP	1/100	Myelin	Abcam (ab 40 390)
ED-1	1/250	Macrophages	Serotec (MCA341GA)
CD206	1/200	M2 Macrophages	Abcam (ab64693)

# 4.2.6 Quantification of tissue cross-sectional area

The area of nerve tissue inside simple and theta PDMS tubes was quantified from the cross-sections obtained after cryo-sectioning of the fixed tissues samples. The slides were brought to room temperature and imaged with conventional transillumination widefield microscopy. The tissue sections were manually traced and the area calculated using imageJ. For sections with internal artifacts, the segmented images were thresholded in order to eliminate void spaces from the area calculations. For the simple tubes, the areas were reported as function of their position along the longitudinal axis of the tube. The minimal sizes of the regenerated tissue cable inside of the tubes was determined for each condition. For simple tubes, the 5-6 sections with the lowest areas were averaged for each sample. For the theta tube, a single section was used. For both tubes type, the mean minimal area per condition was calculated from the average of 3 animals.

# 4.2.7 Quantification of axonal regeneration

Sections of regenerated tissue were immunostained for the neuron-specific tubulin Tuj-1 and for Myelin Basic Protein (MBP). The axonal regeneration was quantified by calculating the Tuj-1 positive area in whole sections. For this, the Tuj-1 image was thresholded to appropriate level with ImageJ, and the segmented area calculated with the 'Analyse particle' plugin. The percentage of axonal area in the sections was computed by taking the ratio between Tuj-1 positive area and the total area of the section. This latter was quantified thanks to the MBP image. MBP stained weakly for unspecific regions, allowing to image the integrality of the section upon histogram adjustment. As for Tuj-1, the MBP images

were thresholded in order to segment the tissue signal from the background, and the area was calculated with the "Analyse particle" plugin. The axonal area and the ratio were averaged from 2 sections for each animal. The data were then expressed as the mean from 3 animals.

# 4.2.8 Quantification of fluorescence intensity

In order to compare the distribution of cells, macrophages and M2 macrophages, the fluorescence intensity was measured on a longitudinal section of the theta tube stained for ED-1, CD206 and DAPI. 2 rectangular zones were traced to include the tissue cables from the micropillar and flat sides, delimited by the central membrane. The 'Plot profile' plugin of imageJ was then used to compute the mean fluorescence intensity profile across the cable. With this plugin, each line inside of the delimited zone is measured for pixel intensities, and all profiles are averaged to yield the mean intensity profile.

# 4.2.9 Statistical analysis

Statistical analyses were performed with the same protocol described in Section 3.2.13 from Chapter 3. Briefly, one-way analysis of variance (ANOVA) with Tukey's post-hoc test was performed for distribution with the same variance. Kruskal—Wallis ANOVA rank test and Mann—Whitney U test adjusted with the Bonferroni method were performed for unequal variances. Computations were performed with the software OriginPro.

# Results

#### 4.3.1 Fabrication of nerve conduits

Micropillars were successfully patterned on the curved inner surfaces of PDMS tubes with diameter on the millimeter range (Fig.4.8). However, the deformation of the negative mold however did not induce modification of the micropillar morphology. The geometrical dimensions of the micropillars were chosen to produce an effective stiffness of 10 kPa on the inner surfaces of the tube. This is in the intermediate range of stiffness explored in the in vitro experiments. The reproducibility and fidelity of pillars with this aspect ratio (AR) is also well controlled, compared to more fragile higher AR pillars.

After the initial fabrication of simple cylindrical tubes, a new design was created, which incorporated a central membrane inside of the tube. The theta design divides the lumen in two spaces, one with patterned micropillars and one with flat PDMS surface. It enables to probe the nerve regeneration simultaneously for the 2 conditions and increases the contact surface with the PDMS surfaces. The central membrane is 4 mm long, and positioned at the center of the 6 mm long tube. For both the simple and theta tubes, the nerve stumps are to be inserted 1 mm into the tube at the extremities, giving an effective distance of 4 mm for the regeneration of the nerve.

The central membranes were patterned with the Stripe micropillar design (cf. Chapter 2), with the 20 µm-wide grooves oriented parallel to the longitudinal axis of the tube. To create a control on the flat side, the membranes were patterned with grooved structures of the same size, but without micropillars. Anticipating the nerve tissue would regrowth along the central membrane, the presence of aligned grooves on the surface was meant to serve as a guiding element for the axons.

The main flaws of the tube observed after fabrication were a slight variability in PDMS wall thickness, due to unperfect centering inside the outer mold, and the presence of a small artifact on the inside surface of some of the tube. The latter is due to misalignment of the negative mold membrane glued in the rods. None of these flaws were found to be

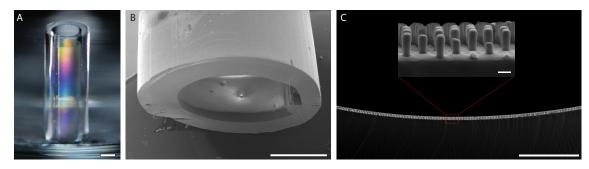


Figure 4.8 – Fabrication of simple tubes. (A) Photography of a tube in ethanol after release from the mold. The diffracted light inside the tube indicates a regular micropillar texture. (B) SEM image of the extremity of a tube. (C) SEM image of the inner surface of a tube, showing micropillar interface. The inset shows high magnification of the portion delimited in the red rectangle. Scale bars:(A-B)=1 mm, (C)=100  $\mu$ m, Inset=2  $\mu$ m.

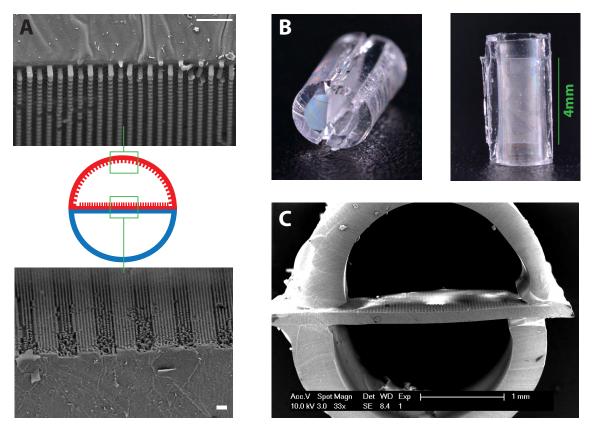


Figure 4.9 – Illustrations of a Theta tube before implantation. (A) SEM images of the tube walls and central membrane, showing the micropillar textures. Scale bars= $10 \,\mu\text{m}$ . (B) Photographs of a Theta tube. The 4 mm long central membrane is visible in the center of the tube. (C) SEM image of the cross-section of a Theta tube.

critical for assessing the nerve regeneration.

## 4.3.2 Implantation of conduits on transected rat sciatic nerves

All conduits were successfully implanted and sutured to the stumps of transected rat sciatic nerves. The inner diameter of the tubes was large enough to insert the nerve stumps inside of the tube extremities (Fig. 4.10). An insertion of 1 mm from the extremities of the tube was targeted, but small variations in the insertion distance were observed, with stumps placed  $\pm 500 \,\mu m$  from their intended position.

With one exception (the 48h time point), all rats recovered well from the surgery and were able to reach the endpoint of the experiment. The rats recovered mobility after a few days, walking mainly with 3 limbs. One rat had to be sacrificed after 2 days, due to an infection of the skin wound. However, the implant was used to assess the early response of cells to the micropillars.

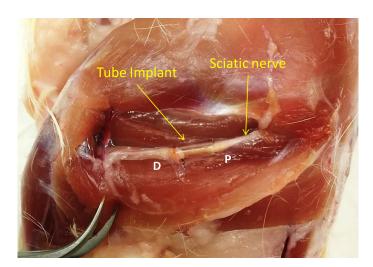


Figure 4.10 – Photography of the surgical implantation of a nerve conduit. This picture was taken during the explantation of the tubes, 12 weeks after implantation. The transected nerve is sutured to the extremities of the tube, with nerve stumps fixed approximately 1 mm into the tube. The D and P letters on the image indicate the distal and proximal directions from the implant.

#### 4.3.3 Nerve regeneration through simple conduits

Three conditions were probed for the regeneration through simple tubes: micropillars, flat surfaces and micropillars with a laminin coating. Three rats per conditions were used and all rats were sacrificed 12 weeks post-implantation. The tubes implants were collected on fresh tissues just after the sacrifice, as opposed to perfusion with PFA. It facilitated the access to the explant through the leg muscles. The explants were then fixed for at least 24h in 4% PFA.

The outcome of nerve regeneration was first observed with photographic means and optical microscopy. Figure 4.11 A-B shows the typical pattern of regeneration: A thin cable of tissue crosses the tube from the proximal to the distal sides. The tissue cable was found either free standing at the center of the tube, or partly in contact with the wall of the tube on one side. The integrity of the micropillar interface could be observed here with brightfield microscopy. The image D from Figure 4.11 shows the boundary between tube surface and inner lumen. Dense micropillar arrays are discernible at the surface of PDMS.

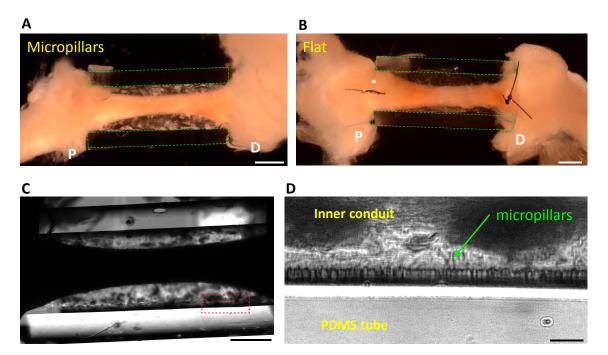


Figure 4.11 – Nerve tissue explants fixed 12 weeks after implantation. (A-B) Photography of micropillar-patterned and flat tubes with regenerated nerve inside, after 24h of fixation in PFA. The green rectangles outline the boundaries of the PDMS tubes. P and D indicate proximal en distal directions. (C) Image reconstructed from stitched brightfield microscopy images of an explant regenerated through a micropillar tube. The red rectangle shows the position of the higher-magnification image on (D). Micropillars are visible on the surface of the PDMS tube. Scale bars: (A-B-C)=1 mm, (D)=10  $\mu m$ .

After cryopreservation in sucrose, all the explants were mounted in OCT and cut into cross-sections at  $-20\,^{\circ}$ C. The presence of the PDMS tube posed significant difficulties for the realisation of thin sections. With its glass transition temperature near  $-125\,^{\circ}$ C, PDMS keeps an elastic behaviour when cutting the explant with the cryostat. Thus, as the blade comes in contact with PDMS, the tube deforms slightly before being actually sliced. The mismatch between the biological tissue and PDMS mechanical behaviour at  $-20\,^{\circ}$ C generally translated into the tearing apart of the PDMS-tissue interfaces, and eventually the loss of the entire slice. Sections with conventional thickness for histology (i.e. around  $10\,\mu\text{m}$ ) were not realisable, but increasing the thickness to  $100\text{-}200\,\mu\text{m}$  allowed to obtain some relatively intact sections. The consequences of this technical limitation were multiple: The position of the tissue relative to the tube was often flawed due to

separation of the component upon cutting. Thick sections are more difficult to stain due to limited penetration of the solution into tissue. Imaging quality is degraded by background fluorescence and conventional histological stains such as Masson's Trichrome are not usable. Moreover, at  $100\,\mu\text{m}$ , the number of available sections is limited and their localisation in the tube less precise. Nevertheless, several exploitable sections were obtained for each explant and the immunostaining successfully detected specific targets in the regenerated tissues.

#### 4.3.4 Quantification of tissue area in conduits

The extent of tissue regeneration inside the conduits was characterized by measuring the tissue area for each section along the tubes. For this, the sections mounted on histological slides were imaged with brightfield microscopy, and their perimeters were manually delimited and measured with imageJ (Fig.4.12A). The areas of sections were reported as function of their position inside the tube. The position of sections, deduced from the sequence and thickness of slices at the moment of cryostat sectioning, are accurate to approximately  $\pm 100\,\mu m$ . Each of the 3 implants per condition are reported on the graph B from Fig.4.12. Important differences can be observed between individual lines. Some of these differences originate from the variation in the exact positioning of the nerve at the time of the implantation, with stumps sutured closer or further than 1 mm from the tube extremity.

The minimal size of the regenerated cable was inspected for the 3 conditions. For this, the 5-6 smallest sections in each set were averaged. The minimal section areas were reported as the average of 3 animals on the bar graphs C on Fig.4.12. A clear effect of the laminin coating on the size of regenerated tissue was observed, with significant difference from the uncoated micropillars. The minimal area was almost doubled for the laminin coated micropillars, as compared to uncoated micropillars. The great variability observed for the flat condition prevented significant differences to be established.

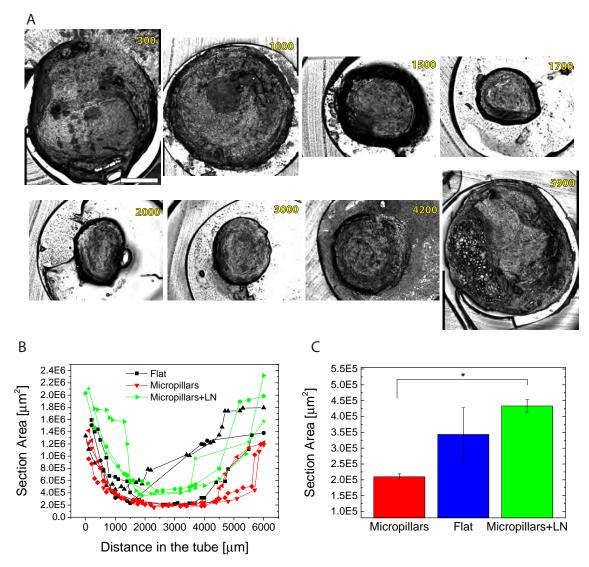


Figure 4.12 – Quantification of tissue regeneration through PDMS nerve tube. (A) Micrographs of the cross-sections of regenerated nerve tissue, obtained after cryo-sectioning. The PDMS tube is visible on the periphery of the images, and the respective position is indicated on the upper right corner. The 0 and 6000 positions correspond to the proximal and distal sides of the tube, respectively. Scale bar =  $500\,\mu\text{m}$ . (B) Graphs of the surface area of tissue as function of the position in the tube for the different conditions. Each curve represent an individual animal. (C). Bar graph of the tissue cable cross-sectional area at its smallest value for each condition, averaged on 3 animals. Significance level: \*P < 0.05.

#### 4.3.5 Leg muscles weight measurements

As a functional measure of regeneration, the atrophy of muscles innerved by the sciatic nerve was quantified. The Gastrocnemius and Tibialis anterior are 2 muscles implicated in the movement of the lower leg, and which experience severe deprivation of stimuli upon sciatic nerve transection. These muscles were isolated during the harvesting of the implants and immediately weighted for both ipsilateral (left leg) and contralateral (right leg) sides (Fig.4.13 A). Only the two conditions uncoated micropillars and flat benefited from this

characterization.

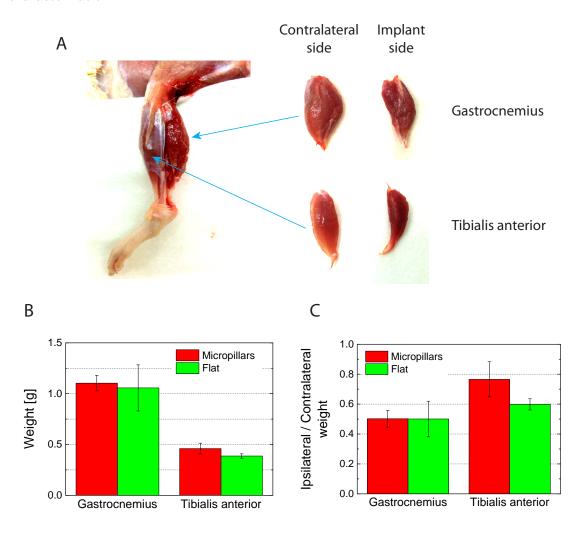


Figure 4.13 – Leg muscular mass after sciatic nerve regeneration through PDMS conduits. (A) Photograph of the leg of the rat exposing the Gastrocnemius and Tibialis anterior muscles from the ipsi- and contralateral sides. Graphs of the mean muscle weight (B) and ipsi- to contralateral weight ratios (C). (3 animals per condition).

The net weight of both muscles were very similar for the flat and micropillar conditions (Fig.4.13 B). Likewise, the ratio between the ipsi- and contralateral muscles remained very close for both conditions (Fig.4.13 C). As observed from these measurements, the quality of the functional regeneration was nearly identical for flat and micropillars-textured conduits.

#### 4.3.6 Nerve regeneration through theta conduit

Theta tubes were implanted on rat sciatic nerves following the same protocol used for simple tubes. With the presence of both micropillar and flat surfaces, the 2 conditions can be simultaneously compared. In order to observe the evolution of tissue size and composition, the tubes were explanted at 3 different time points: 2 weeks, 4 weeks and 12 weeks. Once fixed in PFA, the regenerated tissue cable can be observed through explant

pictures (Fig.4.14). In most of the samples, the tissue is located in the center of the tube, engulfing the central membrane. This validates the hypothesis that the theta design increases the percentage of tissue in contact with conduit surface. In one of the samples, the tissue grew along the tube inner wall, on the micropillar side of the conduit (lower left image in Fig.4.14). This was most likely induced by the position of the sutures, which were located on the same side of the tube in this conduit. To avoid this problem, the other conduits were sutured with 2 diametrally opposed suture points for each extremity.

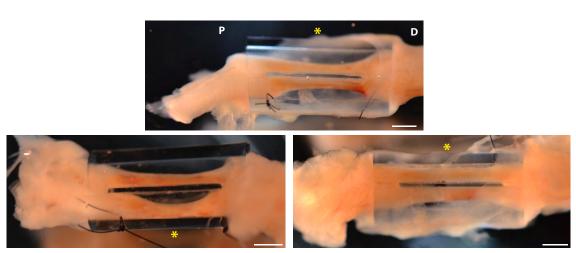


Figure 4.14 – Theta tubes explants fixed 2 weeks post-implantation. Photographs of the 3 explants from the 2-weeks time point immersed in PBS. Regenerated nerve tissue generally wrapped around the central membrane, although on one occasion it followed the inner tube surface (lower left picture). The P and D letters indicate the proximal and distal directions, and the yellow star the side of the theta tube harboring micropillars. Scale bars = 1 mm.

As for the simple tubes, the sectioning of theta conduits was greatly affected by the presence of PDMS. Thick sections were again required to obtain usable material for staining. Even at  $100\,\mu\text{m}$  of thickness, tissue most often detached from the central membrane upon cutting with the cryostat. Thus, the sections had to be analysed without being attached to the actual PDMS surfaces.

#### Quantification of tissue area in conduits

The theta tube design allows direct comparison between the micropillar and flat conditions, as each section contain both type of tissues, with the same longitudinal position in the tube. The tissue sections were measured for their area, and two types of information were plotted: The tissue cross-sectional area at the point of minimal size, and the ratio between micropillar and flat conditions in terms of area, for sections covering the entire length of the tube. We observe a slightly larger tissue area for the micropillar over the flat condition at the shortest time point. The areas are essentially equal at 4 weeks, with a small edge for

the flat condition. At 12 weeks the difference increased, with an area for micropillar which is 30% smaller than the flat one. Interestingly, the tissue area drops between 2 weeks and 4 weeks for both condition. The decrease is sensibly more important on the micropillar side, whereas the flat side stayed within the error range.

The ratio between the tissue area in micropillar and flat compartments allows a relative quantification of the difference between the 2 conditions. The ratios were here calculated for sections from all the positions inside of the tubes. We see a trend indicating a shift towards higher proportion of 'flat' tissue than 'micropillar' tissue as the time progresses. At 2 weeks, the balance is clearly in favor of the micropillar side. But the situation is reversed from 4 weeks on, with an area in the micropillar side reduced by 20 % compared to flat condition at 12 weeks.

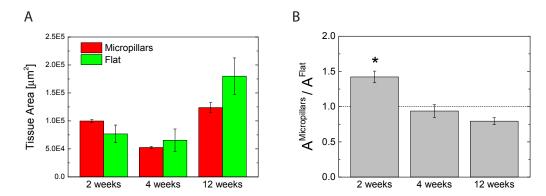


Figure 4.15 – Cross-sectional area of tissue in theta tubes. The area of the tissue cross-sections in the micropillar and flat sides were quantified at 2 weeks, 4 weeks and 12 weeks after implantation. (A) Bar graph of the minimal value of the tissue cross-sectional area. The data is averaged for 3 animals for 2 and 4 weeks, and 2 animals for 12 weeks. (B) Bar graph of the ratio between tissue area in the micropillar side and tissue area in the flat side. The data was averaged from 32, 36 and 18 sections for the 2, 4 and 12 weeks time points, respectively. Sections were taken from the entire length of the theta tubes. Error bars on both graphs represent the SEM. Significance level: \*P < 0.05.

#### 4.3.7 Axonal regeneration

The regeneration of axons through the theta conduits was assessed by immunostaining sections for Tuj-1. Sections were concomitantly stained for the myelin basic protein (MBP), which is expressed mainly by Schwann cells forming the myelin sheath. In order to observe the extent of axonal regeneration along the conduit at 12 weeks, one explant was sectioned in the longitudinal axis of the tube, perpendicularly to the central membrane. The regenerated tissue in the micropillar and flat lumens are visible on the same slide. This section is shown on Fig.4.16. The tissue was slightly deformed during the staining process, which resulted in the spreading of tissue cables apart from each other. The Tuj-1 stained image shows that axons are crossing the entire tube and reaching the distal side

for both conditions after 12 weeks of implantation. Axons were densely packed in both cases, and occupied a significant portion of the tissue cable. Despite an artifact where the fluorescence signal was decreased, myelin structures can be observed at all points along the conduit on Fig.4.16 B. Their shape was similar to the axons, forming long strings parallel to the longitudinal axis of the conduit. Finally, the density of cells is visible through DAPI staining of the nuclei, without striking differences between flat and micropillars conditions here.

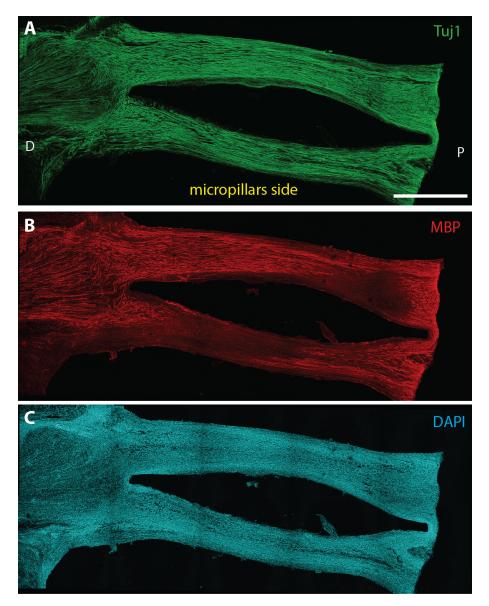


Figure 4.16 – Longitudinal section of theta tube showing axonal regeneration. The images are maximal projections of a Z-stack spanning about  $50\,\mu m$ . The section was stained for: (A) axons (Tuj-1), (B) Myelin (MBP), and (C) nuclei (DAPI). P and D indicates proximal and distal directions. Scale bar =  $1\,m m$ .

The extent of axonal regeneration was quantified on cross-sections of the explants situated in the distal half of the conduits. The total area of axons, i.e. the Tuj-1-positive area, was measured with imageJ and reported for the 3 time points (Fig.4.17 A). The profile

of axonal growth was different between the flat and micropillar conditions. For the flat, the axonal area increased relatively linearly between 2 and 12 weeks. However for the micropillars, the axonal area seemed to have reached a plateau, as no increase was observed between 4 and 12 weeks. There was minor differences in the absolute axonal area of flat and micropillar conditions at 2 and 4 weeks. However, at 12 weeks, the average axonal area of flat condition was almost twice the one of the micropillar condition.

The ratio between the axonal area and total area of the section was calculated and reported on the graph B of Fig.4.17. The total area was calculated from the MBP signal, which allowed to visualize the entire section, including the outer strand of fibrous tissue (Fig.4.17 C). The ratio provided a measure of the percentage of area taken by axons for each section. The axons took only about 7 to  $10\,\%$  of the section area at 2 weeks, but increased to  $30\text{-}35\,\%$  for the later time point 4 and 12 weeks. No significant differences were observed between the micropillar and flat conditions, with only slightly higher values for the flat.

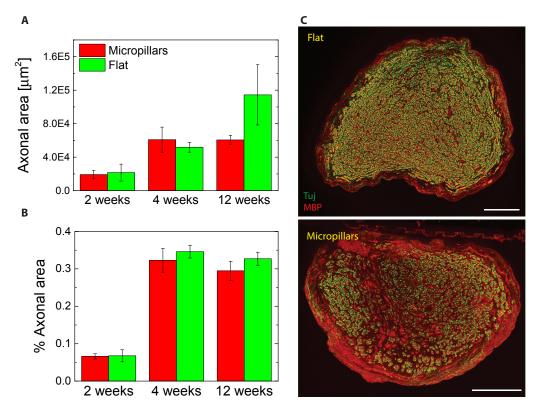


Figure 4.17 – Quantification of axonal regeneration. (A) Graph of the total axonal area (Tuj-1 positive area), and (B) graph of the percentage of axonal area per section, expressed as the ratio between Tuj-1 positive area and total area. The data represent the average of 3 animals for each condition. 2 sections located in the distal half of the tube were averaged. Error bars represent the SEM. (C) Confocal fluorescence images of representative tissue sections used for the quantification, here from the 4 weeks time point. Green is for Tuj-1 and red for MBP. Scale bar = 100 μm.

#### 4.3.8 Short term implantation

One of the conduits was removed after 48 hours of implantation, due to unresolvable wound infection. It gave the opportunity to observe the early interactions of peripheral nerve and immune cells with the PDMS conduit surfaces. In this case, the explant was not mounted in OCT for sectioning. Instead, the theta tube was disassembled by separating the 3 parts formed by the central membrane, micropillar and flat tube halves. The tissue was gently removed and the 3 PDMS parts were immuostained and inspected by confocal microscopy. The tube extremities were imaged by acquiring Z-stacks of images rendered as maximal Z-projection. The marker for activated macrophage ED-1 and the stain for actin filaments were used here to detect immune cells and cytoskeleton. Pictures of the different parts imaged with fluorescence can be found on Fig.4.18.

As observed on these pictures, a great difference in cell number exists between flat versus micropillar surfaces. The tube extremity with micropillars show densely packed cells, almost forming a monolayer. On the opposite side, the flat tube has few cells, which can be individually spotted. Most of the these cells were positive for the macrophage marker, regardless of the surface condition. Similarly, the central membrane showed markedly more cells on the micropillar side compared to the flat side. The Stripe pattern of micropillars did not seem to induce preferences of cells for a stripe configuration over another, whether it be from the mechanical or topographical difference between the stripes. However, the high density of cells here renders a quantitative description difficult.

Lastly, the actin cytoskeleton of individual cells attached to the tube walls was observed. On micropillar surfaces, the cells, especially those positive for the macrophage marker, demonstrated high content of polymerised F-actin. Interestingly, almost all of the macrophages had several actin ring patterns, engulfing the micropillars underneath them. This might have contributed a tighter adhesion of these cells to the surface. On the other hand, macrophages on the flat surface had little amount of actin cytoskeleton, mostly situated at the periphery of the cytoplasm. These cells seemed also more prone to aggregation compared to the micropillar conditions.

#### 4.3.9 Macrophages

The modulation of the immunological response by micropillar topography was inspected here in the context of peripheral nerve regeneration. For this, the sections were stained for the general macrophage marker ED-1. Additionally, the phenotype of the macrophage was assessed by staining simultaneously for the CD206 antigen, which is a marker of the M2

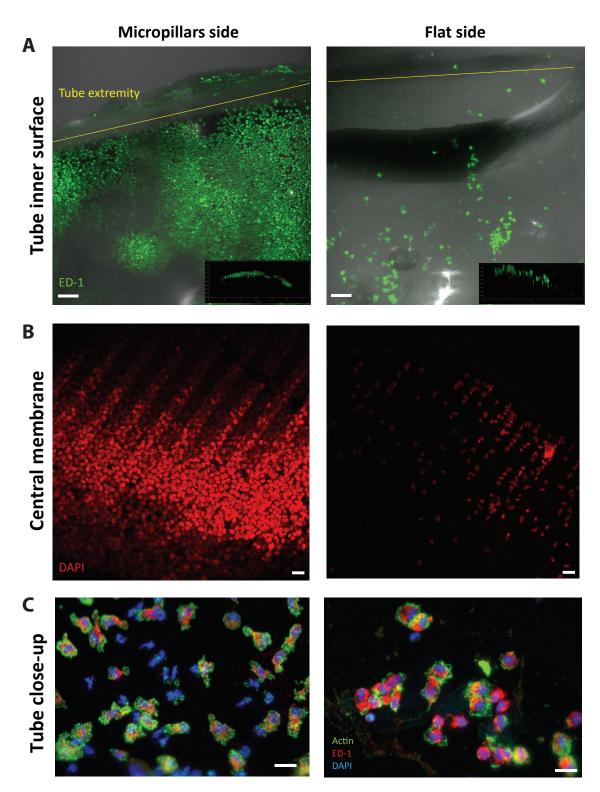


Figure 4.18 – Attachment of cells on PDMS surfaces 2 days post-implantation. Comparison of fluorescently labelled cells between micropillar and flat side. The tube extremities and central membrane on the micropillar side demonstrated higher attachment of cells, mostly expressing macrophages marker ED-1. (A) Images of tube inner surface are projection of a stack of images acquired by confocal microscopy. The insets on the lower right corners show the X-Z plane of the stack. (B) Central membranes imaged near their extremities for cell nuclei. (C) Higher magnification images of cells stained for ED-1 (red) and actin (green). The majority of the cells expressed macrophage marker. Actin cytoskeleton of cells on micropillars demonstrated actin ring formation, as previously observed for in vitro experiments. Scale bars: (A)=100  $\mu$ m, (B-C)=20  $\mu$ m.

phenotype. This latter phenotype is recognized as pro-healing, with wound-healing and tissue remodelling activities, and is opposed to the pro-inflammatory phenotype.

Due to the difficulties to preserve the tissue-material interface during the sectioning, the different components were analysed separately. Portions of PDMS tubes with attached cells remaining were imaged and are presented on Fig.4.19. The images in this figure are representative of the situation commonly observed for most explants: The surfaces covered with micropillars have much higher number of attached cells compared to those with flat surfaces. The majority of these cells stained against ED-1, but not CD206, and thus can be considered as M1 macrophages.

Due to its higher contact area with the tissue, the central membrane in particular demonstrated aggregation of cells on top of the micropillars. Observed in cross-section or from the top, we can see the micropillar side consistently covered with a layer of cells on the entire surface, whereas the flat side is mostly devoid of cells (Fig.4.19 A-C-D). The high-magnification view on image B shows the interaction of macrophages with micropillars from the central membrane, with the Stripe design. The cells are invading the integrality of the inter-pillar space, reaching the bottom surface, and bending the micropillars. However, the density of the cells prevents the observation of the behaviour of individual cells on pillars. No differences are visible between the cells on high aspect ratio pillars and small AR pillars, and thus no particular conclusion can be drawn from the differentiated mechanical and topographic effects on the 2 types of stripes. The inner walls of the tubes were commonly populated by few cells, as seen on Fig.4.19 E-F. As for the central membrane, the micropillar texture displayed higher cell content, in particular macrophages, compared to flat tube surfaces.

Similarly to axons, the distribution of macrophages in the tissue cable along the tube was observed in a longitudinal section. Macrophages with the 2 phenotypes were present at all locations, both the micropillar and flat sides of the tube (Fig.4.20 A-C). Differences in the fluorescence signal intensities and distribution can be observed between the 2 sides and were quantified (Fig.4.20 D). At the tissue periphery, the intensity of both ED-1 and CD206 was stronger on the micropillar surface compared to flat surface, as illustrated by the sharp peaks on their intensity profiles. The signal intensity on the tube side of the tissue was particularly high in this case.

The merged image (Fig.4.20 C) showed the distribution of the macrophage phenotypes in the tissue. The tissue periphery on the micropillar side was populated both by M2 and M1 phenotypes, as green and yellow signals are visible. On the tube side, the majority of ED-1 positive cells were also positive for CD206, as demonstrated by the very similar shape of

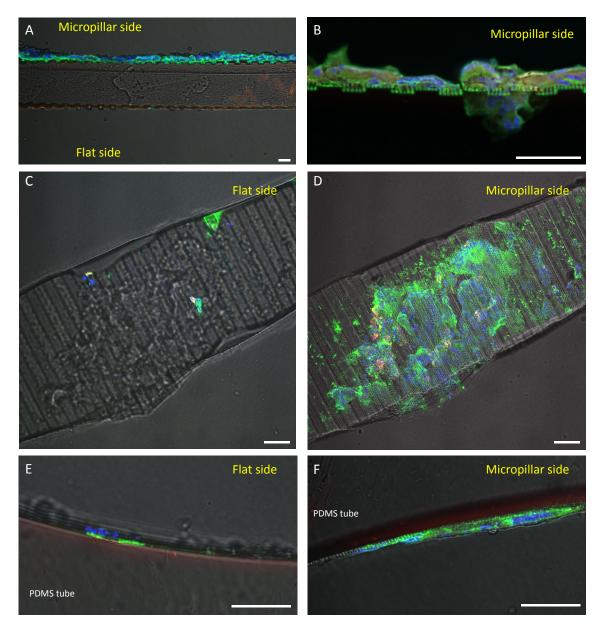


Figure 4.19 – Attachment of cells on micropillar versus flat surfaces. Fluorescence images from tissue cross-sections of a theta conduit 12 weeks after implantation. Green is for macrophages (ED-1), red for M2 macrophages (CD206), blue for cell nuclei (DAPI) and grey for transmitted light. Scale bars are 50  $\mu$ m. (A) Central membrane observed in cross-section, showing simultaneously the flat and micropillar sides. (B) High magnification view of the micropillar side, with cells aggregating on micropillars. (C-D) Portion of a central membrane from a 200  $\mu$ m thick section, observed from the top. Flat and micropillar sides were focussed separately with a confocal microscope. (E-F) Representative images of the inner tube wall surfaces, observed in cross-section.

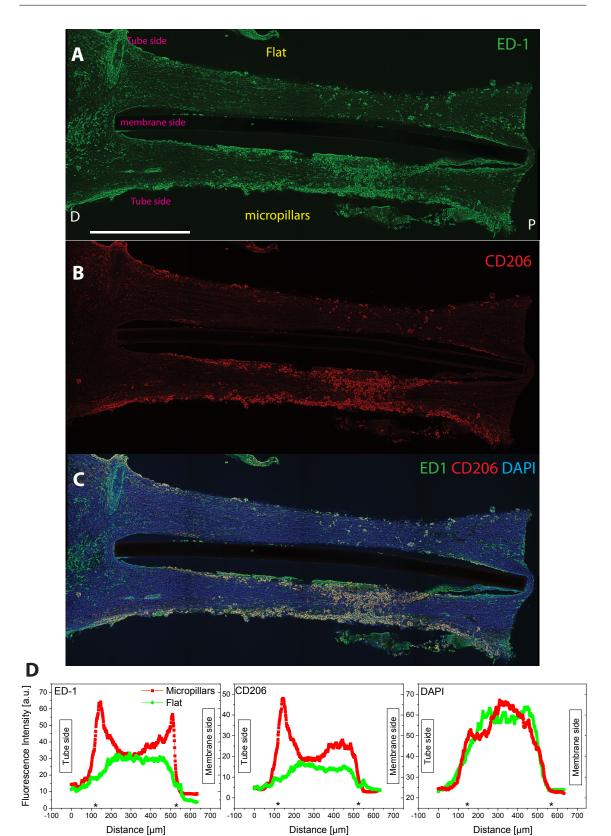


Figure 4.20 – Longitudinal section of theta tube showing macrophage distribution 12 weeks post-implantation. The section was stained for: (A) all macrophages (ED-1) and (B) M2 macrophage (CD206) and (C) DAPI. P and D indicates proximal and distal directions. Scale bar = 1 mm. (D) Fluorescence intensity profile of the markers for the tissue cables in the micropillar (red curves) and flat (green curves) lumen. Curves represent the average intensity of 3 mm of tissue, centered at the mid point of the tube. Stars on the x-axis indicate the approximate borders of the tissue.

the intensity profile for both markers. On the membrane side, ED-1 showed a strong peak, which was not present on the CD206 profile. This suggested that an unbalance in favor of the M1 macrophage phenotype was present in the vicinity of the membrane, where tissue is in contact with the micropillars. Not particular differences were observed between ED-1 and CD206 profiles for the flat surface.

The signal of all markers at the center of the tissue was similar between micropillars and flat conditions. Thus, it was mostly the periphery of the tissue which was affected by the reaction of immune cells to the surface topography, whereas the interior of the tissue remained similar for both flat and micropillar surfaces.

The morphology and phenotype of macrophages were examined at the border of tissue sections. High magnification views of tissue near the central membrane are provided on Fig.4.21. Consistent with previous results, the periphery of the tissue displays higher densities of macrophages when the surface is textured with micropillars. The number of cells in general is visibly higher as well, as seen from the DAPI staining. The orientation of nuclei and cytoplasm seems perpendicular to the surface, thus allowing the cells to form densely packed regions at the interface. The phenotype of macrophage differed somehow from what was observed previously in the longitudinal section. On the micropillar side, few M2 macrophages were observed near the periphery, but the majority of cells stained only for ED-1. Oppositely, on the flat side, few macrophages stained for ED-1 only. The M2 macrophages were homogenously distributed, without increased densities near the border. The ratio CD206 to ED-1 cells was higher here for the flat condition compared to the micropillar one.

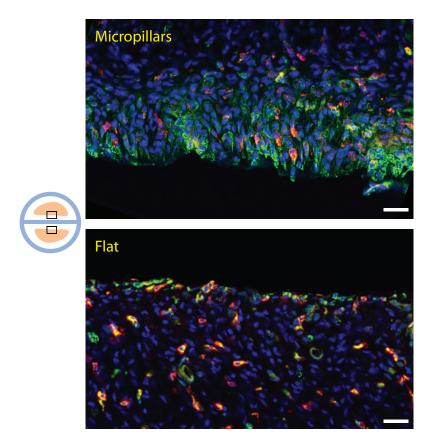


Figure 4.21 – Macrophages near the interface between tissue and material. High magnification confocal microscopy images of regenerated tissue in the vicinity of the central membrane. Green stains for all activated macrophages (ED-1), red for the alternatively activated M2 macrophages (CD206) and blue for cell nuclei (DAPI). Scale bars= $20\,\mu m$ .

## Discussion

Nerve guidance conduits currently constitute one of the major alternatives to autograft for the repair of long nerve defects . The key principle of this technique is to suture the opposing nerves stumps inside of a tube, thereby providing a privileged space for nerve regeneration. It mainly acts by guiding the growing axons and concentrating the multiple factors required for regeneration, such as neurotrophic factors, cells and ECM deposition. Two main objectives are pursued with this strategy: increase the speed and amount of axonal regeneration, and prevent the formation of fibrous tissue at the injury site, which could lead to neuroma. In many ways, regenerative nerve interfaces aim at similar results. Prominent growth of neurons into implanted devices and prevention of fibrosis at the electrode site are paramount for the performance and bio-integration of these interfaces.

Towards this goal, a strategy incorporating a micropillar texture on the surfaces of a nerve conduit was investigated here. The reduction of surface stiffness and the guidance provided by the topographic cues are the 2 rationales behind the use of micropillars. Importantly, this strategy is compatible with current material and processes for fabricating the latest generation of polymeric soft neural implants.

#### 4.4.1 Considerations on the design of the tube and the implantation

The high versatility of soft lithography techniques is well illustrated here by the fabrication of the micro-patterned conduits. The ability of the PDMS to deform has been central to the fabrication process. Using a 100 µm-thin negative mold membrane wrapped around a polystyrene rod, PDMS tubes covered with micropillars on their curved surfaces were created. The selected configuration of micropillars was intended to test whether the reduced effective stiffness would ameliorate the regeneration and reduce the inflammation. On the other side, the vitro experiments presented in Chapter 3 pointed out to a reduction of the number of Schwann cells for effective stiffness in the 1-4 kPa range. For this reason, an intermediate stiffness of 10 kPa was selected for the micropillars in nerve conduits. The interpillar distance was kept relatively small, in order to favor the guidance effect of pillars

on growing axons.

With their inner diameter a bit smaller than 2 mm, the nerve conduits fitted very largely to the sciatic nerve of the rats. In the context of the assessment of micropillar texture effects, the surface of regenerating tissue in contact with the tube should be maximized. For this, one of the possibility would have been to fabricate conduits with smaller diameter, e.g. <1.5 mm. However, this would have called for a new fabrication process. The one designed here was near the limit of the possible miniaturization, in terms of manipulation of the negative molds. Therefore, to increase the contact with between tissue and PDMS, the theta design with its central dividing membrane was created. It effectively augmented the association between tissue and PDMS, as the regenerating tissue cable were mostly growing along the membrane. The cables however did not get in contact with the tube walls, and the half tube spaces were not entirely filled with tissue after 12 weeks post-implantation.

A critical parameter for studies on the regeneration of nerve through nerve conduit is the length of the tube. For most applications, the objective is the repair of transected nerves which are impossible to suture back together, and which need to regenerate over several millimeters to reach the distal stump. To assess the speed of axonal regeneration or Schwann cell migration, studies often use long tubes of 10 to 20 mm. In comparison, the tubes created here have a rather modest distance of regeneration with their 4 mm. At time point down to 2 weeks, axons had reached the distal side in all tubes, preventing an efficient analysis of the axonal regeneration and Schwann cell migration speeds. The rationale for the design of short tubes was to reduce the time needed to reach the filling of the entire luminal space by the tissue. However, none of the theta or simple tubes implanted at the longest time points of 12 weeks reached the point where the tissue totally invaded the tube.

One other determining parameter for nerve regeneration is the duration of the implantation. Whereas short time points are used to determine the speed of cell and axon migration, longer durations allow the observation of the maturation of the tissue inside of the conduit. The longest time point here was 12 weeks. Experiments conducted by colleagues on nerve regeneration through a micro-channel structure showed massive increase of the collagen content between 3 and 9 months (Fig.4.5). The extremely confined space offered by micro-channels for regenerated tissue most probably lead to the compression of the nerve upon maturation. Thus, future studies on the micropillar texture effect might benefit of longer time points, where long-term effects that were are not observable at shorter interval occur. In particular the effect of micropillars on the deposition of connective tissue such as collagen would be advisable.

for both the simple and theta tube

#### 4.4.2 Effect of micropillars on sciatic nerve regeneration

The micropillar texture was firstly assessed for its effect on neuronal tissue regeneration. The area of tissue inside of the tubes constituted the first indication of the ability of the surface topography to modulate the growth of tissue. We observe a reduced tissue area for micropillar-patterned surfaces compared to flat ones at 12 weeks, in both the simple and theta tubes. A trend observed in theta tubes indicated that a decrease over time of the proportion of 'micropillar' tissue compared to 'flat' tissue. Initially larger by almost  $50\,\%$  on the micropillar side, tissue area drops to  $80\,\%$  of the flat one by the 12 weeks time point.

In the theta tubes, the total axonal area was similar for both conditions up to the 4 weeks time point, but more important for the flat surface at 12 weeks. The relatively low number of samples used in this study prevents a robust quantitative effect to be established. However, observations of the tissue area and axonal area are both pointing to a more potent regeneration on the flat surfaces. The relatively similar ratios of axonal to total area in theta tubes indicates that it is mostly the size of the tissue which differed here, as opposed to a variation of the fibrous tissue at the periphery.

The longitudinal section stained for axons and myelin on Fig.4.16 illustrates well the previous remarks. The cable of tissue on the micropillar side is visibly smaller, in particular at the mid-point of the tube. On the other hand, the axonal density that has regenerated to the distal side is fairly similar for both condition. Thus, the micropillar surface may be considered to have little impact on the axonal regeneration potential. It is also backed by the indirect functional assessment constituted by the leg muscle weight measurements in simple tubes. None of conditions demonstrated an improvement over the other in the atrophy of the gastrocnemius and tibialis anterior muscles.

The origin for the shift over time in the proportions of micropillar to flat tissue is open to speculation, with several possible factors acting at different times. At the early time point of 2 weeks, the tissue in contact with micropillar surfaces may benefit of the rapid influx of immune cells like macrophage, which are particularly adherent to these surfaces. This could explain the larger tissue area in comparison to the flat condition. At 12 weeks, the situation is inverted and the flat surfaces support larger tissue that the micropillar one. Oppositely to macrophages, other types of cells important for later stages of the regeneration might be negatively impacted by the micropillars. Aspects such as motility and proliferation of these cells might be affected. According to Minev et al. [158], reduced

motility and proliferation of glial cells on high aspect ratio micropillars were observed. In the context of peripheral nerve regeneration, Schwann cells with lower migration rate would possibly take more time to establish bands of Büngner that allow the ingrowth of axons. Phagocytosis of debris might as well be slowed. One critical aspect which would require investigation is the influence of micropillars on the expression of neurotrophic factors, cytokines or extracellular matrix deposition. For instance, the expression of collagen by periodontal cells was shown to depend on the elasticity and topography of micropillar surfaces [159]. It is not improbable that similar modulation effect could be observed for Schwann cells or fibroblasts in regenerating nerve environment.

The interaction of axons and micropillars could not be observed in this study. The newly formed nerve cables were invariably structured with axons centered on the interior part, and a layer of compact fibrous tissue with varying thickness on the periphery. The presence of the central membrane, with its micropillars and grooves, did not induce a modification of the aforementioned arrangement of the tissue. No increase of the axonal density near these surfaces could be observed either. In this context, it is relatively improbable that axons interact directly with the microstructures. The different cell types intervening during nerve regeneration, such as Schwann cells and macrophages, may rapidly colonize an important portion of the tissue-material interface, preventing a direct contact from growth cones. The effect on Schwann cells or macrophages may however influence indirectly the regeneration. The orientation of Schwann cells by the micropillar topography was shown in vitro, and by extension may occur in the in vivo context as well.

Lastly, the prior coating with a bioactive ECM component such as laminin might be a potential way to empower the effect of micropillar texture. It is motivated by the observation of the increased tissue area for laminin coated simple conduits. The deposition of proteins is generally the initial step after implantation of a foreign material. The conformation of deposited protein at the interface is known to take important role in consecutive cellular events. In that respect, the tissue response might be favorably influenced by a material coated with an appropriate adhesion molecule. Laminin constitute the ideal candidate here, as it is known to promote Schwann cell motility, axonal growth and is one of the principal constituent of the basal lamina.

#### 4.4.3 Effect of micropillars on the immune response

The most dramatic effect of micropillar texture was demonstrated on macrophages. As previously observed in vitro, this type of cell is greatly affect by its underlying topography. The manifold difference in macrophage density between flat and micropillar-patterned

PDMS surfaces was proved valid in the in vivo nerve regeneration context. A striking example of this effect was given by the short term implantation of a theta tube, which was removed after 48 hours only. A this point, fibrin cables had already formed on both side of the tube. The analysis of the surface of the tube revealed a dense population of cells on micropillar surfaces, whereas only few cells were present on the flat areas. The majority (>70%) of these cells expressed the macrophage marker ED-1, regardless of the surface condition. Interestingly, the cells demonstrated the same cytoskeletal organisation as in in vitro samples, with multiple actin rings engulfing micropillars at the center and periphery of the cell. In comparison, the cytoskeleton of cells on flat surface was relatively reduced. The formation of these actin rings surely take a role in the increased adhesion of macrophage to the micropillar surface.

This short term implantation proved that cells could invaded very rapidly the micropillar textured surfaces. This stands somehow in contradiction to the previous hypothesis of reduced cell motility on micropillars. However, the differential behaviour between cell types on micropillars should not be overlooked. The cells in this case were mostly macrophages, which may greatly differ from Schwann cell in their interactions with micro-patterned substrates. Of note, the rapid invasion of macrophages on the micropillar environment may preclude the effect of micropillars on other cells.

The firm attachment of macrophages on micropillars was also observable at later time point. The inspection of pieces of PDMS tubes that were separated from the tissue during the sectioning revealed remaining portions of tissue attached in several cases. Some cells could be present on flat surface as well, in much lower quantities. A common point to both conditions was the phenotype of these cells, which almost all stained for the macrophage marker. Macrophage were seen in contact with the central membrane on these pieces. Unfortunately, no particular effect of the distinct topography and mechanics between stripes was observed. The high density of these cell may have precluded the observation of a clear effect here.

The analysis of a longitudinal section at 12 weeks post-implantation confirmed that the macrophages were not only more abundant at the interfaces, but also in the regenerated tissue as well. The nerve cable in the micropillar space showed a particularly high intensity of macrophage markers at the periphery. In comparison the intensity on the flat side was very modest at the borders. Intensities at the center of the tissue was similar for both conditions, indicating that mostly the exterior of the tissue was affected, while the interior of the cable remained unaffected.

An intriguing point here is the fact that the entire periphery is concerned by the higher

signal intensity. It includes the part of the tissue that is facing outward to the tube wall, and which is in principle not in contact with the surface and micropillars. A possible explanation might be that the macrophages in contact with the surface transmit information regarding the interface to the residing macrophage population. Paracrine signalling or contact-mediated signalling could be envisioned as potential ways of transmitting information here.

In this study, the phenotype of the macrophage in the regenerating tissue was investigated. Current strategies for improving nerve repair include the modulation of the immune response and in particular of macrophage polarization [120, 119, 160, 117]. In a simplistic description, macrophages recruited to an injury site can differentiate into 2 phenotypes: The pro-inflammatory M1 and the pro-repair M2. A timely pattern of activation of both phenotypes is thought to lead to successful regeneration. In the case of predominance of the M1 phenotype at latter stages, adverse effects on the regeneration could occur. Modulation of the phenotype through surface topography has been reported [124, 161]. The effect of micropillar topography on macrophage polarization remains an open question, which would require in vitro experimentation. In this study, the marker CD206 was used to detect the pro-repair M2 macrophages. As seen on the longitudinal section, an important proportion of the macrophages express the M2 marker, indicating a pro-repair phenotype. However, a closer look to the tissue in the 10 to 20 µm from the interface showed the prevalence of the ED-1 marker, with few macrophages staining for the M2 marker. The situation was different for flat PDMS surface, with a more balanced ratio between M1 and M2 phenotypes. Additionally, the pieces of PDMS tubes with remaining cells attached did not stain for CD206. Taken together, these observations seems to indicate a potentially negative effect of the micropillar topography in terms of the modulation of the immune response. The presence of M1 macrophage in high density in the vicinity of the micropillar interface may indicate an over-activation of the pro-inflammatory phenotype by the pillars. The avidity of macrophages to engulf micropillars in actin rings may be an early manifestation of this phenomenon. The micropillars indeed share similar dimensions with some bacteria, potentially inducing frustrated phagocytosis by the macrophages, and stimulating their inflammatory potential.

#### 4.4.4 Implications for the tissue-material interface

The integration of the micropillar texture on a regenerative neural interface was the long term goal motivating this research. In particular, the strangulation of nerve fibers in the micro-channel device, with nervous tissue being slowly replaced by collagen, called for a strategy to prevent such fibrotic reaction. In the light of the investigations and results obtained here, the micropillar texture might not constitute the best option for attaining the objective. The extremely aggressive reaction of macrophages to micropillars seem to override the other potentially beneficial effects, such as the reduced surface stiffness and the guidance by topographic cues. Excessive accumulation of immune cells at the interface would probably sustain the foreign body reaction and hamper the communication with the electrodes.

However, the effect of micropillars on collagen deposition remain to be elucidated. For this, longer time points should be used in combination with designs mimicking the micro-channel confinement. The adhered macrophages normally form multi-nucleated giant cells at the surface of foreign material, in the classical steps towards encapsulation. A compromised mobility or an excessive surface attachment raise the question of the transition to this multi-nucleated state for macrophages on micropillars.

Another aspect which should be investigated is the use of supporting cells, such as stem cells, to encourage regeneration in neural devices. The previous chapter reported an increased attachment of adipose tissue-derived stem cells to micropillar topography compared to flat PDMS surface. In this context, the incorporation of micropillars could ameliorate the attachment and survival of the cells seeded inside of PDMS implants.

Finally, the potential of micropillar texture for the modulation of tissue reaction might be more adequate in other application where the proliferation of immune cells is recommended. The process of wound healing for instance may benefit from an accumulation of macrophages during granulation of the tissue.

## Conclusion

This chapter reviews the in vivo experiments that were performed in order to assess the effect of micropillar on nerve regeneration. The end goal of this strategy is to increase the bio-integration and functionality on the long-term of regenerative nerve interfaces. PDMS nerve guidance conduits featuring inner surfaces patterned with micropillar were fabricated. In line with observations made in the in vitro experimentation, a configuration of micropillar with intermediate stiffness was chosen. At 10 kPa, the micropillar are meant to provide a soft environment without the deleterious side effects on the proliferation of cells. After the creation of a simple tube, a theta design was conceived in order to increase the tissue-material contact. A central membrane divided the lumen into one half space covered with micropillar and the other half having flat PDMS surfaces. It enabled the direct comparison of both conditions.

The effect of micropillars in nerve conduits was studied on the transected sciatic nerve of rat at time points up to 12 weeks. Tissue regenerated in contact with micropillars demonstrated smaller area than on flat surface at 12 weeks, while coating the micropillars with laminin improved largely this parameter. The regeneration of axons remained poorly affected by the topography of the surface. Axonal area was similar up to 4 weeks after implantation, but larger on flat surfaces at 12 weeks, due to increased tissue area. The second investigated parameter was the immune response to micropillars. A strong reaction of macrophages was observed at short term, with fast invasion of the micropillar environment and tight anchoring to the pillars through actin rings. This latter could be interpreted as a tentative to internalize the pillars, which may appear as bacteria for the macrophages. At the longer time point of 12 weeks, the macrophages were found in higher density at the periphery of tissue on the micropillars side, compared to flat condition. Analysis of the phenotype of the macrophages at the border indicated that the pro-inflammatory M1 phenotype is predominantly represented in the first layer of cells in contact with the micropillars.

Taken together, these investigations point to a probable negative effect of the micropillars on nerve regeneration. For these reason, their use on regenerative neural interfaces as a

#### Chapter 4. Evaluation of Micropillar Texture in vivo

strategy for improved bio-integration might be compromised. However, their effect on the deposition of collagen in the case of nerve strangulation was not covered here. Future studies should include longer time points, in order to observe the deposition of collagenous matrix on micropillar textured surfaces.

# 5

# CONCLUSIONS

This chapter closes the thesis with a global look over the results. Their significance in the context of peripheral nerve interfaces is discussed. Lastly, potential future developments and perspectives are outlined.

#### Contents

5.1 Summary of the results	152
5.2 Significance	156
5.3 Outlook and Perspectives	158

5.1

# Summary of the results

The overall objective of this thesis was to evaluate micropillars as a texture to modulate the interactions of peripheral nerve cells with PDMS surfaces. At the microscopic level, micropillars not only provide topographic cues, they also decrease the effective mechanical stiffness of the surface. Cells can integrate the physical parameters encountered in the surrounding environment and modify several aspects of their machinery accordingly. The possibility of modulating cellular behaviour with micropillars was envisioned here as a strategy for enhancing the bio-integration of silicone neural implants in the PNS. Essentially, promotion of neuronal growth and prevention of fibrotic encapsulation were targeted.

In the initial phase, micropillars arrays of different dimensions were fabricated, with the aim to determine the effect of the geometrical parameters on cells and identify favorable configurations. Microfabrication technologies were employed to create a hard mold etched on a silicon wafer, which presented a library of micropillar configurations. The microstructures were reproduced on PDMS surfaces by replica molding. This soft lithography process enabled the rapid fabrication of substrates for material characterization and in vitro assays. The mechanical behaviour of micropillars under bending, simulated with FEM, allowed to estimate the pillar spring constants and the effective modulus of the surface. A reduction of the elastic modulus down to 3 orders of magnitude compared to bulk PDMS was obtained with the softest configuration D1. ( $E^{PDMS}$ =1.95 MPa,  $E^{D1}$ =0.7 kPa) The range of effective stiffness produced was comparable with the Young's modulus of soft tissue, and with the compliance of substrates used for cellular mechanosensitivity studies.

The effect of micropillar diameter and interpillar spacing were investigated in vitro. For this, two chips were utilized. The first one, Chip 9, had 4 arrays with different diameters of micropillars (1.2, 2.2, 3.2 and 4.2  $\mu$ m) and constant spacing (3  $\mu$ m). This translated into 4 effective elastic moduli, allowing to probe the response of cells as function of the mechanical properties. The second chip, Chip 1, had 3 arrays with different interpillar spacings (1.0, 3.5 and 7.5  $\mu$ m) and constant diameter (ca. 1.3  $\mu$ m). This was used to probe the effect of pillar density/surface area variations.

The dorsal root ganglia (DRG) of adult rats, which enclose the somata of sensory neurons, were dissociated to obtain individual cells. The resulting heterogenous population, containing neurons, glial cells and fibroblasts, was used as a model for studying the effect of the micropillars on cells derived from the PNS. After 7 days of incubation in vitro, neurons presented extended processes on all types of surfaces. However, no preferential configurations was detected, as similar densities of neurons were found on all arrays as well as flat surfaces. In contrast, the proliferation of glial cells was affected by the micropillars. Their density was significantly decreased on the two smallest pillars diameters (2.2 and  $1.2\,\mu\text{m}$ ), suggesting a negative influence of substrate stiffness in the 4-0.7 kPa range. On Chip 1, the two largest interpillar spacings (3.5 and 7.5  $\mu$ m) displayed significantly lower glial cells than the densest S1 (S=1.0  $\mu$ m), which was in turn similar to flat surface. The intermediary spacing (3.5  $\mu$ m) was the most deleterious for glial cell proliferation.

The interactions of neurons with the micropillars were further characterized by inspecting their 3D integration, neurite orientation, soma morphology and applied traction forces. Despite permissive adhesion molecules (PDL and Laminin) covering the bottom, shafts and tops of pillars, neuron somata resided mostly on the top of pillars, regardless of interpillar spacing. Similarly, their neurites were anchored near the top part of micropillars, with freestanding portions between the posts. These observations indicated that neurons could effectively experience the flexibility of pillars. As an indirect measure of mechanosensitivity, the area of somata on the different micropillar diameters was quantified. Higher fractions of small, round somata were found on the softest configuration (D1,D2), compared to the stiffer D3 and D4, both similar to flat control. Thus, the upper limit of mechanosensitivity for DRG neurons was found between 12.3 and 4 kPa (D2-D3). Further indications supporting this threshold came from the drop of traction forces amplitude applied by neurons on micropillars between D3 and D2. The lower forces applied on D2 (4 kPa) suggested that the neurons had integrated the stiffness of their substrate and adapted their traction force to maintain constant deformation.

Neurites are known to use contact guidance as a pathfinding mechanism. In that context, the presence of micropillars on the surface constituted topographical cues which largely affected the orientation of growing neurites. Their alignment to the axes of the micropillar arrays increased with the reduction of interpillar spacing, displaying prominent alignment on the smallest spacing S1. Interestingly, a small variation of spacing between the X- and Y-axis directions on S1 (Sx=1.0, Sy=1.2) demonstrated a dramatic effect over the neurite orientation. Most aligned neurite segments were observed along the smallest Sx direction compared to the opposite Y-axis. This suggested a very high sensitivity of growing neurites to topography in the nanometer range.

To conclude the in vitro work, pilot experiments were realized on macrophages and adiposederived stem cells on micropillars. The former cell type is an important modulator of the inflammation response and thus particularly relevant in the context of implanted material. Macrophages were at least 4 times more numerous on micropillars than on flat PDMS, regardless of the configuration. Variations of spacing but not diameter induced modification of their density. On average, the least dense array S7 supported 2.5 times more macrophages than the densest S1. Their cytoskeleton showed intense actin filaments encircling the micropillars, providing tight anchoring to the substrate. Together, these observations concurred to the hypothesis that macrophages attempted to phagocytize the micropillars, possibly due to their similarity with bacterial dimensions.

Adipose-derived stem cells can be differentiated into Schwann cells and pre-loaded into nerve guidance conduits to enhance regeneration. Modulating their attachment to surfaces through micropillars was therefore of interest. After 7 days of incubation, the density of stem cells was multiplied by a factor from 2 to 4 on micropillars, compared to flat surface. Their density also increased as an effect of pillar diameter reduction. This was accompanied by a decrease in cell area and an increase in circularity. According to these results, we can hypothesize that stem cells integrated and responded to the mechanical cues presented by micropillars. Furthermore, it suggested that soft substrates with moduli around 1-4 kPa (and possibly lower) could improve the attachment of these cells.

In parallel to the in vitro experimentation, the effect of micropillars was investigated in the in vivo context on rat sciatic nerve regeneration. For this, nerve guidance conduits presenting micropillar textures with intermediate stiffness (10 kPa) were fabricated in PDMS. The objective with this configuration of micropillars was to promote axonal growth with a reduced surface stiffness, while avoiding the decrease of cell proliferation observed on the two softest surfaces (0.7-4 kPa) in vitro. Taking advantage of the flexibility of the PDMS negative molds, the micropillars were patterned on the curved inner surfaces of the tubes. On certain tubes, a longitudinal flat membrane was added at the center, dividing the lumen in one micropillar-textured half and one non-patterned half. This design, also defined as Theta structure in the text, increased the contact surface between tissue and PDMS surfaces and allowed to study the effect of micropillars and flat surface in the same experimental conditions.

The distal and proximal stumps of sciatic nerve were sutured at each extremities of the tube, and the nervous tissue was let to regenerate inside of the tubes for up to 3 months. In both conditions (flat and micropillars), a continuous layer of fibrinous tissue rapidly crossed the tube length (4 mm) to establish contact between the proximal and distal parts

of the nerve. Globally, the regeneration of the tissue was only slightly superior on flat surfaces at 12 weeks, with larger total tissue area and axonal area compared to micropillar surfaces. However, these differences were not statistically significant and muscular atrophy was the same for both conditions.

Conversly, the response of macrophages, which play a major role in inflammation and tissue remodelling, was greatly affected by the micropillars. 48 hours after implantation of the conduits, the cells, most of them positively stained against the macrophage marker ED-1, massively spread across the micropillar surfaces, whereas only a few were seen attached to flat surfaces. A similar situation was observed after 12 weeks of implantation. Layers of cells were found attached to conduit surfaces with micropillars. In contrast, the flat condition left very few cells attached to the surfaces. Macrophages were found also more abundant at the periphery of the tissue cables in micropillar-textured lumen compared to flat-textured lumen. The M2 phenotype of macrophages, which favors tissue repair, was well represented in both conditions. However, it was found to be decreased near the interfaces with micropillars.

Altogether, the in vitro and in vivo results indicated that the reduction of surface stiffness through micropillar did not affect the growth of peripheral neurons, despite the demonstration of their mechanosensitivity. Macrophages showed a consistent behaviour in both the in vitro and in vivo contexts. Their proliferation and tight anchoring to micropillar surfaces in vitro was translated in denser population for nerve tissue regenerating in contact with micropillars.

.

5.2

## Significance

Silicone micropillar arrays have been first introduced as a bioengineering tool more than 10 years ago [29]. Since then, they became largely exploited to decipher cellular biomechanics phenomena and substrate stiffness influence on cell function [31, 25, 66]. An increasing number of cell types were characterized on micropillars, endothelial cells [162], cardiomyocytes [163], keratinocytes [164] or epithelial cells [159], to cite a few.

The work presented in this thesis contributes to this body of knowledge by reporting on the topographic and mechanical interactions of PNS cells with PDMS micropillars. While numerous studies investigated CNS/PNS cell biomechanics with polyacrylamide or agarose gels [22, 61, 63], very few made use of PDMS micropillar arrays as mechanical cues for neurons and glia. Notable exceptions include studies on the differentiation of neural stem cells [165, 166], on the electrophysiology of DRG neurons [167] and on the behaviour of glial cells from the CNS [158]. However, the aims, cell types or experimental conditions described in these papers differed from the present work. In this perspective, the effect of micropillars on glial cells proliferation, soma morphology, neurite alignment and traction forces amplitude constitute unprecedentedly reported observations. The threshold value for glial cell and soma mechanosensitivity, found between 4 and 12.3 kPa on micropillars, corresponded to the range previously reported with other means [62, 61]. These results may serve as a basis for the design of implant surfaces with physical parameters inducing specific effects on cells.

The response of macrophages to surface topography on various materials is increasingly investigated, with demonstrated effects on their density, morphology, activation, phenotypes or cytokine expression [168, 123, 169]. Titanium surfaces with roughness parameters in the micron range were shown to modulate proinflammatory cytokines and chemokines expression by macrophages [168]. Micro-structured surfaces altered macrophage activation, whereas nano-textured one did not [123]. Topography in the form of micro- to submicron (500 nm) gratings affected macrophage adhesion, morphology and cytokine expression in comparison to flat surfaces on 3 different types of polymers [161]. However, no distinctive

reaction has been found between the different types of gratings, and macrophages were insensitive to nanotopography smaller than 500 nm [161].

With the exception of a study using larger pillars (D=10 µm, H=14-25 µm) [97], this thesis presents one of the first observation of the response of macrophages to PDMS micropillars. A dramatic increase of macrophage density on all types of micropillar arrays was here demonstrated. This contrasted with the results found in the pre-cited paper [97], where macrophage density was inhibited or unaffected by the pillars. This divergence might be explained by the difference of pillar dimensions. Alternatively, the fact that the micropillars from that study were not coated with PDL might have played a role. Interestingly, the effect of microstructure density (pillar spacing) was found as an effective way to modulate the attachment of macrophages. This effect, which mostly rely on geometrically dimensions, may be applied to other materials in order to control macrophage populations at the surface.

Texturing the surface of implants to ameliorate their integration and lifetime in the body is not an entirely novel idea. The development of silicone breast implants in particular stirred research in this domain decades ago, with the aim to reduce collagen deposition and fibrous capsule formation [170, 171]. Some textures on these implants consisted of pillar arrays with dimensions in the hundreds of micron range. The use of micropillars largely smaller than the cell size has a very distinct effect. Cells resting on a bed of micropillars are able to bend them, which provides mechanical feedback and potentially induces specific cellular functions such as migration, proliferation or differentiation [59, 162, 25, 172]. Making use of this cell-instructive textures is the approach pursued in this thesis for ameliorating PNS tissue interactions with PDMS surfaces. To the best of the author's knowledge, a mere 2 papers from the same group report on the effect of PDMS micropillars implanted subcutaneously in vivo [97, 173]. Again, these pillars had larger diameters (10 μm) and heights (14-25 μm). Thus, the use of micron-sized pillars on nerve regeneration described here is not covered by other studies. The results from these investigations pointed out to a strong effect of micropillars on macrophages, which were recruited to greater extent compared to flat surfaces, while axonal regeneration remained poorly affected. A strict correlation between macrophage number and fibrotic tissue formation is not currently demonstrated [97]. Additional parameters such macrophage activation and fusion into foreign body giant cells play a critical role in foreign body reaction and might be modulated by the topography. Alternatively, the proliferation of fibroblasts, and fibrocytes in particular, showed good correlation with indicators of fibrotic reaction [97]. Thus, while macrophages were highly recruited to micropillar surfaces, several other parameters have to be considered to establish a definitive link between micropillars and tissue response.

## Outlook and Perspectives

The initial motivation behind this thesis was to improve the response of PNS tissue to neural implants with micro-textured surfaces. Adopting micropillars as a strategy towards this aim opened many questions pertaining to cellular mechanosensitivity, mechanotransduction and topography sensitivity. Considering the different cell types involved, these questions have implications in fields such as neural biomechanics, tissue engineering or immunomodulation. One of the great merit of micropillars comes from their duality as a mechanical force sensor and substrate stiffness modulator, which makes them apt to study these multiple aspects.

The mechanisms of neuronal interactions with micropillars remain to be fully characterized. The presence of glial cells in the cultures notably influenced the growth of neurons, preventing the description of purely neuron-pillar interactions. While the morphology of soma was modified by micropillar mechanical cues, the integration of these cues by growth cones could not be observed. Future experiments should include highly purified cultures and earlier time points to address this question. One of the striking observations in vitro was the localization of neurites near the top part of micropillars, even for the largest spacing of 7.5 µm. This phenomenon may arise from the glial-neurite association or from the internal tensions generated in the neurite network. In the latter case, micropillars may allow to measure these tension forces and provide new insight to force generation and propagation during neurite elongation.

Overall, the beneficial effect of low substrate stiffness on neuronal growth, previously described and generally admitted, was not observed in our experiments. One should take here into consideration the perilous generalization of observations made with different chemistries, materials, compliances or cell types, which renders comparisons difficult. Importantly, the micropillar arrays created might not have reached a sufficiently low modulus to capture a positive effect. Also, their dimensions are relatively large compared to growth cones and neurites, which might not be able to perceive the mechanical cues on this scale. In this perspective, the use of micropillar texture on the nanometer scale might appear as smoother, while retaining the mechanical effect. Achieving such pattern

resolution would require an alternative fabrication process. Techniques such as focused ion beam milling, electron beam lithography, epitaxial electrodeposition or block copolymer lithography are capable of patterning high aspect ratio nanopillars in diverse materials.

An interesting future line of work with the micropillar developed here should include a complete characterization of cell types, such as fibrocytes and foreign body giant cells, as well as the observation of collagen deposition. This promises a more comprehensive understanding of the influence of micropillars on foreign body reaction. Micropillars have been shown to favor stem cell differentiation into adipogenic or osteogenic lineage depending on their mechanical flexibility [25]. Similarly, the modulation of adipose-derived stem cells differentiation into Schwann cells by micropillars should be investigated. One can hypothesize that micropillar arrays with tailored stiffness could favor differentiation into the Schwann cell phenotype. This would constitutes an interesting approach in the frame of the incorporation of support cells onto nerve conduits for improved regeneration. Conduit surfaces patterned with micropillars could increase the attachment and viability of stem cells, as well as the yield of Schwann cell differentiation, thus improving the support to regenerating neurons.

Finally, while it was a motivation for the present research, the integration of a micropillar texture with an electrode-bearing device remains to be addressed. A rationale for using exclusively PDMS micropillars in this study was the compatibility and facilitated integration with recent silicone neural interfaces. Moreover, PDMS has been considered the most reliable material among a pool of polymers for the fabrication of neural implants [9]. In an all-PDMS device, gold thin films could be readily deposited on micropillar arrays to form electrodes with three-dimensional surfaces. In the case of the microchannel regenerative interface, coating the inner walls of the channels with micropillars may prove to be an effective strategy for avoiding fibroblast proliferation and over-deposition of collagen, which potentially hinder the proper functioning of the device.

Altogether, micropillars constitute a promising approach to instruct cell behaviour and modulate tissue-material interactions. The demonstration of the possibility to finely tune essential parameters such as cell adhesion with simple modification of the pillar geometry should motivate further research in this domain.

## **BIBLIOGRAPHY**

- [1] Alim Louis Benabid. Deep brain stimulation for parkinson's disease. Current opinion in neurobiology, 13(6):696–706, 2003.
- [2] Gerald E Loeb. Cochlear prosthetics. Annual review of neuroscience, 13(1):357–371, 1990.
- [3] DM Long. The current status of electrical stimulation of the nervous system for the relief of chronic pain. Surgical neurology, 49(2):142–144, 1998.
- [4] C. Hassler, T. Boretius, and T. Stieglitz. Polymers for neural implants. *Journal of Polymer Science Part B-Polymer Physics*, 49(1):18–33, 2011.
- [5] Patrick J Rousche and Richard A Normann. Chronic recording capability of the utah intracortical electrode array in cat sensory cortex. *Journal of neuroscience methods*, 82(1):1–15, 1998.
- [6] W. M. Grill, S. E. Norman, and R. V. Bellamkonda. Implanted neural interfaces: biochallenges and engineered solutions. *Annu Rev Biomed Eng*, 11:1–24, 2009.
- [7] X. Navarro, T. B. Krueger, N. Lago, S. Micera, T. Stieglitz, and P. Dario. A critical review of interfaces with the peripheral nervous system for the control of neuroprostheses and hybrid bionic systems. *Journal of the Peripheral Nervous System*, 10(3):229–58, 2005.
- [8] J. O. Larsen, M. Thomsen, M. Haugland, and T. Sinkjaer. Degeneration and regeneration in rabbit peripheral nerve with long-term nerve cuff electrode implant: a stereological study of myelinated and unmyelinated axons. *Acta Neuropathol*, 96 (4):365–78, 1998.
- [9] T. Boretius, J. Badia, A. Pascual-Font, M. Schuettler, X. Navarro, K. Yoshida, and T. Stieglitz. A transverse intrafascicular multichannel electrode (time) to interface with the peripheral nerve. *Biosens Bioelectron*, 26(1):62–9, 2010.
- [10] S. P. Lacour, S. Benmerah, E. Tarte, J. FitzGerald, J. Serra, S. McMahon, J. Fawcett, O. Graudejus, Z. Yu, and B. Morrison. Flexible and stretchable micro-electrodes for

- in vitro and in vivo neural interfaces. Medical & Biological Engineering & Computing,  $48(10):945-954,\ 2010.$
- [11] Paolo Dario, Paolo Garzella, Maurizio Toro, Silvestro Micera, Mani Alavi, Uwe Meyer, Elena Valderrama, L Sebatiani, Brunello Ghelarducci, Cristina Mazzoni, et al. Neural interfaces for regenerated nerve stimulation and recording. Rehabilitation Engineering, IEEE Transactions on, 6(4):353–363, 1998.
- [12] Stéphanie P. Lacour, Raghied Atta, James J. FitzGerald, Mark Blamire, Edward Tarte, and James Fawcett. Polyimide micro-channel arrays for peripheral nerve regenerative implants. Sensors and Actuators A: Physical, 147(2):456–463, 2008.
- [13] S. P. Lacour, J. J. Fitzgerald, N. Lago, E. Tarte, S. McMahon, and J. Fawcett. Long micro-channel electrode arrays: a novel type of regenerative peripheral nerve interface. *IEEE Trans Neural Syst Rehabil Eng*, 17(5):454–60, 2009.
- [14] Akhil Srinivasan, Mayank Tahilramani, John T. Bentley, Russell K. Gore, Daniel C. Millard, Vivek J. Mukhatyar, Anish Joseph, Adel S. Haque, Garrett B. Stanley, Arthur W. English, and Ravi V. Bellamkonda. Microchannel-based regenerative scaffold for chronic peripheral nerve interfacing in amputees. *Biomaterials*, 41(0): 151–165, 2015.
- [15] P. A. Wieringa, R. W. F. Wiertz, E. L. de Weerd, and W. L. C. Rutten. In vitro verification of a 3-d regenerative neural interface design: Examination of neurite growth and electrical properties within a bifurcating microchannel structure. *Proceedings of the Ieee*, 98(3):389–397, 2010.
- [16] J. J. FitzGerald, N. Lago, S. Benmerah, J. Serra, C. P. Watling, R. E. Cameron, E. Tarte, S. P. Lacour, S. B. McMahon, and J. W. Fawcett. A regenerative microchannel neural interface for recording from and stimulating peripheral axons in vivo. J Neural Eng, 9(1):016010, 2012.
- [17] Vadim S. Polikov, Patrick A. Tresco, and William M. Reichert. Response of brain tissue to chronically implanted neural electrodes. *Journal of Neuroscience Methods*, 148(1):1–18, 2005.
- [18] David J Edel, VV Toi, Vincent M McNeil, and Lloyd D Clark. Factors influencing the biocompatibility of insertable silicon microshafts in cerebral cortex. *Biomedical Engineering*, *IEEE Transactions on*, 39(6):635–643, 1992.
- [19] Miguel AL Nicolelis, Dragan Dimitrov, Jose M Carmena, Roy Crist, Gary Lehew, Jerald D Kralik, and Steven P Wise. Chronic, multisite, multielectrode recordings

- in macaque monkeys. Proceedings of the National Academy of Sciences, 100(19): 11041–11046, 2003.
- [20] D. H. Szarowski, M. D. Andersen, S. Retterer, A. J. Spence, M. Isaacson, H. G. Craighead, J. N. Turner, and W. Shain. Brain responses to micro-machined silicon devices. *Brain Research*, 983(1–2):23–35, 2003.
- [21] P. A. Janmey, I. Levental, and P. C. Georges. Soft biological materials and their impact on cell function. *Soft Matter*, 3(3):299–306, 2007.
- [22] A. P. Balgude, X. Yu, A. Szymanski, and R. V. Bellamkonda. Agarose gel stiffness determines rate of drg neurite extension in 3d cultures. *Biomaterials*, 22(10):1077–84, 2001.
- [23] L. A. Flanagan, Y. E. Ju, B. Marg, M. Osterfield, and P. A. Janmey. Neurite branching on deformable substrates. *Neuroreport*, 13(18):2411–5, 2002.
- [24] Karol Miller, Kiyoyuki Chinzei, Girma Orssengo, and Piotr Bednarz. Mechanical properties of brain tissue in-vivo: experiment and computer simulation. *Journal of biomechanics*, 33(11):1369–1376, 2000.
- [25] J. Fu, Y. K. Wang, M. T. Yang, R. A. Desai, X. Yu, Z. Liu, and C. S. Chen. Mechanical regulation of cell function with geometrically modulated elastomeric substrates. *Nat Methods*, 7(9):733–6, 2010.
- [26] Chen Shi, Xin Cui, Xurui Zhang, Plamen Tchoukov, Qingxia Liu, Noemi Encinas, Maxime Paven, Florian Geyer, Doris Vollmer, Zhenghe Xu, et al. Interaction between air bubbles and superhydrophobic surfaces in aqueous solutions. *Langmuir*, 2015.
- [27] W. G. Bae, D. Kim, and K. Y. Suh. Instantly switchable adhesion of bridged fibrillar adhesive via gecko-inspired detachment mechanism and its application to a transportation system. *Nanoscale*, 2013.
- [28] Sami Myllymaa, Sami Pirinen, Katja Myllymaa, Mika Suvanto, Tapani A Pakkanen, Tuula T Pakkanen, and Reijo Lappalainen. Improving electrochemical performance of flexible thin film electrodes with micropillar array structures. *Measurement Science* and Technology, 23(12):125701, 2012.
- [29] J. L. Tan, J. Tien, D. M. Pirone, D. S. Gray, K. Bhadriraju, and C. S. Chen. Cells lying on a bed of microneedles: an approach to isolate mechanical force. *Proc Natl* Acad Sci U S A, 100(4):1484–9, 2003.

- [30] Marion Ghibaudo, Léa Trichet, Jimmy Le Digabel, Alain Richert, Pascal Hersen, and Benoît Ladoux. Substrate topography induces a crossover from 2d to 3d behavior in fibroblast migration. *Biophysical Journal*, 97(1):357–368, 2009.
- [31] M. Ghibaudo, J. M. Di Meglio, P. Hersen, and B. Ladoux. Mechanics of cell spreading within 3d-micropatterned environments. Lab Chip, 11(5):805–12, 2011.
- [32] Dong Qin, Younan Xia, and George M Whitesides. Soft lithography for micro-and nanoscale patterning. *Nature protocols*, 5(3):491–502, 2010.
- [33] Younan Xia and George M Whitesides. Soft lithography. Annual review of materials science, 28(1):153–184, 1998.
- [34] Younan Xia and George M. Whitesides. Soft lithography. Angewandte Chemie International Edition, 37(5):550–575, 1998.
- [35] Christopher S Chen, Milan Mrksich, Sui Huang, George M Whitesides, and Donald E Ingber. Geometric control of cell life and death. Science, 276(5317):1425–1428, 1997.
- [36] Xiao-Mei Zhao, Younan Xia, and George M Whitesides. Fabrication of threedimensional micro-structures: Microtransfer molding. Advanced Materials, 8(10): 837–840, 1996.
- [37] Younan Xia, Jabez J McClelland, Rajeev Gupta, Dong Qin, Xiao-Mei Zhao, Lydia L Sohn, Robert J Celotta, and George M Whitesides. Replica molding using polymeric materials: A practical step toward nanomanufacturing. Advanced Materials, 9(2): 147–149, 1997.
- [38] Enoch Kim, Younan Xia, and George M. Whitesides. Polymer microstructures formed by moulding in capillaries. *Nature*, 376:581–584, 1995.
- [39] Enoch King, Younan Xia, Xiao-Mei Zhao, and George M Whitesides. Solvent-assisted microcontact molding: A convenient method for fabricating three-dimensional structures on surfaces of polymers. *Advanced Materials*, 9(8):651–654, 1997.
- [40] Jeong Won Park, Behrad Vahidi, Anne M Taylor, Seog Woo Rhee, and Noo Li Jeon. Microfluidic culture platform for neuroscience research. *Nature protocols*, 1(4): 2128–2136, 2006.
- [41] Kwanghun Chung, Matthew M Crane, and Hang Lu. Automated on-chip rapid microscopy, phenotyping and sorting of c. elegans. *Nature methods*, 5(7):637–643, 2008.

- [42] Julia M Sidorova, Nianzhen Li, David C Schwartz, Albert Folch, and Raymond J Monnat Jr. Microfluidic-assisted analysis of replicating dna molecules. *Nature* protocols, 4(6):849–861, 2009.
- [43] D. Fuard, T. Tzvetkova-Chevolleau, S. Decossas, P. Tracqui, and P. Schiavone. Optimization of poly-di-methyl-siloxane (pdms) substrates for studying cellular adhesion and motility. *Microelectronic Engineering*, 85(5-6):1289–1293, 2008.
- [44] James L Wilbur, Rebecca J Jackman, George M Whitesides, Eunice L Cheung, Larry K Lee, and Mara G Prentiss. Elastomeric optics. *Chemistry of materials*, 8(7): 1380–1385, 1996.
- [45] Dongchan Ahn and Ali Dhinojwala. Sum frequency generation vibrational spectroscopy of silicone surfaces & interfaces. In Silicone Surface Science, pages 23–58. Springer, 2012.
- [46] Lin Wang, Bing Sun, Katherine S. Ziemer, Gilda A. Barabino, and Rebecca L. Carrier. Chemical and physical modifications to poly(dimethylsiloxane) surfaces affect adhesion of caco-2 cells. *Journal of Biomedical Materials Research Part A*, 93A(4):1260–1271, 2010. ISSN 1552-4965. doi: 10.1002/jbm.a.32621. URL http://dx.doi.org/10.1002/jbm.a.32621.
- [47] H. K. Ye, Z. Y. Gu, and D. H. Gracias. Kinetics of ultraviolet and plasma surface modification of poly(dimethylsiloxane) probed by sum frequency vibrational spectroscopy. *Langmuir*, 22(4):1863–1868, 2006.
- [48] James J. Cunningham, Janeta Nikolovski, Jennifer J. Linderman, and David J. Mooney. Quantification of fibronectin adsorption to silicone-rubber cell culture substrates. *Biotechniques*, 32(4):876, 878, 880 passim, Apr 2002.
- [49] Hua Ai, Yuri M. Lvov, David K. Mills, Merilyn Jennings, Jonathan S. Alexander, and Steven A. Jones. Coating and selective deposition of nanofilm on silicone rubber for cell adhesion and growth. *Cell Biochem Biophys*, 38(2):103–114, 2003. doi: 10.1385/CBB:38:2:103. URL http://dx.doi.org/10.1385/CBB:38:2:103.
- [50] N. Völcker, D. Klee, H. Höcker, and S. Langefeld. Functionalization of silicone rubber for the covalent immobilization of fibronectin. J Mater Sci Mater Med, 12(2):111–119, Feb 2001.
- [51] Pierre-Jean Wipff, Hicham Majd, Chitrangada Acharya, Lara Buscemi, Jean-Jacques Meister, and Boris Hinz. The covalent attachment of adhesion molecules to silicone membranes for cell stretching applications. *Biomaterials*, 30(9):1781–1789, Mar

- 2009. doi: 10.1016/j.biomaterials.2008.12.022. URL http://dx.doi.org/10.1016/j.biomaterials.2008.12.022.
- [52] Rupert Timpl, Heilwig Rohde, P Gehron Robey, Stephen I Rennard, Jean-Michel Foidart, and George R Martin. Laminin-a glycoprotein from basement membranes. Journal of Biological Chemistry, 254(19):9933-9937, 1979.
- [53] HK Kleinman, L Luckenbill-Edds, FW Cannon, and GC Sephel. Use of extracellular matrix components for cell culture. *Analytical biochemistry*, 166(1):1–13, 1987.
- [54] Päivi Liesi. Laminin and fibronectin and their cellular receptors during neural development. Seminars in Neuroscience, 3(4):331 340, 1991. ISSN 1044-5765. doi: http://dx.doi.org/10.1016/1044-5765(91)90050-X. URL http://www.sciencedirect.com/science/article/pii/104457659190050X. Cell Adhesion Molecules in the Nervous System.
- [55] Marston Manthorpe, Eva Engvall, Erkki Ruoslahti, Frank M Longo, George E Davis, and Silvio Varon. Laminin promotes neuritic regeneration from cultured peripheral and central neurons. The Journal of cell biology, 97(6):1882–1890, 1983.
- [56] I. Schoen, W. Hu, E. Klotzsch, and V. Vogel. Probing cellular traction forces by micropillar arrays: contribution of substrate warping to pillar deflection. *Nano Lett*, 10(5):1823–30, 2010.
- [57] Kweku A Addae-Mensah, Nicholas J Kassebaum, Michael J Bowers, Ronald S Reiserer, Sandra J Rosenthal, Paul E Moore, and John P Wikswo. A flexible, quantum dot-labeled cantilever post array for studying cellular microforces. Sensors and Actuators A: Physical, 136(1):385–397, 2007.
- [58] O. du Roure, A. Saez, A. Buguin, R. H. Austin, P. Chavrier, P. Silberzan, and B. Ladoux. Force mapping in epithelial cell migration. *Proc Natl Acad Sci U S A*, 102(7):2390–5, 2005.
- [59] M. Ghibaudo, A. Saez, L. Trichet, A. Xayaphoummine, J. Browaeys, P. Silberzan, A. Buguin, and B. Ladoux. Traction forces and rigidity sensing regulate cell functions. Soft Matter, 4(9):1836–1843, 2008.
- [60] Jr. Pelham, R. J. and Y. Wang. Cell locomotion and focal adhesions are regulated by substrate flexibility. Proc Natl Acad Sci U S A, 94(25):13661–5, 1997.
- [61] D. Koch, W. J. Rosoff, J. Jiang, H. M. Geller, and J. S. Urbach. Strength in the periphery: growth cone biomechanics and substrate rigidity response in peripheral and central nervous system neurons. *Biophys J*, 102(3):452–60, 2012.

- [62] Y. Gu, Y. Ji, Y. Zhao, Y. Liu, F. Ding, X. Gu, and Y. Yang. The influence of substrate stiffness on the behavior and functions of schwann cells in culture. *Biomaterials*, 33 (28):6672–81, 2012.
- [63] P. Moshayedi, F. Costa L. da, A. Christ, S. P. Lacour, J. Fawcett, J. Guck, and K. Franze. Mechanosensitivity of astrocytes on optimized polyacrylamide gels analyzed by quantitative morphometry. J Phys Condens Matter, 22(19):194114, 2010.
- [64] P. C. Georges, W. J. Miller, D. F. Meaney, E. S. Sawyer, and P. A. Janmey. Matrices with compliance comparable to that of brain tissue select neuronal over glial growth in mixed cortical cultures. *Biophys J*, 90(8):3012–8, 2006.
- [65] R. D. Sochol, A. T. Higa, R. R. R. Janairo, S. Li, and L. Lin. Effects of micropost spacing and stiffness on cell motility. *Micro & Nano Letters*, 6(5):323–326, 2011.
- [66] R. D. Sochol, A. T. Higa, R. R. R. Janairo, S. Li, and L. W. Lin. Unidirectional mechanical cellular stimuli via micropost array gradients. *Soft Matter*, 7(10):4606– 4609, 2011.
- [67] M. T. Yang, N. J. Sniadecki, and C. S. Chen. Geometric considerations of microto nanoscale elastomeric post arrays to study cellular traction forces. Advanced Materials, 19(20):3119-+, 2007.
- [68] D. M. Thompson and H. M. Buettner. Oriented schwann cell monolayers for directed neurite outgrowth. Ann Biomed Eng, 32(8):1120-30, 2004.
- [69] D. M. Thompson and H. M. Buettner. Neurite outgrowth is directed by schwann cell alignment in the absence of other guidance cues. Ann Biomed Eng, 34(1):161–8, 2006.
- [70] P. G. di Summa, P. J. Kingham, W. Raffoul, M. Wiberg, G. Terenghi, and D. F. Kalbermatten. Adipose-derived stem cells enhance peripheral nerve regeneration. J. Plast Reconstr Aesthet Surg, 63(9):1544–52, 2010.
- [71] D. E. Discher, P. Janmey, and Y. L. Wang. Tissue cells feel and respond to the stiffness of their substrate. *Science*, 310(5751):1139–43, 2005.
- [72] Démosthène Mitrossilis, Jonathan Fouchard, Axel Guiroy, Nicolas Desprat, Nicolas Rodriguez, Ben Fabry, and Atef Asnacios. Single-cell response to stiffness exhibits muscle-like behavior. Proc Natl Acad Sci U S A, 106(43):18243–18248, 2009.
- [73] P. Kollmannsberger, C. M. Bidan, J. W. C. Dunlop, and P. Fratzl. The physics of tissue patterning and extracellular matrix organisation: how cells join forces. *Soft Matter*, 7(20):9549–9560, 2011.

- [74] S. Y. Tee, J. Fu, C. S. Chen, and P. A. Janmey. Cell shape and substrate rigidity both regulate cell stiffness. *Biophys J*, 100(5):L25–7, 2011.
- [75] Viola Vogel and Michael Sheetz. Local force and geometry sensing regulate cell functions. *Nat Rev Mol Cell Biol*, 7(4):265–275, 2006.
- [76] I. Levental, P. C. Georges, and P. A. Janmey. Soft biological materials and their impact on cell function. Soft Matter, 3(3):299–306, 2007.
- [77] Pouria Moshayedi, Gilbert Ng, Jessica C. F. Kwok, Giles S. H. Yeo, Clare E. Bryant, James W. Fawcett, Kristian Franze, and Jochen Guck. The relationship between glial cell mechanosensitivity and foreign body reactions in the central nervous system. *Biomaterials*, (0), 2014.
- [78] Adam J. Engler, Shamik Sen, H. Lee Sweeney, and Dennis E. Discher. Matrix elasticity directs stem cell lineage specification. *Cell*, 126(4):677–689, 2006.
- [79] C. M. Cheng, P. R. Leduc, and Y. W. Lin. Localized bimodal response of neurite extensions and structural proteins in dorsal-root ganglion neurons with controlled polydimethylsiloxane substrate stiffness. *J Biomech*, 44(5):856–62, 2011.
- [80] N. D. Leipzig and M. S. Shoichet. The effect of substrate stiffness on adult neural stem cell behavior. *Biomaterials*, 30(36):6867–78, 2009.
- [81] Cathryn A. Sundback, Jeffery Y. Shyu, Yadong Wang, William C. Faquin, Robert S. Langer, Joseph P. Vacanti, and Tessa A. Hadlock. Biocompatibility analysis of poly(glycerol sebacate) as a nerve guide material. *Biomaterials*, 26(27):5454–5464, 2005.
- [82] P. C. Georges and P. A. Janmey. Cell type-specific response to growth on soft materials. *J Appl Physiol*, 98(4):1547–53, 2005.
- [83] Diane Hoffman-Kim, Jennifer A. Mitchel, and Ravi V. Bellamkonda. Topography, cell response, and nerve regeneration. Annual Review of Biomedical Engineering, 12 (1):203–231, 2010.
- [84] J. M. Anderson, A. Rodriguez, and D. T. Chang. Foreign body reaction to biomaterials. *Seminars in Immunology*, 20(2):86–100, 2008.
- [85] Douglas W Hamilton, Carol Oakley, Nicolas AF Jaeger, and Donald M Brunette. Directional change produced by perpendicularly-oriented microgrooves is microtubule-dependent for fibroblasts and epithelium. *Cell motility and the cytoskeleton*, 66(5): 260–271, 2009.

- [86] E. Stepien, J. Stanisz, and W. Korohoda. Contact guidance of chick embryo neurons on single scratches in glass and on underlying aligned human skin fibroblasts. *Cell Biol Int*, 23(2):105–16, 1999.
- [87] P. Clark, P. Connolly, A. S. Curtis, J. A. Dow, and C. D. Wilkinson. Topographical control of cell behaviour: Ii. multiple grooved substrata. *Development*, 108(4):635–44, 1990.
- [88] J. R. Fallon. Neurite guidance by non-neuronal cells in culture: preferential outgrowth of peripheral neurites on glial as compared to nonglial cell surfaces. *J Neurosci*, 5 (12):3169-77, 1985.
- [89] Catherina G Becker and Thomas Becker. Growth and pathfinding of regenerating axons in the optic projection of adult fish. *Journal of neuroscience research*, 85(12): 2793–2799, 2007.
- [90] Kristian Franze and Jochen Guck. The biophysics of neuronal growth. *Reports on Progress in Physics*, 73(9):094601, 2010.
- [91] A. Hurtado, J. M. Cregg, H. B. Wang, D. F. Wendell, M. Oudega, R. J. Gilbert, and J. W. McDonald. Robust cns regeneration after complete spinal cord transection using aligned poly-l-lactic acid microfibers. *Biomaterials*, 2011.
- [92] Jennifer A. Mitchel and Diane Hoffman-Kim. Cellular scale anisotropic topography guides schwann cell motility. *PLoS One*, 6(9):e24316, 2011.
- [93] J. M. Bruder, A. P. Lee, and D. Hoffman-Kim. Biomimetic materials replicating schwann cell topography enhance neuronal adhesion and neurite alignment in vitro. J Biomater Sci Polym Ed, 18(8):967–82, 2007.
- [94] N. M. Dowell-Mesfin, M. A. Abdul-Karim, A. M. Turner, S. Schanz, H. G. Craighead, B. Roysam, J. N. Turner, and W. Shain. Topographically modified surfaces affect orientation and growth of hippocampal neurons. *J Neural Eng*, 1(2):78–90, 2004.
- [95] A. M. Turner, N. Dowell, S. W. Turner, L. Kam, M. Isaacson, J. N. Turner, H. G. Craighead, and W. Shain. Attachment of astroglial cells to microfabricated pillar arrays of different geometries. J Biomed Mater Res, 51(3):430–41, 2000.
- [96] M. T. Yang, J. Fu, Y. K. Wang, R. A. Desai, and C. S. Chen. Assaying stem cell mechanobiology on microfabricated elastomeric substrates with geometrically modulated rigidity. *Nat Protoc*, 6(2):187–213, 2011.

- [97] D. W. Baker, X. Liu, H. Weng, C. Luo, and L. Tang. Fibroblast/fibrocyte: Surface interaction dictates tissue reactions to micropillar implants. *Biomacromolecules*, 2011.
- [98] Xiang Ge, Yang Leng, Xiong Lu, Fuzeng Ren, Kefeng Wang, Yonghui Ding, and Meng Yang. Bacterial responses to periodic micropillar array. *Journal of Biomedical Materials Research Part A*, pages n/a-n/a, 2014.
- [99] T. Yeung, P. C. Georges, L. A. Flanagan, B. Marg, M. Ortiz, M. Funaki, N. Zahir, W. Ming, V. Weaver, and P. A. Janmey. Effects of substrate stiffness on cell morphology, cytoskeletal structure, and adhesion. *Cell Motil Cytoskeleton*, 60(1): 24–34, 2005.
- [100] Patricia A Zuk, Min Zhu, Hiroshi Mizuno, Jerry Huang, J William Futrell, Adam J Katz, Prosper Benhaim, H Peter Lorenz, and Marc H Hedrick. Multilineage cells from human adipose tissue: implications for cell-based therapies. *Tissue engineering*, 7(2):211–228, 2001.
- [101] Paul J Kingham, Daniel F Kalbermatten, Daljeet Mahay, Stephanie J Armstrong, Mikael Wiberg, and Giorgio Terenghi. Adipose-derived stem cells differentiate into a schwann cell phenotype and promote neurite outgrowth in vitro. Experimental neurology, 207(2):267–274, 2007.
- [102] P. G. di Summa, D. F. Kalbermatten, W. Raffoul, G. Terenghi, and P. J. Kingham. Extracellular matrix molecules enhance the neurotrophic effect of schwann cell-like differentiated adipose-derived stem cells and increase cell survival under stress conditions. *Tissue Eng Part A*, 19(3-4):368-79, 2013.
- [103] Yu Suk Choi, Ludovic G. Vincent, Andrew R. Lee, Kyle C. Kretchmer, Somyot Chirasatitsin, Marek K. Dobke, and Adam J. Engler. The alignment and fusion assembly of adipose-derived stem cells on mechanically patterned matrices. *Biomaterials*, 33 (29):6943–6951, 2012.
- [104] K. Franze, P. A. Janmey, and J. Guck. Mechanics in neuronal development and repair. *Annu Rev Biomed Eng*, 15:227–51, 2013.
- [105] E. Spedden, J. D. White, E. N. Naumova, D. L. Kaplan, and C. Staii. Elasticity maps of living neurons measured by combined fluorescence and atomic force microscopy. *Biophys J*, 103(5):868–77, 2012.
- [106] L. Cai, L. Zhang, J. Dong, and S. Wang. Photocured biodegradable polymer substrates of varying stiffness and microgroove dimensions for promoting nerve cell guidance and differentiation. *Langmuir*, 2012.

- [107] Ivan R Minev, Pavel Musienko, Arthur Hirsch, Quentin Barraud, Nikolaus Wenger, Eduardo Martin Moraud, Jérôme Gandar, Marco Capogrosso, Tomislav Milekovic, Léonie Asboth, et al. Electronic dura mater for long-term multimodal neural interfaces. Science, 347(6218):159–163, 2015.
- [108] FrankXue Jiang, Bernard Yurke, BonnieL Firestein, and NoshirA Langrana. Neurite outgrowth on a dna crosslinked hydrogel with tunable stiffnesses. *Annals of Biomedical Engineering*, 36(9):1565–1579, 2008.
- [109] Jennie B Leach, Xin Q Brown, Jeffrey G Jacot, Paul A DiMilla, and Joyce Y Wong. Neurite outgrowth and branching of pc12 cells on very soft substrates sharply decreases below a threshold of substrate rigidity. *Journal of neural engineering*, 4(2): 26, 2007.
- [110] D. D. Dewitt, S. N. Kaszuba, D. M. Thompson, and J. P. Stegemann. Collagen imatrigel scaffolds for enhanced schwann cell survival and control of three-dimensional cell morphology. *Tissue Eng Part A*, 15(10):2785–93, 2009.
- [111] Sangyoon J Han, Kevin S Bielawski, Lucas H Ting, Marita L Rodriguez, and Nathan J Sniadecki. Decoupling substrate stiffness, spread area, and micropost density: a close spatial relationship between traction forces and focal adhesions. *Biophysical journal*, 103(4):640–648, 2012.
- [112] A. Engler, L. Bacakova, C. Newman, A. Hategan, M. Griffin, and D. Discher. Substrate compliance versus ligand density in cell on gel responses. *Biophys J*, 86(1 Pt 1):617–28, 2004.
- [113] Jie Shi Chua, Choon-Peng Chng, Aung Aung Kywe Moe, Jason Y. Tann, Eyleen L. K. Goh, Keng-Hwee Chiam, and Evelyn K. F. Yim. Extending neurites sense the depth of the underlying topography during neuronal differentiation and contact guidance. *Biomaterials*, 35(27):7750–7761, 2014.
- [114] J. S. Goldner, J. M. Bruder, G. Li, D. Gazzola, and D. Hoffman-Kim. Neurite bridging across micropatterned grooves. *Biomaterials*, 27(3):460–72, 2006.
- [115] K. J. Jang, M. S. Kim, D. Feltrin, N. L. Jeon, K. Y. Suh, and O. Pertz. Two distinct filopodia populations at the growth cone allow to sense nanotopographical extracellular matrix cues to guide neurite outgrowth. *PLoS One*, 5(12):e15966, 2010.
- [116] Robert D Stout, Chuancang Jiang, Bharati Matta, Illya Tietzel, Stephanie K Watkins, and Jill Suttles. Macrophages sequentially change their functional phenotype in

- response to changes in microenvironmental influences. The Journal of Immunology, 175(1):342–349, 2005.
- [117] Bryan N Brown, Buddy D Ratner, Stuart B Goodman, Salomon Amar, and Stephen F Badylak. Macrophage polarization: an opportunity for improved outcomes in biomaterials and regenerative medicine. *Biomaterials*, 33(15):3792–3802, 2012.
- [118] Carlo Perego, Stefano Fumagalli, and Maria-Grazia De Simoni. Temporal pattern of expression and colocalization of microglia/macrophage phenotype markers following brain ischemic injury in mice. *Journal of Neuroinflammation*, 8(1):174, 2011.
- [119] Nassir Mokarram, Alishah Merchant, Vivek Mukhatyar, Gaurangkumar Patel, and Ravi V. Bellamkonda. Effect of modulating macrophage phenotype on peripheral nerve repair. *Biomaterials*, 33(34):8793–8801, 2012.
- [120] Nassir Mokarram and RaviV Bellamkonda. A perspective on immunomodulation and tissue repair. *Annals of Biomedical Engineering*, pages 1–14, 2013.
- [121] A. K. Blakney, M. D. Swartzlander, and S. J. Bryant. The effects of substrate stiffness on the in vitro activation of macrophages and in vivo host response to poly(ethylene glycol)-based hydrogels. *J Biomed Mater Res A*, 100(6):1375–86, 2012.
- [122] K. A. Barth, J. D. Waterfield, and D. M. Brunette. The effect of surface roughness on raw 264.7 macrophage phenotype. *J Biomed Mater Res A*, 101(9):2679–88, 2013.
- [123] N. E. Paul, C. Skazik, M. Harwardt, M. Bartneck, B. Denecke, D. Klee, J. Salber, and G. Zwadlo-Klarwasser. Topographical control of human macrophages by a regularly microstructured polyvinylidene fluoride surface. *Biomaterials*, 29(30):4056–64, 2008.
- [124] Koyal Garg, Nicholas A. Pullen, Carole A. Oskeritzian, John J. Ryan, and Gary L. Bowlin. Macrophage functional polarization (m1/m2) in response to varying fiber and pore dimensions of electrospun scaffolds. *Biomaterials*, 34(18):4439–4451, 2013.
- [125] A. M. Labrousse, E. Meunier, J. Record, A. Labernadie, A. Beduer, C. Vieu, T. Ben Safta, and I. Maridonneau-Parini. Frustrated phagocytosis on micro-patterned immune complexes to characterize lysosome movements in live macrophages. Front Immunol, 2:51, 2011.
- [126] P. G. di Summa, D. F. Kalbermatten, E. Pralong, W. Raffoul, P. J. Kingham, and G. Terenghi. Long-term in vivo regeneration of peripheral nerves through bioengineered nerve grafts. *Neuroscience*, 181:278–91, 2011.

- [127] D Adam Young, Yu Suk Choi, Adam J Engler, and Karen L Christman. Stimulation of adipogenesis of adult adipose-derived stem cells using substrates that mimic the stiffness of adipose tissue. *Biomaterials*, 34(34):8581–8588, 2013.
- [128] Rafael D. Gonzalez-Cruz, Vera C. Fonseca, and Eric M. Darling. Cellular mechanical properties reflect the differentiation potential of adipose-derived mesenchymal stem cells. *Proceedings of the National Academy of Sciences*, 109(24):E1523–E1529, 2012.
- [129] Ravi V. Bellamkonda. Peripheral nerve regeneration: An opinion on channels, scaffolds and anisotropy. *Biomaterials*, 27(19):3515–3518, 2006.
- [130] Maria Siemionow and Grzegorz Brzezicki. Chapter 8 current techniques and concepts in peripheral nerve repair. volume 87 of *International Review of Neurobiology*, pages 141 172. Academic Press, 2009. doi: http://dx.doi.org/10.1016/S0074-7742(09) 87008-6. URL http://www.sciencedirect.com/science/article/pii/S0074774209870086.
- [131] S. K. Lee and S. W. Wolfe. Peripheral nerve injury and repair. J Am Acad Orthop Surg, 8(4):243–52, 2000.
- [132] X. Navarro, N. Lago, M. Vivo, K. Yoshida, K. P. Koch, W. Poppendieck, and S. Micera. Neurobiological evaluation of thin-film longitudinal intrafascicular electrodes as a peripheral nerve interface. 2007 Ieee 10th International Conference on Rehabilitation Robotics, Vols 1 and 2, pages 643–649, 2007.
- [133] Amit Pabari, Shi Yu Yang, Alexander M Seifalian, and Ash Mosahebi. Modern surgical management of peripheral nerve gap. *Journal of Plastic, Reconstructive & Aesthetic Surgery*, 63(12):1941–1948, 2010.
- [134] Satoshi Ichihara, Yuji Inada, and Tatsuo Nakamura. Artificial nerve tubes and their application for repair of peripheral nerve injury: an update of current concepts. *Injury*, 39:29–39, 2008.
- [135] W. W. Campbell. Evaluation and management of peripheral nerve injury. *Clin Neurophysiol*, 119(9):1951–65, 2008.
- [136] JW Fawcett and Roger J Keynes. Peripheral nerve regeneration. *Annual review of neuroscience*, 13(1):43–60, 1990.
- [137] C. Marin and E. Fernandez. Biocompatibility of intracortical microelectrodes: current status and future prospects. *Front Neuroeng*, 3:8, 2010.
- [138] J. M. Anderson. Biological responses to materials. Annual Review of Materials Research, 31:81–110, 2001.

- [139] David W Grainger. All charged up about implanted biomaterials. *Nature biotechnology*, 31(6):507–509, 2013.
- [140] K. C. Cheung. Implantable microscale neural interfaces. Biomedical Microdevices, 9 (6):923–938, 2007.
- [141] W. M. Grill and J. T. Mortimer. Electrical properties of implant encapsulation tissue. Ann Biomed Eng, 22(1):23–33, 1994.
- [142] W. M. Grill and J. T. Mortimer. Neural and connective tissue response to long-term implantation of multiple contact nerve cuff electrodes. *J Biomed Mater Res*, 50(2): 215–26, 2000.
- [143] D. K. Leventhal, M. Cohen, and D. M. Durand. Chronic histological effects of the flat interface nerve electrode. J Neural Eng, 3(2):102–13, 2006.
- [144] N. Lago, K. Yoshida, K. P. Koch, and X. Navarro. Assessment of biocompatibility of chronically implanted polyimide and platinum intrafascicular electrodes. *Ieee Transactions on Biomedical Engineering*, 54(2):281–290, 2007.
- [145] James W Fawcett and Richard A Asher. The glial scar and central nervous system repair. *Brain research bulletin*, 49(6):377–391, 1999.
- [146] KM Miller and JM Anderson. In vitro stimulation of fibroblast activity by factors generated from human monocytes activated by biomedical polymers. *Journal of biomedical materials research*, 23(8):911–930, 1989.
- [147] Natalia Lago, Dolores Ceballos, Francisco J. Rodriguez, Thomas Stieglitz, and Xavier Navarro. Long term assessment of axonal regeneration through polyimide regenerative electrodes to interface the peripheral nerve. *Biomaterials*, 26(14):2021–2031, May 2005. doi: 10.1016/j.biomaterials.2004.06.025. URL http://dx.doi.org/10.1016/j.biomaterials.2004.06.025.
- [148] David F Williams. On the mechanisms of biocompatibility. *Biomaterials*, 29(20): 2941–2953, 2008.
- [149] E Romero, Jean-François Denef, Jean Delbeke, Annie Robert, and Claude Veraart. Neural morphological effects of long-term implantation of the self-sizing spiral cuff nerve electrode. Medical and Biological Engineering and Computing, 39(1):90–100, 2001.
- [150] Pouria Fattahi, Guang Yang, Gloria Kim, and Mohammad Reza Abidian. A review of organic and inorganic biomaterials for neural interfaces. *Advanced Materials*, pages n/a-n/a, 2014.

- [151] JP Bearinger, S Terrettaz, R Michel, N Tirelli, H Vogel, M Textor, and JA Hubbell. Chemisorbed poly (propylene sulphide)-based copolymers resist biomolecular interactions. *Nature Materials*, 2(4):259–264, 2003.
- [152] Yinghui Zhong and Ravi V Bellamkonda. Controlled release of anti-inflammatory agent  $\alpha$ -msh from neural implants. *Journal of controlled release*, 106(3):309–318, 2005.
- [153] Yinghui Zhong and Ravi V Bellamkonda. Dexamethasone-coated neural probes elicit attenuated inflammatory response and neuronal loss compared to uncoated neural probes. *Brain research*, 1148:15–27, 2007.
- [154] Daniel J. Chew, Lan Zhu, Evangelos Delivopoulos, Ivan R. Minev, Katherine M. Musick, Charles A. Mosse, Michael Craggs, Nicholas Donaldson, Stéphanie P. Lacour, Stephen B. McMahon, and James W. Fawcett. A microchannel neuroprosthesis for bladder control after spinal cord injury in rat. Science Translational Medicine, 5 (210):210ra155-210ra155, 2013. ISSN 1946-6234. doi: 10.1126/scitranslmed.3007186.
- [155] Vivek Mukhatyar, Balakrishna Pai, Isaac Clements, Akhil Srinivasan, Richard Huber, Akash Mehta, Shoumit Mukhopadaya, Soumon Rudra, Gaurangkumar Patel, Lohitash Karumbaiah, and Ravi Bellamkonda. Molecular sequelae of topographically guided peripheral nerve repair. Annals of Biomedical Engineering, pages 1–20, 2013.
- [156] I. P. Clements, V. J. Mukhatyar, A. Srinivasan, J. T. Bentley, D. S. Andreasen, and R. V. Bellamkonda. Regenerative scaffold electrodes for peripheral nerve interfacing. *Neural Systems and Rehabilitation Engineering, IEEE Transactions on*, 21(4):554–566, 2013.
- [157] V. J. Mukhatyar, M. Salmeron-Sanchez, S. Rudra, S. Mukhopadaya, T. H. Barker, A. J. Garcia, and R. V. Bellamkonda. Role of fibronectin in topographical guidance of neurite extension on electrospun fibers. *Biomaterials*, 32(16):3958–68, 2011.
- [158] Ivan R Minev, Pouria Moshayedi, James W Fawcett, and Stéphanie P Lacour. Interaction of glia with a compliant, microstructured silicone surface. *Acta biomaterialia*, 9(6):6936–6942, 2013.
- [159] E. Mussig, T. Steinberg, S. Schulz, J. P. Spatz, J. Ulmer, N. Grabe, A. Kohl, G. Komposch, and P. Tomakidi. Connective-tissue fibroblasts established on micropillar interfaces are pivotal for epithelial-tissue morphogenesis. Advanced Functional Materials, 18(19):2919–2929, 2008.

- [160] Jami Scheib and Ahmet Hoke. Advances in peripheral nerve regeneration. Nat Rev Neurol, 9(12):668–676, 2013.
- [161] S. Chen, J. A. Jones, Y. Xu, H. Y. Low, J. M. Anderson, and K. W. Leong. Characterization of topographical effects on macrophage behavior in a foreign body response model. *Biomaterials*, 31(13):3479–91, 2010.
- [162] L. E. Dickinson, D. R. Rand, J. Tsao, W. Eberle, and S. Gerecht. Endothelial cell responses to micropillar substrates of varying dimensions and stiffness. J Biomed Mater Res A, 100(6):1457–66, 2012.
- [163] A. G. Rodriguez, S. J. Han, M. Regnier, and N. J. Sniadecki. Substrate stiffness increases twitch power of neonatal cardiomyocytes in correlation with changes in myofibril structure and intracellular calcium. *Biophys J*, 101(10):2455–64, 2011.
- [164] T. Steinberg, S. Schulz, J. P. Spatz, N. Grabe, E. Mussig, A. Kohl, G. Komposch, and P. Tomakidi. Early keratinocyte differentiation on micropillar interfaces. *Nano Lett*, 7(2):287–94, 2007.
- [165] Elisa Migliorini, Jelena Ban, Gianluca Grenci, Laura Andolfi, Alessandro Pozzato, Massimo Tormen, Vincent Torre, and Marco Lazzarino. Nanomechanics controls neuronal precursors adhesion and differentiation. *Biotechnology and Bioengineering*, 110(8):2301–2310, 2013.
- [166] P. Shi, K. Shen, S. Ghassemi, J. Hone, and L. C. Kam. Dynamic force generation by neural stem cells. *Cell Mol Bioeng*, 2(4):464–474, 2009.
- [167] Kate Poole, Regina Herget, Liudmila Lapatsina, Ha-Duong Ngo, and Gary R. Lewin. Tuning piezo ion channels to detect molecular-scale movements relevant for fine touch. Nat Commun, 5, 2014.
- [168] Ali K Refai, Marcus Textor, Donald M Brunette, and J Douglas Waterfield. Effect of titanium surface topography on macrophage activation and secretion of proinflammatory cytokines and chemokines. *Journal of Biomedical Materials Research Part A*, 70(2):194–205, 2004.
- [169] Enrica Saino, Maria Letizia Focarete, Chiara Gualandi, Enzo Emanuele, Antonia I Cornaglia, Marcello Imbriani, and Livia Visai. Effect of electrospun fiber diameter and alignment on macrophage activation and secretion of proinflammatory cytokines and chemokines. *Biomacromolecules*, 12(5):1900–1911, 2011.

- [170] Munish Batra, Steve Bernard, and George Picha. Histologic comparison of breast implant shells with smooth, foam, and pillar microstructuring in a rat model from 1 day to 6 months. *Plastic and reconstructive surgery*, 95(2):354–363, 1995.
- [171] S. R. Taylor and D. F. Gibbons. Effect of surface texture on the soft tissue response to polymer implants. *Journal of Biomedical Materials Research*, 17(2):205–227, 1983. ISSN 1097-4636. doi: 10.1002/jbm.820170202. URL http://dx.doi.org/10.1002/jbm. 820170202.
- [172] EunJung Kim, Aaron Fleischman, George Muschler, and Shuvo Roy. Response of bone marrow derived connective tissue progenitor cell morphology and proliferation on geometrically modulated microtextured substrates. *Biomedical Microdevices*, pages 1–12, 2013.
- [173] D. W. Baker and L. P. Tang. Effect of microtopography on fibrocyte responses and fibrotic tissue reactions at the interface. *Proteins at Interfaces Iii: State of the Art*, 1120:339–353, 2012.

## GLOSSARY

BSABovine Serum Albumin CNSCentral Nervous System CSICoherence Scanning Interferometry CDCritical Dimension DIDeionized DIVDays In Vitro DRGDorsal Root Ganglion DMEMDulbecco's Modified Eagle's Medium  $E_{eff}$ Effective elastic modulus ECMExtracellular Matrix FAFocal Adhesion FBGCForeign-body giant cells FBRForeign Body Reaction FBSFetal Bovine Serum Finite Element Method FEMFOVField of View IPAIsopropanol kSpring constant of pillar LNLaminin NGFNerve Growth Factor O/NOvernight PDLPoly-D-Lysine PDMSPoly(dimethyl siloxane PDLPoly-D-Lysine PFAParaformaldehyde REMReplica Molding RTRoom Temperature SCSchwann Cell SEMScanning Electron Microscopy / Standard Error of Mean w/vweight to volume ratio

adipose-derived stem cells

ASC

# Cédric Paulou

## Biomedical engineer

#### Education

2011–2015 PhD in Bioengineering, Center for Neuroprosthetics, EPFL.

Title: Interactions of Peripheral Nerve Cells with Soft Micropillar Interfaces

Thesis director: Prof. S. Lacour

2006–2008 MSc Bioengineering and Biotechnologies, School of Life Sciences, EPFL.

1-year exchange at Georgia Tech, USA Mention of excellence for the Master thesis

2006–2008 BSc Life Sciences and Technologies, School of Life Sciences, EPFL.

Orientation in Neurosciences

07-09 2006 EPFL-ISREC International Summer Research Program, Laboratory for

Lymphatic and Cancer Bioengineering.

Project title: Implications of VEGF on tumor metastasis

### Project Experience

2011–2015 PhD Student, Laboratory for Soft Bioelectronic Interface, EPFL.

Novel strategies for enhancing the bio-integration of regenerative neural interfaces

#### Expertise:

- Surface engineering: Creation of a 3D micro-patterns in silicone
- In vitro testing of cellular behaviour on
- Design and evaluation of implants for improving nerve regeneration
- Potential implications for increasing lifetime of implanted devices

#### Skills:

- Communication: written (thesis and article) and oral (presentations, posters)
- Laboratory organization (instruments, protocols, stocks)
- Teaching (semester students, lectures, practical courses)

#### 2009–2011 Research Assistant, Medical Photonics Group, EPFL.

Design and evaluation of an imaging technique for in-situ bladder cancer classification during endoscopic interventions

Development of a spectroscopic technique for measuring tissue oxygenation Skills:

- Clinical research in operating room setting at a university hospital (CHUV)
- Participation to the writing of a peer-reviewed article
- Collaboration with an industrial partner in endoscopy

2007–2008 **Master Student**, *Matrix Biology and Engineering Lab*, Georgia Institute of Technology, USA.

Construction of a Recombinant Plasminogen Activator with a Novel Fibrin Targeting Motif

#### Expertise:

- o Genetic engineering for designing a chimeric protein with novel functionalities
- Creation of a bacterial production system for the recombinant protein
- Optimization of protein folding conditions for recovery of active agent
- In-vitro evaluation of the chimeric agent properties

#### Achievements:

- One-year internship in a highly-ranked US technology institute
- Rapid integration in an international environment
- Acquired autonomy in experimental biomedical research

#### Skills

Biology Cell culture, in vitro experimentation, animal experimentation, molecular biology, immunohistology, protein engineering, mechanobiology, nerve regeneration

Microfab Soft lithography, photolithography, etching, silicone processing, cleanroom

Imaging Fluorescence, confocal, electronic Microscopy, image processing and analysis

IT Latex, MS Office, Origin, ImageJ, Illustrator, Photoshop, L-Edit

#### Languages

French Mother tongue

English Fluent

main working language, 1 year in the USA

German Basic

#### Publications and Conferences

Articles Primary neurons and glial cells respond to topographical and mechanical cues from micropillar-textured silicone substrates. <u>Paulou C</u>, Lacour SP. *Submitted* 

Real-time, in vivo measurement of tissular pO2 through the delayed fluorescence of endogenous protoporphyrin IX during photodynamic therapy. Piffaretti F, Novello AM, Kumar RS, Forte E, <u>Paulou C</u>, and Nowak-Sliwinska P, Van Den Bergh H, and Wagnières G. *Journal of biomedical optics* 2012

Proceeding Engineering fibrin ECM using fibrin knob-pocket interactions. Soon A, Stabenfeldt SE, <u>Paulou C</u>, Barker TH. *Matrix Biology Biennial Meeting* 2008

Conferences Micro-structured surfaces as substrate with tunable mechanical cues for understanding substrate-rigidity response in peripheral nerve neurons. <u>Paulou C</u>, Lacour SP. MRS Spring Meeting 2013

Micro-patterned silicone surfaces as instructive substrate for neuronal regeneration. Paulou C, Lacour SP. SSBE Annual Meeting 2012

Stretchable metallization for soft biolectronic interfaces. Musick K, <u>Paulou C</u>, Oppenheim T, Lacour SP. *Nanobiotech Montreux* 2011